SPIN TRANSPORT STUDY IN SPINTRONICS NANODEVICES

BALA KUMAR A/L SUNDARAM PILLAY

(B. Eng (Hons.), National University of Singapore)

REPORT SUBMITTED

FOR THE DEGREE OF DOCTORATE ENGINEERING

DEPARTMENT OF ELECTRICAL AND COMPUTER ENGINEERING

NATIONAL UNIVERSITY OF SINGAPORE

2008

Acknowledgements

I would like to thank my supervisor Dr. Mansoor Abdul Jalil for providing guidance and suitable references that have started me into the area of spintronics. I would also like to thank my co-supervisor, Dr. Tan Seng Ghee and Dr. Teo Kie Leong for helping me in my research work. Dr. Tan Seng Ghee has been especially helpful in guiding me to solve many theoretical problems during my research work. I also would like to thank Dr. Liang Gengchiau for helping me with theoretical understanding particularly in the section of microscopic transport.

S. Bala kumar

List of Publications

1. [!]S. G. Tan, M. B. A. Jalil, S. Bala Kumar, **Spin tunneling in multilayer spintronic devices**, Physical Review B 77, 085424 (2008)

2. [!]S. Bala Kumar, S. G. Tan, M. B. A. Jalil, **Bias current effects on the magnetoresistance of a FM-SC-FM trilayer**, Appl. Phys. Lett. 90, 142106 (2007).

3. [!]S. Bala Kumar, M. B. A. Jalil, S. G. Tan, **Spin-Polarized Resonant Transport in Hybrid FM-2DEG Structure**, Phys. Rev. B 75, 155309 (2007).

4. S. Bala Kumar, S. G. Tan, M. B. A. Jalil, **The effect of capping layer on the spin accumulation and magnetoresistance of a CPP spin valv**e, Appl. Phys. Lett. 90, 163101 (2007).

5. [!]S. Bala Kumar, S. G. Tan, M. B. A. Jalil et al., **Nanopillar ferromagnetic nanostructure as highly efficient spin injector into semiconductor**, Appl. Phys. Lett. 91, 142110 (2007).

6. [!]S. Bala Kumar, S. G. Tan and M. B. A. Jalil et al., **Nanoelectronic Logic Device based on the Manipulation of Magnetic and Electric Barriers**, J. Appl. Phys. 103, 054310 (2008).

7. [!]S. Bala Kumar, S. G. Tan, M. B. A. Jalil et al., **Spin transfer torque in current-perpendicular-to-plane multilayer structure induced by spin relaxation in the capping layer**, J. Appl. Phys. 103, 07A712 (2008).

8. N. L. Chung, M. B. A. Jalil, S. G. Tan, and S. Bala Kumar, **Interfacial resistance and spin flip effects on the magnetoresistance of a current-perpendicular to plane spin valve**, J. Appl. Phys. 103, 07F308 (2008).

9. S. Bala Kumar, S. G. Tan, M. B. A. Jalil et al., **Spin Injection due to interfacial spin asymmetry in a ferromagnet-semiconductor hybrid structure**, J. Appl. Phys. 102, 084310 (2007).

10. S. G. Tan, M. B. A. Jalil, S. Bala Kumar et al., **Theoretical modeling of Half-metallic CPP Spin Valves** , J. Appl. Phys. 101, 09J502 (2007).

11. S. G. Tan, M. B. A. Jalil, and S. Bala Kumar, **Influence of Spin Relaxation on Magnetoresistance**, J. Appl. Phys. 101, 044303 (2007).

12. S. Bala Kumar, S. G. Tan, M. B. A. Jalil, **Effect of Interfacial Spin Flip and Momemtum Scatering on Magnetoresistanc**e, IEEE Trans. Magn. 43, 2863 (2007).

13. Z. Y. Leong, S. G. Tan, M. B. A. Jalil, S. Bala Kumar et al., **Magnetoresistance modulation due to interfacial conductance of current perpendicular-to-plane spin valves**, J. Magn. Magn. Mater. 310, e635 (2007).

14. [!]S. Bala Kumar, M. B. A. Jalil, S.G. Tan et al., **Magnetoresistance effects arising from interfacial resistance in a current-perpendicular-to-plane spin-valve trilayer**, Phys. Rev. B 74, 184426 (2006).

15. M. B. A. Jalil, S. G. Tan, S. Bala Kumar et al., **Spin drift diffusion studies of magnetoresistance effects in current-perpendicular-to-plane spin valves with half-metallic insertions**, Phys. Rev. B 73, 134417 (2006).

16. S. G. Tan, M. B. A. Jalil, S. Bala Kumar et al., **Layer thickness effect on the magnetoresistance of a current-perpendicular-to-plane spin valve**, J. Appl. Phys. 100, 063703 (2006).

17. [!]S. T. Bae, S. G. Tan, M. B. A. Jalil, S. Bala Kumar et al., **Magnetoresistive behavior of current-perpendicular-to-plane trilayer with half-metal insertions**, J. Appl. Phys. 99, 08T107 (2006).

18. S. G. Tan, M. B. A. Jalil, S. Bala Kumar et al., **Utilization of magneto-electric potential in ballistic nano devices**, J. Appl Phys. 99, 084305 (2006).

19. [*]S. Bala Kumar, M. B. A. Jalil, S. G. Tan et al., **The effect of spreading resistance on the magnetoresistance of current-perpendicular-to-plane spin valves with patterned spacer layers**, IEEE Trans. Magn. 42, 3788 (2006).

20. S. Bala Kumar, S. G. Tan, M. B. A. Jalil et al., **MR Enhancement in Current-Perpendicular-to-Plane Spin-valve by Insertion of a Ferromagnetic Layer within the Spacer Layer**, IEEE Trans. Magn. 42, 2459 (2006).

21. S. G. Tan, M. B. A. Jalil, S. Bala Kumar , **Electrical control of ballistic spin-dependent conductance through magneto-electric barriers in the 2D-electron gas of GaAs heterostructure**, IEEE Trans. Magn. 42, 2673 (2006).

Citation Report:

Total citation : 44

Non-self citation: 13

[!] *Highlighted in Virtual Journal of Nanoscience and Technology*

[*] *Appear as the cover page of the issue.*

Contents

Summary

A detail understanding of the physics of spin transport phenomena is essential to enhance the performance of present spintronic devices, as well as in designing new devices for future applications. This thesis consists of theoretical study and simulation on the physics of spin transport in spintronic nanodevices. The spin transport phenomenon is mainly studied based on the i) semi-classical spin-drift-diffusion (SDD) equation, and the ii) mesoscopic Green's function (GF) formalism. SDD is a phenomenological model which describes the electron transport in the presence of spin relaxation in the diffusive transport regime. GF is a quantum theoretic model of electron transport in complex and inhomogeneous systems in the mesoscopic size range.

The aim of our simulation is to harness the physics of spin transport to improve the performance of devices such as the spin valves (SV) and spin-transistors, as well as to propose new design for these devices. In this thesis, first the effects of various device parameters on spin transport is analyzed in detail. Focus is given to the understanding of the fundamental physics of spin transport as well as identifying any anomalous and novel

effects. Once transport physics and the various transport effects are well understood, then we utilize this understanding to enhance the performance of the devices. We also explore new methods and device designs in order to further improve the performance.

First [Chapter 2-4] we study the optimization of magnetoresistance (MR) in metallic SV structures by using SDD transport model. We analyze the effects of the material and structural properties on the device performance. We notice various novel effects that influence the MR of the SV device, i.e. i) the effect of spin-independent resistivity on spin-dependent-scattering, ii) an anomalous MR suppression effect due to coupling of resistivity with spin relaxation, iii) complex interplay between spin-dependent-scattering, spin relaxation and the anomalous MR suppression effect due to increase in the FM layer thickness, iv) competitive resistance effect due to interfacial resistance or additional layers, and v) spreading resistance effect due to layer patterning. These effects were studied in detail and carefully utilized to optimize the MR ratio of the SVs. Next [Chapter 5], we study the spin transport phenomena in a 2DEG semiconductor structure, where ballistic transport is assumed. In this structure we notice resonant tunneling effect which leads to an oscillatory transport behavior. The transport properties, such as the transmission probability, the spin injection (SI) efficiency and the MR ratio, all exhibit oscillatory behavior when the electron energy is varied. We utilize this effect to design a magnetoresistive spin-transistor, whose MR can be varied by gate voltage. Then [Chapter 7] we incorporate magnetic gates into this transistor and apply GF formulation to study the effect of resonant tunneling across magnetic-electric barrier. Finally[Chapter 8] we integrate the two spin transport models–i) SDD and ii) GF– to develop a multiscale spin transport theory, which is used to study the effect of interfacial barrier profile and barrier asymmetry for further enhancement of the SI in a ferromag-

net/semiconductor(2DEG) interface.

(490 words)

List of Tables

List of Figures

List of Symbols and Abbreviations

List of Abbreviations

2DEG	Two-degree electron gas
AP	Anti-parallel
CIP	Current-in-plane
CPP	Current-perpendicular-to-plane
DMS	Diluted magnetic semiconductor
DOS	Density of States
FE	Finite-element
FEP	Finite-element Poisson
FM	Ferromagnet
GF	Green's Function
GMR	Giant Magnetoresistance
HEMT	High-electron-mobilty-transistor
IR	Interfacial resistance
MFP	Mean free path
MRAM	Magnetoresistive Random Access Memory
MR	Magnetoresistance
MTJ	Magnetic tunneling junction
NM	Non-magnet
P	Parallel
SC	Semiconductor
SDD	Spin dependent drift-diffuion
SDL	Spin diffusion length
SDT	Spin-dependent tunneling
SI	Spin injection
SPRT	Spin-polarized resonant tunneling
SR	Spreading resistance
SV	Spin valve
TC	Two-channel model
TMR	Tunneling Magnetoresistance
WF	Wave Function

List of Symbols

λ	average spin-diffusion-length	I	current
α	intrinsic conductance polarization	μ	electrochemical potential
ρ	resistivity	$\Delta\mu$	spin accumulation
d	layer thickness	E	energy
β	current polarization	G	Green's Function or Conductance
j	current density	Σ	Self energy

Subscripts:

$\blacksquare_F$	FM material	$\blacksquare_R$	left-contact
$\blacksquare_N$	NM material	$\blacksquare_L$	right-contact
$\blacksquare_S$	SC material	$\blacksquare_{FM}$	Fermi-level of metal
$\blacksquare_\uparrow$	spin-up	$\blacksquare_{FS}$	Fermi-level of SC
$\blacksquare_\downarrow$	spin-down	$\blacksquare_I$	interfacial property

Superscripts:

$\blacksquare^R$	retarded function	$\blacksquare^A$	advance function

Chapter 1

Introduction

1.1 Background

1.1.1 Electron Spin

In 1897, Sir J.J. Thompson discovered the electron, an elementary sub-atomic particle that carries a finite amount of charge. The electron's charge degree of freedom gives rise to the conventional electrical current in metals and semiconductors. Electrical current is produced as a result of electrons interacting with each other and with electromagnetic fields via Coulomb and Lorentz forces. In 1920s, two successive experimental evidences suggested an additional property of the electron. These experiments are: 1) investigation on the fine structure – on closer examination, the spectral lines of the hydrogen spectrum appears to be closely-spaced doublets, and 2) the Stern-Gerlach experiment – a beam of silver atoms directed through an inhomogeneous magnetic field splits into two beams. These experiments suggest that electrons have an intrinsic angular momentum. This intrinsic property, being classically analogous to a spinning ball of charge, was termed as electron spin. These two experiments – 1) fine structure and 2) Stern-Gerlach – also proved that electron spin is quantized into two discrete levels, namely "spin-up" with

the z-component of the spin-angular momentum of $S_z = +\frac{1}{2}\hbar$ and "spin-down" with $S_z = -\frac{1}{2}\hbar$.

1.1.2 Spintronics

In conventional electronic devices, the spin property of electrons has not been utilized for any practical purposes. Spintronics or magnetoelectronics,[4–9] is an emerging technology which exploits the "spin" property of the electrons in addition to the "charge" property. As as result, spintronics enables us to combine the advantages of both the features of electronics and magnetism to make new generation of devices.

Historically, spintronics technology emerged from seminal experiments conducted on spin dependent electron transport in solid state devices in 1980's. Some of the milestones that led to the progress in this field are as follows: 1) 1970 : Ferromagnet/superconductor tunneling experiments pioneered by Meservey and Tedrow,[10] 2) 1975 : Experiments on magnetic tunnel junctions by Julliere,[11] 3) 1985 : Observation of spin-polarized electron injection from a ferromagnetic metal to a normal metal by Johnson and Silsbee,[12] 4) 1988 : Discovery of giant magnetoresistance independently by Albert Fert et al.[13] and Peter Grnberg et al.[14] (1988), 5) 1990 : Theoretical proposal of the use of semiconductors for spintronics in a spin field-effect-transistor by Datta and Das[15] in 1990.

The primary requirement of a spintronic device is to have a system to generate spin polarized current. Spin polarized current refers to the current in which electrons with one type of spin (majority spin) are significantly more than the other type of spin (minority spin), hence there is an imbalance between spin-up and spin-down electrons.

The system that produces spin polarized current is called spin injector/polarizer. The next requirement is to transport, maintain and manipulate the spin current across the device. And finally, we need another system which is sensitive to the spin current, such that we can detect and measure the spin.

The spin property of electron can be technologically utilized in many ways. Some of the examples are: 1) Electron energy is dependent on the orientation of its spin. Therefore spin can be utilized in a new kind of binary logic of ones (high energy) and zeroes (low energy). 2) Similar to the flow of charges, the flow of spins also carry information. Therefore spin can be used for data transfer with the advantage of easily being manipulated with externally applied fields. 3) The alignment of spins creates a net magnetic moment, and therefore spin can be used for non-volatile data storage.

Since spintronics enables us to combine both the features of electron charge and electron spin, the performance of existing electronic products could be further enhanced by utilizing the advantages of the spin property of electrons. Electron spins can be manipulated faster and at lower energy cost compared to charges. Spin also has longer coherence length compared to electron mean free path, i.e. once spin is *created*; it maintains its state for a longer time, especially in the semiconductors. Hence, by utilizing the spin properties, it opens the possibility of developing new devices with many potential advantages such as: 1) non-volatile data storage, 2) higher data processing speed, 3) lesser power consumption and 4) larger integration density, compared to the conventional electronic devices.

Thus, spintronics technology is expected to result in new multifunctional devices[15–21] such as spin-field-effect-transistor, spin-light-emitting-diode, spin-resonant-

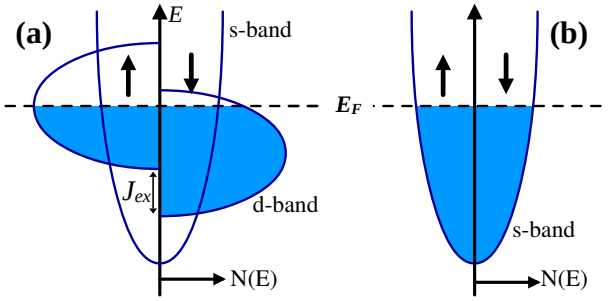

Figure 1.1: Density of States (DOS) that are available for electrons in a (a) ferromagnetic (FM) metal and (b) non-magnetic (NM) metal. In FM there is spin splitting of DOS. This is due to the magnetic exchange field in FM. E, the electron energy; E_F, the Fermi level; J_{ex}, the magnetic exchange energy; $N(E)$, the DOS.

tunneling-diode, optical switches operating at terahertz frequency, modulators, encoders, decoders, and quantum bits for quantum computation and communication. Spintronics also had successfully given rise to devices for memory/data storage application, e.g. spin valve and Magnetic Random Access Memory (MRAM).

1.2 Spin Transport Phenomena

Although the field of spintronics looks promising, many technical issues have to be resolved in order to have successful incorporation of spins into existing technology. These technical issues can be sub-divided into 4 main areas: 1) generating, 2) transporting, 3) manipulating, and 4) detecting spin polarized current in solid state devices.

1.2.1 Spin Generation

1.2.1.1 Spin in Ferromagnetic (FM) and Nonmagnetic (NM) Materials

In ferromagnetic (FM) materials[22,23] the simplest spin transport model is the two-channel model. In the two-channel model, electron transport is described as follows: a) spin-up

and spin-down electrons are transported in two different channels, b) both the channels are electrically parallel with each other, and c) both the channels are almost independent, i.e. there is rarely any interchange/flipping/mixing of electrons between the two channels (spin interaction does occur in a very long range. The details of such interaction is explained in Sec. 1.2.2.4). Therefore in FM, the electrical resistivity and mobility experienced by the spin-up and spin-down electrons are different. This unusual behavior of asymmetrical electron resistivity (and mobility) for spin-up and spin-down electrons in FM was first explained by Mott.[22,23]

The asymmetry in the electron mobility for different spins is also indirectly caused by the asymmetry in the electron density-of-state (DOS). In FM material, the DOS is asymmetrical for spin-up and spin-down electron due to the spin-splitting in the band structure [see Fig. 1.1]. The spin splitting in the band structure is caused by the magnetic exchange interaction field–the same field which causes ferromagnetism itself.

Due to these two reasons–1) two-channel transport(asymmetry in electron mobility) and 2) asymmetric in DOS–, in a FM material, the flux of spin-up and spin-down electrons are not equal; and thus the current in FM is spin polarized. When current passes from a FM metal to a nonmagnetic (NM) metal[12,24–26] via an ohmic contact, spin-polarized current is obtained in the NM due to the mobility asymmetry (*indirectly* due to DOS asymmetry) in FM. Similarly, when current passes from FM to NM via an insulator (tunneling contact), spin-polarized current is obtained in the NM *directly* due to the DOS asymmetry in FM. Therefore FM can be used as spin-polarizer in spintronics circuits.

1.2.1.2 Spin in Semiconductor (SC)

Although a significant amount of spin polarization arises in FM metals, this is inadequate for spin-based applications. Hence, non-equilibrium spin must be introduced in semiconductor (SC) to make advanced spin-based devices. SC based spintronics[4] can combine the well-known advantages of SC materials (i.e. versatility of charge transport manipulation and established nanofabrication technology) with the additional functionality provided by the spin degree of freedom. Recent experimental demonstrations of long spin diffusion length[27,28] in SC, and the ability to manipulate spin orientation by electrical and magnetic means[29–32] have brought the possibility of SC-based spintronics devices for memory, optoelectronic, and spin-field-effect transistor applications[15] closer to realization. The key parameters which need to be optimized in future SC-based spintronic devices is its spin injection (SI) efficiency, i.e. the ability to inject spin polarized current into semiconductor.[20,33,34] Initial SC-based devices which utilized direct spin injection from FM electrodes into the SC layer, had extremely low SI due to the large conductivity mismatch.[35–39] This mismatch problem has been overcome by the incorporation of tunnel barriers[36,40,41] and the use of diluted magnetic semiconductors (DMS) as spin-injectors,[41] although the latter suffer from generally low Curie temperature.[29,42] Spin can also be created in SC via optical method,[43,44] i.e, by shining circularly polarized light to transfer the angular momentum from photon to electron.

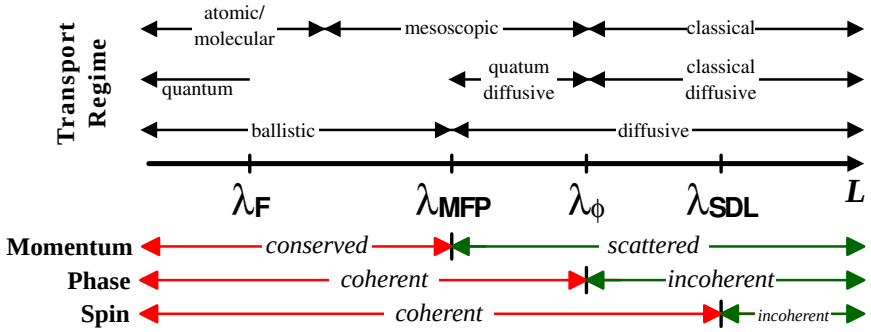

Figure 1.2: λ_F, λ_{MFP}, and λ_{SDL} refers to Fermi-wavelength, mean free path (MFP), and spin diffusion length (SDL), respectively. MFP is the average distance traveled by an electron before colliding with another particle and thus loosing initial momentum. Diffusive transport, occurs when λ_{MFP} is shorter than the device dimensions, L, i.e. $L >> \lambda_{MFP}$. Thus in diffusive transport, electron collides many times, before transported across the device. Diffusive transport is commonly described by the semi-classical Boltzmann model. SDL indicates how far an electron can travel in a diffusive conductor before its initial spin direction is randomized. For an electron to maintain its spin coherence, the device dimension should be lesser than λ_{SDL}. Generally in metals $\lambda_{MFP} < \lambda_{SDL}$, hence two independent diffusive spin channels can be utilized to describe the transport. This gives rise to the two-channel model. In SC SDL is much larger, implying the importance of injecting spin into SC. Diffusive transport is described by using spin-drift-diffusive model. Ballistic transport occurs when $L < \lambda_{MFP}$, where electrons move without colliding with each other. In ballistic transport, the transport conditions are predetermined by reservoirs at the boundaries. Ballistic transport is described by using Landauer formula. Quantum transport occurs when $L < \lambda_F$. In this regime electrons exhibit wave property.

1.2.2 Spin Transport

1.2.2.1 Transport Regime

Spin-polarized electron transport will occur naturally in any material in which there is a difference in the spin-populations at the Fermi level. In general, spin transport can be described by the appropriate type of theoretical transport methodology of the transport regime applicable in the device or in a given experimental system. Compared to charge transport, in spin transport, spin coherence is maintained for much larger time (and length) scale. Figure 1.2 shows various electron transport regimes and the physical phenomena related to these regimes.

1.2.2.2 Spin Injection (SI)

Spin injection (SI) is the process of transporting spin electrically into a material, usually SC. The strength of SI can be measured by determining the value of spin-polarization of current, at the contact from where the electrons are injected. There are various methods to inject spin into SC:

1. Ohmic SI[33,39]– spin polarized current in FM is transferred into the SC via ohmic FM/SC interface. The resistivity of the SC (ρ_N) and of the FM (ρ_F) influences the effectiveness of the SI. For substantial spin to be injected, the condition of $\rho_F \gg \rho_N$ must be met. But, in practical materials $\rho_F \ll \rho_N$ and hence ohmic SI into SC is very inefficient.[35]

2. Tunneling SI[41,45–47] – Unlike ohmic SI, in tunneling SI the resistivities of the electrodes play a minimal role. This is because when the impedance of the barrier is sufficiently high; the DOS of the two electrodes that are involved in the tunneling process determines the transport across the interface. As such, the current through the barrier is very small while the electrodes remain in equilibrium.

3. Ballistic SI[48,49] –Spin is injected across the FM-SC interfaces in the ballistic regime, whereby the spin-dependant transmission probability of the electron is determined by the difference between the two spin conduction subbands of the FM metal and the conduction band of the SC.

1.2.2.3 Spin Accumulation

When a current passes from FM metal to NM metal, it carries with it a net spin angular momentum and hence magnetization. The magnetization which builds up in the new

material is known as spin accumulation. The magnitude of spin accumulation is determined by the equilibrium between the net SI rate at the interface and spin relaxation rate at the bulk of NM.

1.2.2.4 Spin Relaxation

Due to spin relaxation, spin accumulation decays exponentially from the interface on a length scale called the spin-diffusion-length (SDL), λ_{SDL}. Thus SDL is a very important parameter in determining the maximum thickness of NM material. The time scale equivalent to SDL is the spin-relaxation-time – the time that determines how long electron maintains its spin state in a material. Relatively, electron-spin takes much large time (and length) to relax compared to electron-momentum, especially in SC. Some of the common mechanisms[50] which causes spin relaxation are: Elliot-Yafet mechanism,[51] D'yakonav-Perel' mechanism,[52] Bir-Aranov Pikus mechanism,[53] and Hyperfine-interaction.[54]

1.2.3 Spin Manipulation

Once spin is created or injected in a material, we need to control the spin to obtain desired outcome. The techniques to change and control the spin state of electrons in devices is referred as spin manipulation. Spin manipulation can be done via various means, such as: a) electrical field and spin-orbit interactions,[55–57] b) g-factor modulation,[58] c) magnetic semiconductor,[57,59] d) magnetic field[56,60,61] and e) optical[56,62] means.

1.2.4 Spin Detection

Finally, we need to sense and measure the changes in the signals caused by the presence of nonequilibrium spin in the spintronic devices. The system which is sensitive to this signal is called a spin-detector. One of the ways to detect spin in spin-transistors is by putting a FM filter in front of the device (at the drain of the transistor) such that the filter will act as a spin sensitive detector.[15] Magnetic Force Microscopy is used to image the spin state of surfaces with high resolution. In semiconductors, spin detection can be achieved by utilizing the effects of spin accumulation,[63] optical emmision,[64,65] Faraday rotation,[66] and band-filling.[67] In multilayered devices, magnetoresistive effect can be utilized to detect the spin (magnetization) state of the layers.

1.3 Magnetoresistive Devices

Since spin is proportional to magnetic moments of the electron, spintronics is also linked to magnetism. One of the unique characteristic of some of the spintronic devices is the effect of magnetoresistance (MR). MR refers to the change in the electrical resistance of a material, when the material is exposed to an external magnetic field. MR devices, which have the ability to detect magnetic field, are being used as reading heads in magnetic hard disks. In this section, we highlight the concept and some of the applications of magnetoresistive devices in data storage technology.

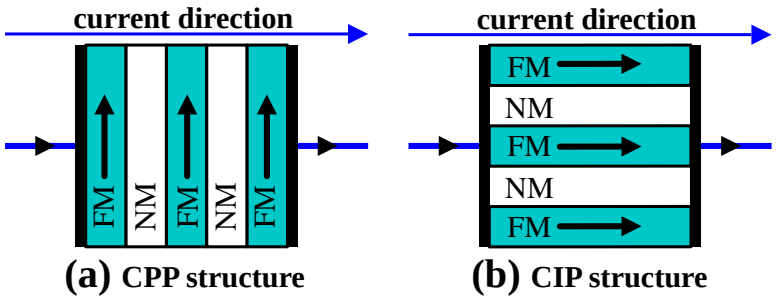

Figure 1.3: a) GMR multilayer in CPP configuration. b) GMR multilayer in CIP configuration. Direction of the arrows inside the layers indicates magnetization of the FM.

1.3.1 Giant Magnetoresistance (GMR)

Giant magnetoresistance (GMR)[68–70] refers to the huge change in electrical resistance that occurs when a strong magnetic field is applied to a multilayer made of alternating FM and NM metallic layers. GMR was unveiled by applying magnetic field to magnetic metallic multilayers such as Fe/Cr[13,14,71] and Co/Cu,[72] in which FM layers are separated by NM spacer layers of few nm thick. Significant reduction in the electrical resistance was observed in such multilayer. This effect was found to be much larger than other MR effects that was previously observed in metals and hence termed, “giant-MR”.

There are two configurations in which a MR multilayer device can operate: 1) current-perpendicular-to-plane (CPP)[73–78] and 2) current-in-plane (CIP)[78–80][refer Fig. 1.3]. CIP was the first to be discovered as its geometry is easier to be realized compared to CPP. CPP implementation requires sophisticated nanolithography technology.

When external magnetic field is applied to a GMR multilayer, the applied field aligns the magnetic moments of the FM layers, and thus the resistance of the multilayer varies accordingly. When magnetic moments of all the FM layers are aligned (parallel to each other), spin polarized electrons of one polarity is scattered less than the other polarity. On the other hand, when magnetic moments in FM layers are anti-aligned,

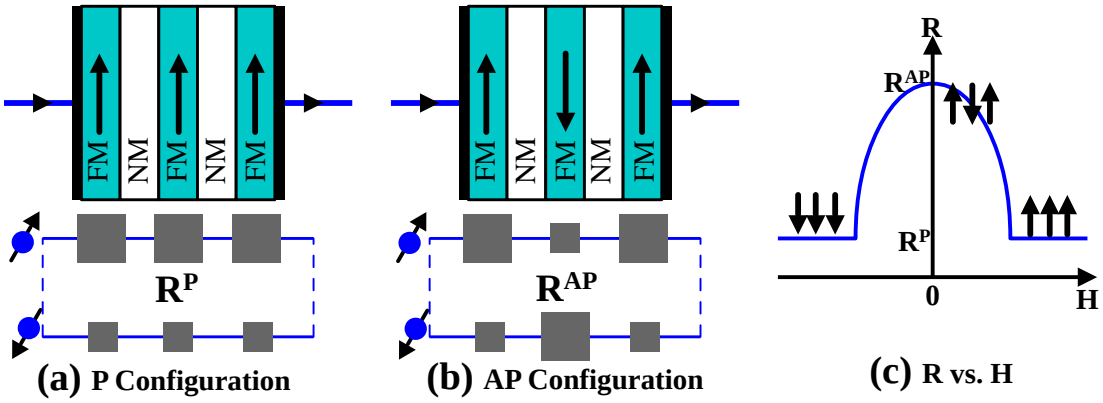

Figure 1.4: Resistor model to represent the GMR multilayers. a) GMR multilayer in parallel (P) configuration. b) GMR multilayer in antiparallel (AP) configuration. The two parallel paths correspond to the respective spin channels. The direction of the arrows inside the layers indicates magnetization direction. Big (small) box in the resistance circuit indicates large (small) resistance. c) Sketch of resistance, R and magnetic field, H. $R^{P(AP)}$ indicates the resistance of the structure at P (AP) configuration.

electrons of both polarities–spin-up and spin-down– are highly scattered. This causes a decrease in the electron mean free path (MFP) and hence decreases the resistance of the multilayer.

Figure 1.4 shows simple resistor models to illustrate the GMR effect in a multilayer. The resistor models make use of series resistors to represent resistances that electrons experience as they traversed through the layers. Generally, GMR multiyers are designed such that with the absence of the magnetic field, the magnetizations of the FM layers are anti-parallel [Fig. 1.4(b)]. And, by applying appropriate magnetic field, magnetization of the FM layers are aligned in parallel [Fig. 1.4(a)]. This gives rise to the changes in resistance as shown in Fig. 1.4c. The MR of the device is defined as $MR = \frac{R^{AP}-R^{P}}{R^{AP}}$, where $R^{AP}(R^{P})$ is antiparallel (parallel) resistance.

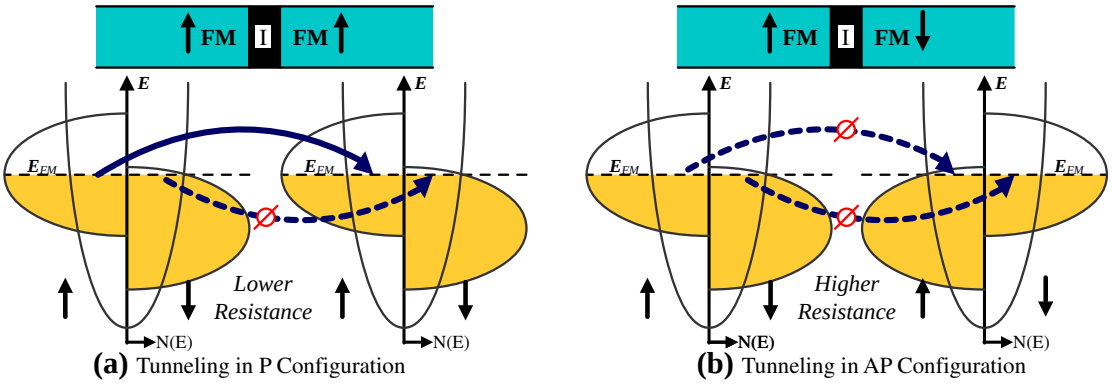

Figure 1.5: Tunneling in parallel and antiparallel configurations, in a FM/I/FM magnetic tunneling junction. Dashed (solid) curved arrows indicates high (low) resistive tunneling.

1.3.2 Magnetic Tunnel Junction (MTJ)

A magnetic tunnel junction (MTJ) consists of two layers of magnetic metals separated by an ultrathin layer of insulator (I) as shown in Fig. 1.5. The I layer is so thin that electrons tunnel through the layer if a bias voltage is applied across the two FM electrodes. The tunneling current depends on the relative orientation of the magnetizations of the two FM layers, which is varied by external magnetic fields. The variation in tunneling current gives rise to tunneling-MR(TMR) effect in these MTJ structures.

The TMR effect can be explained by using Julliere's model,[11] which is based on two assumptions: 1) spin of electrons is conserved in the tunneling process, and 2) tunneling of up-spin and down-spin electrons are two independent processes. Based on these assumptions, spin-dependent-tunneling (SDT) – electrons originating from spin-up(down) state of the first FM layer can only tunnel to the unfilled spin-up(down) states of the second FM layer – occurs at FM/I/FM interface.

SDT leads to the TMR effect because there is an imbalance in the electric current carried by spin-up and spin-down electrons tunneling at FM/I/FM interface. The origin

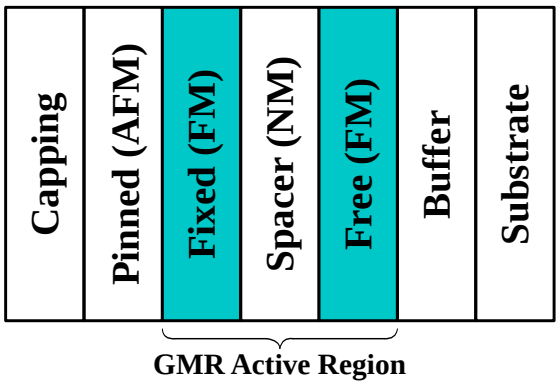

Figure 1.6: Structure of typical spin valve (SV) device. The active region of a SV device comprise of a GMR trilayer. The free layer is magnetically soft (the magnetization is relatively very sensitive to small fields) while the fixed/pinned layer is magnetically hard (the magnetization is relatively insensitive to fields of moderate size). The magnetization of the fixed layer is pinned or exchange-biased in a certain direction by a pinning layer. The pining layer is used as a reference layer. Depending on the external magnetic fields, the magnetization of the free layer becomes parallel or anti-parallel to the magnetization of fixed layer. In between the pinned layer and free layer, there is a thick Cu spacer layer to prevent any magnetic coupling between the layers. There are also Ta layers which act as a buffer (to provide a good growth surface) and a cap (to avoid oxidization of the sample in the air). The whole sample is deposited on a piece of Si substrate which is much thicker than the whole multilayer structure.

of this current imbalance is qualitatively explained by the fact that the electronic bands of the FM are exchange split, i.e. DOS at the Fermi energy for the spin-up and spin-down electrons are different. Therefore, the number of electrons that can tunnel through the barrier and consequently the tunneling resistance are dependent on spin state of the electrons.

Thus, if the two FM layers are magnetized parallel (antiparallel), the minority and majority spins tunnel to the minority (majority) and majority (minority) spin states, respectively. Hence the tunneling resistance is higher in anti-parallel configuration compared to parallel configuration. Referring to Fig. 1.5, TMR is defined as $TMR = \frac{R_{\uparrow\downarrow} - R_{\uparrow\uparrow}}{R_{\uparrow\downarrow}}$.

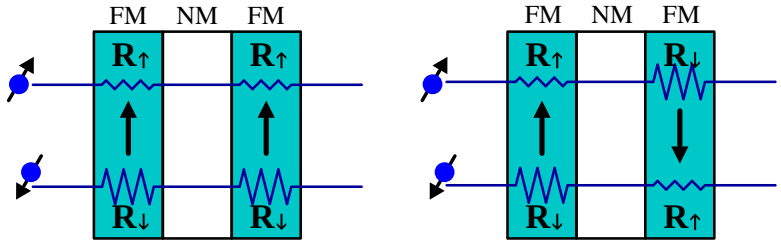

(a) P Configuration **(b) AP Configuration**

Figure 1.7: Channel paths corresponds to each spin polarized electrons as they traversed through the layers of a spin valve in a) parallel, and, b) antiparallel configuration. The direction of the arrows inside the layers indicate magnetization direction of the layers. The resistance that corresponds to the parallel configuration, $R^P = 2R_\uparrow \parallel 2R_\downarrow = 2R_\uparrow R_\downarrow/(R_\uparrow + R_\downarrow)$ and the resistance that corresponds to the antiparallel configuration, $R^{AP} = (R_\uparrow + R_\downarrow) \parallel (R_\uparrow + R_\downarrow) = (R_\uparrow + R_\downarrow)/2$.

1.3.3 Spin Valve (SV)

Spin valve (SV)[81,82] is a magnetic multilayer device that functions based on GMR effect. SV is being used as the reading head in the magnetic hard disk. Figure 1.6 shows the structure of a typical SV device and function of various layers in the device.

Referring to Fig. 1.7, in parallel configuration, the spin-up electron passes through the NM metal without much scattering whereas the spin-down electron is scattered. Therefore the spin-up electrons are in a low resistance state. In the anti-parallel configuration, both spins–up and down–experience scattering, giving rise to the high resistance state. By using the simple resistor model as illustrated in Fig. 1.7(a), the resistances that corresponds to the parallel configuration, R^P and antiparallel configuration, R^{AP} are obtained. Note that $R^P = 2R_\uparrow R_\downarrow/(R_\uparrow + R_\downarrow)$ is smaller than $R^{AP} = (R_\uparrow + R_\downarrow)/2$, i.e. $R^P < R^{AP}$. The difference between R^P and R^{AP} leads to the MR effect.

1.3.4 Magnetoresistive Random Access Memory(MRAM)

Magnetoresistive random access memory (MRAM)[83] is a non-volatile memory device, which stores data bits using magnetic moments instead of conventional electrical charges. MRAM is built from a grid of MTJ "cells". MRAM uses the magnetization configuration of the MTJ cells for information storage, e.g. "0" and "1" correspond to parallel and antiparallel configuration in the MTJ. Data is written by using magnetic hysteresis, i.e. by changing the magnetization configuration of the MTJ cells. Data is read by using MR effect, i.e. measuring the electrical resistance of the MTJ cell.

1.4 Motivations and Objectives

Spintronics is a newly emerging technology which is still in its infancy. As far as commercialization is concerned, spintronics has just been recently introduced into data storage and memory technologies. However, since its introduction, spintronics devices have brought significant improvements in these technologies. In addition to this, spintronics is also considered to be one of the highly promising technology for the future data storage and memory applications. However, among the obstacles for the future development of spintronics is the lack of the understanding of the spin transport physics in nanodevices. A detail understanding of the physics of spin transport phenomena is essential to enhance the performance of present spintronics devices, as well as in designing new devices for future applications.

This thesis aims to model and understand the spin transport in spintronic nanodevices, especially in spin valves and spin transistors. Spin transport phenomena will be mainly studied based on the i) semi-classical spin-drift-diffusion (SDD)[25,26,36] equation,

and the ii) mesoscopic Green's function (GF)[84–86] formalism. The focus of our analysis is to harness the physics of spin transport to improve the performance of spintronic devices (spin valves and spin transistors), as well as to propose new designs for these devices. The work described in the thesis aims to achieve the following three objectives:

1. To develop mathematical models for diffusive and mesoscopic transport in spintronic devices. These models will be used to describe and study the spin transport phenomena in the devices.

2. To investigate the effects of material and structural properties on spin transport. Focus will be given to the fundamental understanding of the physics as well as identifying any anomalous and novel effects.

3. To utilize the fundamental understanding of the physical phenomena to enhance/optimize the performance of spintronic devices, i.e. improving spin injection and magnetoresistance. We would also explore new methods and device designs to further improve the device performances.

Besides this, the simulation programs that we developed to model the spin transport, will be helpful in aiding the experimentalists to predict the device performance prior to conducting experiments.

1.5 Outline

The outline of this thesis is as follows:

Chapter 2: We develop a mathematical model to describe the spin transport in a trilayer-SV device using the phenomenological SDD equation. Using this model, we perform

analytical and numerical analysis to study the effect of material and structural properties on the MR of the SV device. We focus our analysis mainly on understanding the physics of spin transport in the CPP SV as well as optimizing the material parameters to achieve high MR ratio. We discover various novel/intersting effects which are further utilized to enhance the MR ratio.

Chapter 3: We further study the optimization of MR when there are additional resistive components in the trilayer-SV. In a more realistic device the electron scattering at the interfaces between different layers give rise to additional resistive components. We analyze the effect of such interfacial resistances (IR) on the MR of the device. We also propose an alternative method to enhance MR, i.e. by inserting additional layers in the SV. The effect of such layer insertion is explored in detail. In both of these cases, the additional resistive components–1) IR and 2) additional layers–give rise to an interesting effect, whereby each of the individual resistive components competes with each other in dominating the spin asymmetry of the device. Our results show that this competitive resistance effect plays a very crucial role in MR optimization. We also analyze the interplay between competitive resistance effect and spin-relaxation for further optimization of the MR.

Chapter 4: After studying this competitive resistance effect, we analyze the spin transport effects due to patterning the layers of SV devices. Patterning of the layers not only effects the resistance due to areal change, but also gives rise to the current confinement effect which further causes other phenomenon such as current crowding and spreading resistance. Therefore, to optimize MR all these effects have to be considered. We have also shown that by carefully utilizing these effects, and with the knowledge from previous chapters, the device performance can be further enhanced.

Chapter 5: In all the previous chapters, we studied the electron and spin transport properties in a purely diffusive regime. In this following chapter we study electron and spin transport across a ballistic 2DEG structure. We find that the transport properties of the device, such as the transmission probability, the SI efficiency and the MR ratio, all exhibit oscillatory behavior when the electron energy is varied. The basis of these oscillations is the resonant transport across the 2DEG. By utilizing this resonant transport property, we further propose a SC-based gate controlled MR device that could perform the function of a metallic SV, but with the advantage that its MR can be optimized (post-fabrication) and its stability enhanced by controlling a gate bias voltage.

Chapter 6: Next we explain the physics of electron transport from microscopic view, and further develop a theoretical model, based on tight-binding Green's Function (GF) method, to describe electron transport in mesoscopic regime.

Chapter 7: We apply this GF model to study the effect of spin transport and optimization of SI across a magnetic-electric barrier in a spin transistor device. We proposed a viable form of spin current transistor which passes electron through a series of magnetic-electric barriers built into the device. The barriers assume a wavy spatial profile across the conduction path due to the inevitable broadening of the magnetic fields. Field broadening results in a monotonically increasing magnetic vector potential across the conduction channel, which increases spin polarization. We have identified that the important factors for generating high spin polarization and conductance modulation.

Chapter 8: Finally, we integrate the two main spin transport models described in this thesis, i.e.1) the microscopic GF formalism, and 2) macroscale SDD model, and develop a multiscale spin tunneling theory to study spin transport across the interfaces of multilayer spintronics. This multiscale approach opens the possible for the detailed

theoretical studies of interfacial properties (e.g. barrier height, barrier shape and barrier spin asymmetry) required for achieving high spin injection via tunneling. Based on the calculated results, the optimal interfacial properties have been identified for possible experimental verification.

Chapter 9: We conclude this thesis and suggest future works in this area.

Chapter 2

Physics of the Trilayer CPP Structure

In this chapter, we perform analytical and numerical studies of the MR of a CPP SV structure using the phenomenological spin-drift-diffusion models. We develop a mathematical model to compute the spin accumulation, current polarization, potential variation and MR in the SV device. Using this model, we analyze the effect of material and structural properties on the MR of the device. We focus our analysis mainly on understanding the physics of spin transport in the CPP SV as well as optimizing the material parameters to achieve high MR ratio. We discover various novel/intersting effects, i.e. i) the effect of spin-independent resistivity on spin-asymmetry, ii) an anomalous MR suppression effect due to the coupling of spin relaxation with resistivity and iii) complex interplay between spin-asymmetry, spin relaxation and the anomalous MR suppression effect due to increase in the FM layer thickness. These effects are further utilized to enhance the MR ratio.

2.1 Introduction

Giant-magnetoresistance[68–70] (GMR) refers to a large fractional change in resistance induced by an applied external magnetic field, which changes the magnetization orientations of the two FM layers separated by a NM spacer, from the parallel to the anti-parallel configuration. GMR effects were first reported in the Fe/Cr,[13,14,71] Co/Cu,[87] as well as Ag/Co[72] multilayers, but later devices are based on the SV trilayer structure. For these SV structures, experiments have demonstrated that the CPP[?,73–77] geometry achieves a higher MR ratio compared to the CIP geometry. Due to its structural geometry, the CPP structure also possess the engineering advantages[88,89] of achieving smaller shield-

Material	$\rho(\Omega m)$	α	$\lambda(nm)$	**Material Type**
NiFe	1.16×10^{-7}	0.4	5	FM
CoFe	1.05×10^{-7}	0.4	15	FM
Cu	1.68×10^{-8}	0	140	NM
CrO_2	5.24×10^{-7}	0.7	10	HM
Fe_2O_3	1.99×10^{-4}	0.7	10	HM

Table 2.1: Materials and typical material parameters[1–3] at room temperature. ρ, α, λ, FM, NM, HM refers to resistivity, intrinsic conduction polarization, spin relaxation length, ferromagnet, nonmagnet, and half-metal.

to-shield gap, which is crucial in present ultra-high density magnetic recording beyond 1 $Tbit/in^2$. In parallel with the experimental efforts, many theoretical[25,26,35,36,90–92] models, have been developed to investigate the GMR effect in both the CPP and CIP configurations.

However, the continued increase in the areal density of magnetic recording information storage media on magnetic platters poses a heavy demand on increasing the MR of CPP structure. The present exchange-biased CPP sensors with the experimentally-realized MR of around 3-4% are inadequate to meet the requirements imposed by ultra-high density storage of several terabits per square inch.

In this chapter, we perform both analytical and numerical studies of the MR of a CPP structure using the phenomenological spin-drift-diffusion(SDD) models. For simplicity, our studies are deliberately focused only on the active MR region of a CPP SV. This active region consists of FM-NM-FM trilayer, as shown in Fig. 2.1. We call our device as a pseudo-SV (PSV) device. In a real SV device there are other required passive layers that contribute negatively to the overall MR e.g. the capping and the shield layers.

First, we develop a mathematical model to compute spin accumulation, current

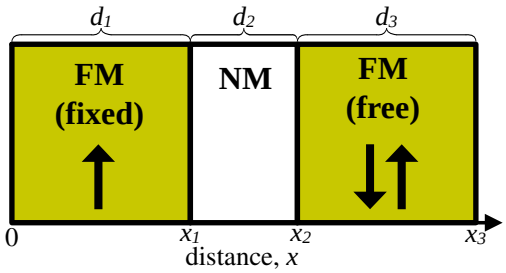

Figure 2.1: Schematic illustration of a trilayer CPP spin valve which forms the active region of a typical CPP spin valve sensor used in the recording heads.

polarization, potential variation and MR of the PSV [Sec. 2.2]. Using this model, we further analyze the effect of material and structural properties on the MR of the device [Sec. 2.3]. In our analysis we focus mainly on understanding the physics of spin transport as well as optimizing the material parameters to achieve high MR ratio. Via our analysis, we notice various novel effects, i.e. i) the effect of spin-independent resistivity on spin-asymmetry [Sec. 2.3.1], ii) an anomalous MR suppression effect due to the coupling of spin relaxation with resistivity [Sec. 2.3.3] and iii) complex interplay between spin-asymmetry, spin relaxation and the anomalous MR suppression effect due to increase in the FM layer thickness [Sec. 2.3.4]. These effects are further utilized to enhance the MR ratio.

Unless otherwise stated, the values of material parameter used in our numerical analysis is shown in Table 2.1.

2.2 Theory

2.2.1 Boltzmann Spin-Drift-Diffusive (SDD) model

In this section we develop the analytical model to study the spin transport and calculate the MR in a CPP multilayer device based on the collinear spin-drift-diffusive (SDD) equations. The SDD method used here is based on the earlier works of van Son,[25] Fert-Valet,[26] and Rashba.[36]

In our model, λ, α, ρ, d, β, j, and μ indicate average spin-diffusion-length (SDL) of minority and majority spin, intrinsic conductance polarization, resistivity, layer thickness, current polarization, current density, and electrochemical potential, respectively. Arrow superscript/subscripts $\uparrow(\downarrow)$ refer to the majority (minority) spin component, and numerical subscripts i refer to the layer index. The subscript F and N refers to FM and NM layer, respectively.

In this model, j is kept constant while the electrochemical potential is allowed to vary across the device. Due to spin-split property of the FM layers, j and ρ split into their spin-dependent components given by:

$$j_\uparrow = \beta j \quad ; \quad j_\downarrow = (1-\beta)j, \tag{2.1a}$$

$$\rho_\uparrow = 2\rho/(1+\alpha) \quad ; \quad \rho_\downarrow = 2\rho/(1-\alpha), \tag{2.1b}$$

where $\rho_\uparrow||\rho_\downarrow = \rho$, $j_\uparrow + j_\downarrow = j$, $\beta = j_\uparrow/j$, and $\alpha = (\rho_\uparrow - \rho_\downarrow)/(\rho_+\rho_\downarrow)$. The current density, $j = I/A$ where I is the total current and A is the cross sectional area of the device.

Based on Ohm's Law, current density is related to the electrochemical potential

gradient as follows:

$$\frac{\partial \mu_{\uparrow,\downarrow}}{\partial x} = -e\rho_{\uparrow,\downarrow} j_{\uparrow,\downarrow} \tag{2.2}$$

where, e is the electron charge and x is the spatial position.

The spin diffusion equation describing the relaxation of electron spin is governed by a second-order equation:

$$\frac{\partial^2 \Delta\mu}{\partial x^2} = \frac{\Delta\mu}{\lambda^2} \tag{2.3}$$

where, $\Delta\mu = \mu_\uparrow - \mu_\downarrow$ is the spin-split in the electrochemical potential arising from spin accumulation. $\Delta\mu$ decays in metals due to the presence of Elliot-Yafet[51,93] spin scattering effects.

2.2.2 Spin Accumulation, $\Delta\mu(x)$

From (2.3), the general solution for the spin accumulation $\Delta\mu_i(x)$ in each layer-i can be written as:

$$\Delta\mu_i(x) = P_i \exp(\frac{x}{\lambda_i}) + Q_i \exp(-\frac{x}{\lambda_i}) \tag{2.4}$$

To solve for the coefficients P_i and Q_i in (2.4), we need to apply the boundary relations governing $\Delta\mu_i(x)$ at each interface $x = x_i$ between layers i and $(i+1)$. Assuming no interfacial resistance, the first set of boundary conditions are obtained from the continuity of spin-dependent electrochemical potential at each interfaces, $x = x_i$, i.e.

$$\mu_{(i+1)}(x_i)_{\uparrow,\downarrow} = \mu_i(x_i)_{\uparrow,\downarrow} \tag{2.5}$$

Equation (2.5) can then be expressed in terms of, spin accumulation $\Delta\mu_i(x)$, i.e.

$$\Delta\mu_{(i+1)}(x_i) = \Delta\mu_i(x_i) \tag{2.6}$$

A second set of boundary conditions can be obtained by considering the spin-current across the interfaces. From (2.2), we obtain the following relations on the left (2.7a) and

right-side (2.7b) of the interface at $x = x_i$:

$$\rho_{i\uparrow} j_{i\uparrow}(x) - \rho_{i\downarrow} j_{i\downarrow}(x) = -\frac{1}{e}\frac{\partial \Delta\mu_i(x)}{\partial x}\Big|_{x = x_i} \tag{2.7a}$$

$$\rho_{(i+1)\uparrow} j_{(i+1)\uparrow}(x) - \rho_{(i+1)\downarrow} j_{(i+1)\downarrow}(x) = -\frac{1}{e}\frac{\partial \Delta\mu_{(i+1)}(x)}{\partial x}\Big|_{x = x_i}$$

$$\Rightarrow \rho_{(i+1)\uparrow} j_{i\uparrow}(x) - \rho_{(i+1)\downarrow} j_{i\downarrow}(x) = -\frac{1}{e}\frac{\partial \Delta\mu_{(i+1)}(x)}{\partial x}\Big|_{x = x_i} \tag{2.7b}$$

In the second equality of (2.7b), we have assumed conservation of spin components of current across the interfaces, i.e. no spin-flip scattering occurs at the interfaces, so that $j_{i\uparrow,\downarrow} = j_{(i+1)\uparrow,\downarrow}$. The final boundary conditions are obtained at the terminals, where the spin-accumulation vanishes, i.e.

$$\Delta\mu_1(0) = 0, \Delta\mu_3(x_3) = 0 \tag{2.8}$$

Solving (2.6), (2.7) and (2.8) simultaneously yields the values for the coefficients P_i and Q_i of (2.4), and spin polarization of current $\beta(x_i)$ at the interfaces. Then, from (2.4), the spatial variation of spin-accumulation, $\Delta\mu_i(x)$ for each layer is determined. The spatial profile of $\Delta\mu(x)$ under different conditions are illustrated in Fig. 2.2.

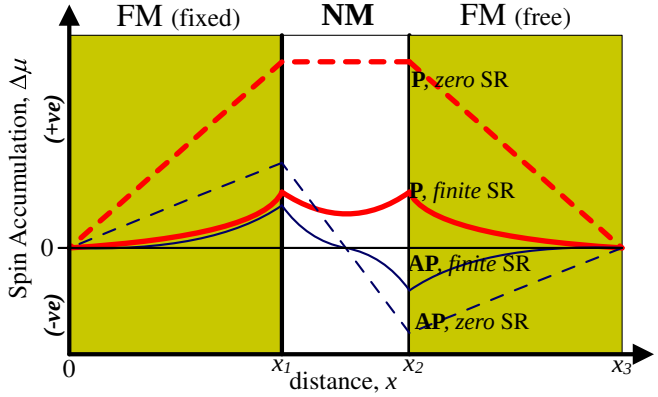

Figure 2.2: Spatial variation of $\Delta\mu$. Thin (thick) lines represent parallel (anti-parallel) configuration. Solid (dashed) line shows the spatial variation of $\Delta\mu$ when the spin relaxation effect is negligible, i.e. $\lambda \rightarrow \infty$(spin relaxation effect is significant, i.e. $\lambda \rightarrow$layer thickness).

2.2.3 Spin-dependent Current Density, $j_{\uparrow,\downarrow}(x)$

To obtain the spatial profile of the $j_{\uparrow,\downarrow}(x)$, we first consider (2.7), at a general x. The spatial variation of β is then given by

$$\begin{aligned} & j\left[\rho_{i\uparrow}\beta_i(x) - \rho_{i\downarrow}\left(1-\beta_i(x)\right)\right] = -\frac{1}{e}\frac{\partial\Delta\mu_i(x)}{\partial x} \\ \Rightarrow \quad & \beta_i(x) = \frac{1}{2} + \frac{\alpha_i}{2} + \frac{1-\alpha_i}{4\lambda_i\rho_i}\left[Q_i\exp\left(-\frac{x}{\lambda_i}\right) - P_i\exp\left(\frac{x}{\lambda_i}\right)\right]. \end{aligned} \tag{2.9}$$

From (2.9) and (2.1a), the spatial variation of the $j_{i\uparrow,\downarrow}(x)$ can be obtained. The spatial variation of current polarization, $\frac{j_\uparrow(x)-j_\downarrow(x)}{j_\uparrow(x)+j_\downarrow(x)} = 2\beta(x) - 1$ is illustrated in Fig. 2.3.

2.2.4 Electrochemical Potential, $\mu(x)$

Note that (2.4) allows us to obtain the spin accumulation $\Delta\mu(x)$ but not the individual spin-up and spin-down electrochemical potentials $\mu_{\uparrow,\downarrow}$. To obtain $\mu_{\uparrow,\downarrow}$, we integrate (2.2), i.e.

$$\mu_{i\uparrow,\downarrow}(x) = -e\int j_{i\uparrow,\downarrow}(x)\rho_{i\uparrow,\downarrow}dx \tag{2.10}$$

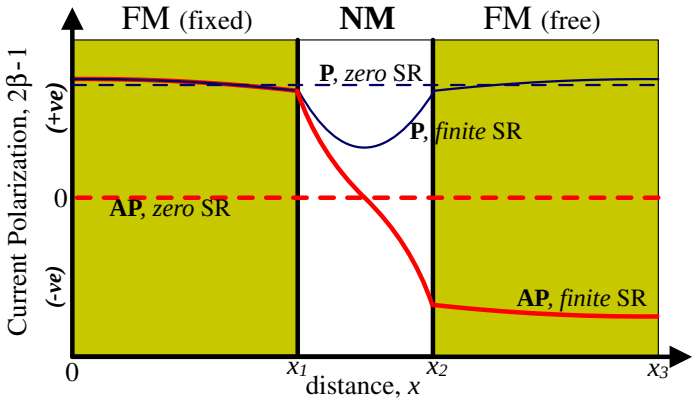

Figure 2.3: Spatial variation of current polarization, $2\beta - 1$. Thin (thick) line represents parallel (anti-parallel) configuration. Solid (dashed) line shows the spatial variation of current polarization when the spin relaxation effect is negligible, i.e. $\lambda \rightarrow \infty$(spin relaxation effect is significant, i.e. $\lambda \rightarrow$layer thickness)).

and substitute the values of $j_{i\uparrow,\downarrow}(x)$ which have been determined earlier. The constants of integration in (2.10) are determined by applying the terminal boundary conditions of $\mu_3(x_3)_\uparrow = 0$ and $\mu_3(x_3)_\downarrow = 0$. The general expression for spin-dependent electrochemical potential is obtained as:

$$\mu_{\uparrow,\downarrow} = \mu_0 + \delta\mu_{\uparrow,\downarrow} \equiv M + Nx + R_{\uparrow,\downarrow} \exp\left(\frac{x}{\lambda}\right) + S_{\uparrow,\downarrow} \exp\left(-\frac{x}{\lambda}\right), \tag{2.11}$$

The spatial profile of this potential is a result of electric field distribution across the device. However, the respective electrochemical potential for each spin channel deviates from the electrostatic potential due to spin accumulation. This deviation constitutes the non-linear part of the electrochemical potential. The spin-independent/ electrostatic/ ohmic/ linear part of the potential is given by $\mu_0 = M + Nx$ and the spin-dependent potential/non-linear part is given by $\delta\mu_{\uparrow,\downarrow} = R_{\uparrow,\downarrow} \exp(x/\lambda) + S_{\uparrow,\downarrow} \exp(-x/\lambda)$. Figure 2.4 illustrates the spatial variation of $\mu^{\uparrow,\downarrow}$ and μ_0.

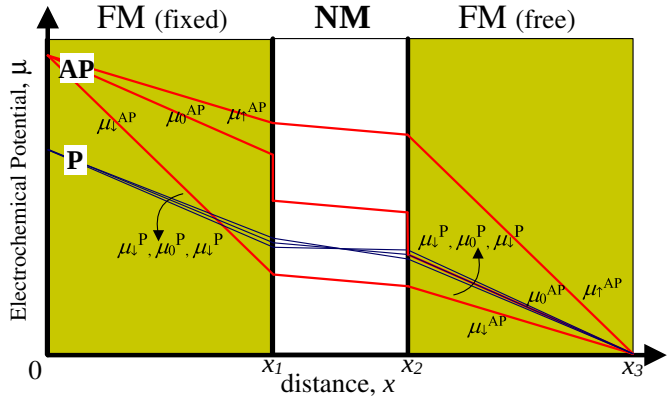

Figure 2.4: Spatial variation of electrochemical potential. Thin (thick) line represents parallel (anti-parallel) configuration. Infinite λ is used. For finite λ, $\mu_{\uparrow,\downarrow}$ varies exponentially, while μ_0 remains linear.

2.2.5 Magnetoresistance, MR

In the anti-parallel (AP) configuration, the magnetization orientation of the free FM layer (layer-3) switches to the opposite direction compared to that of the fixed layer (layer-1). Therefore, the spin-up electrons will experience the minority spin-resistivity, $\rho_{\downarrow}$ in the free layers. Thus, the resistivities experienced by spin-up and spin-down electrons in the free layers in AP configurations are given by $\rho^{\mathrm{AP}}_{i(\uparrow,\downarrow)} = \rho_{i(\downarrow,\uparrow)}$. The MR ratio of the device is defined by

$$MR = \frac{R^{AP} - R^{P}}{R^{AP}} \tag{2.12}$$

where R^{AP} and R^{P} refers to the overall resistance in the anti-parallel(AP) and parallel(P) configurations, respectively. In our analysis, we have i) considered a constant-current model, i.e. j is constant; ii) assumed zero spin-accumulation at both terminals $[\Delta\mu_1(0) = 0, \Delta\mu_3(x_3) = 0]$, and iii) set the potential to be ground at $\mu_3(x_3)_{\uparrow,\downarrow} = 0$. Following these assumptions, we have the relation $R \propto \mu_{1(\uparrow,\downarrow)}(0)$. Hence the MR can be expressed as

$$MR = \frac{\mu^{\mathrm{AP}}_{1\uparrow}(0) - \mu^{\mathrm{P}}_{1\uparrow}(0)}{\mu^{\mathrm{AP}}_{1\uparrow}(0)} \tag{2.13}$$

From the above derivation, the analytical expression of MR for the device in Fig. 2.1 is obtained as follows:

$$MR = \frac{\alpha_F^2 \left(\frac{\rho_N}{\rho_F}\right)^2 \lambda_F^2 \lambda_N \sinh^2\left(\frac{d_F}{\lambda_F}\right)}{\left(\frac{\rho_N}{\rho_F}\lambda_F \cosh\left(\frac{d_N}{2\lambda_N}\right)\sinh\left(\frac{d_F}{\lambda_F}\right) - (1-\alpha_F^2)\lambda_N \cosh\left(\frac{d_F}{\lambda_F}\right)\sinh\left(\frac{d_N}{2\lambda_N}\right)\right) \times \begin{pmatrix} (1-\alpha_F^2)\cosh\left(\frac{d_F}{\lambda_F}\right)\cosh\left(\frac{d_N}{2\lambda_N}\right)\left(\frac{d_N}{2}\lambda_N + d_F\lambda_N\frac{\rho_N}{\rho_F}\right) + \\ \frac{\rho_N}{\rho_F}\lambda_F \sinh\left(\frac{d_F}{\lambda_F}\right)\left(\alpha_F^2\lambda_N\cosh\left(\frac{d_N}{2\lambda_N}\right) + \frac{d_N}{2}\sinh\left(\frac{d_N}{2\lambda_N}\right)\right) + \\ d_F\left(\frac{\rho_N}{\rho_F}\right)^2 \lambda_F \sinh\left(\frac{d_F}{\lambda_F}\right)\sinh\left(\frac{d_N}{2\lambda_N}\right) \end{pmatrix} \tag{2.14}$$

When spin relaxation effect is neglected, i.e $\lambda_{F,N} \to \infty$, (2.14) can be simplified to

$$MR = \left(\frac{2\alpha_F}{2 + \frac{R_N}{R_F}(1-\alpha_F^2)}\right)^2 \tag{2.15}$$

where the areal resistance, $R_{N,F} = \rho_{N,F} d_{N,F}$. This expression is identical to the MR expression obtained by simple two-channel model.

2.3 Influence of Device Parameters on MR

The most straightforward method to enhance the MR is by optimizing the spin transport parameters of the PSV. Therefore, detailed understanding of the fundamental physics as well as the influence of each parameter on MR is essential. In this section we analyze the effect of: i) resistivity (ρ), ii) intrinsic conduction polarization (α), iii) spin-diffusion length (λ) and iV) thickness of each layers (d) on the MR of the PSV device in Fig. 2.1. After analyzing the effects of these parameters, we further study the optimization of these parameters to enhance the MR. Unless otherwise stated, we use Cu and CoFe for NM and FM layer(s), respectively.

It is worth mentioning that our results show generally higher MR values than the experimentally measured MR values of the CPP SV. This is because, for simplicity,

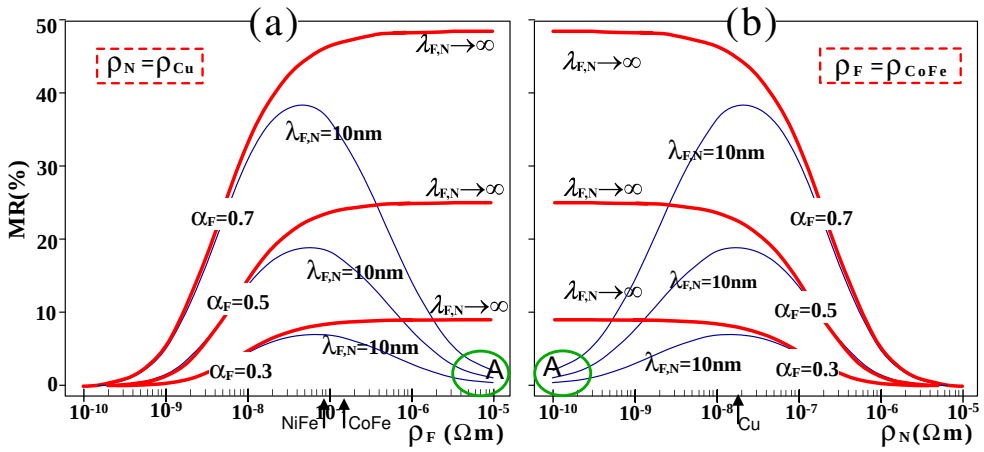

Figure 2.5: (a) MR variation with increasing FM resistivity. (b) MR variation with increasing NM resistivity. Thick (thin) lines indicate the MR when the spin diffusion length, λ is finite (infinite). The circled region, labeled "A" indicates the anomalous MR suppression effect due to spin relaxation.

our studies are deliberately focused on only the active MR region of a CPP SV. In a real device there are other required non-magnetic layers that contribute negatively to the overall MR e.g. the capping and the shield layers, which are not included in our model. In addition to this, in practical devices, the thin film material quality as well as the interfacial effects could also have an adverse effect on the MR.

2.3.1 Effects of Resistivity on MR optimization

To analyze the effect of layer resistivities, we study the MR in the absence of spin relaxation effect, i.e. $\lambda \rightarrow \infty$. Solid lines in Fig. 2.5(a) and (b) show the MR variation when $\lambda \rightarrow \infty$. The expression for MR at this limit is given by (2.15). Fig. 2.5(a) shows an increasing MR of the device with increasing resistivity of the FM layer, ρ_F. Fig. 2.5(b) shows an increasing MR of the device with decreasing resistivity of of the NM layer, ρ_N. As $\rho_F \rightarrow \infty$ or $\rho_N \rightarrow 0$, MR approaches a maximum asymptotic value of α_F^2.

These results can be explained as follows: Note that FM layer is spin-asymmetric ($\alpha_F \neq 0$), and NM layer is spin-symmetric ($\alpha_N = 0$). Spin-asymmetry refers to the degree of spin-dependent electron scattering. High α value indicates high spin-asymmetry of a layer. Overall high spin-asymmetry of a device will cause a large imbalance between the spin-down and spin-up electron population and hence results in high current polarization, β and high MR ratio.

Because FM layer is spin-asymmetric ($\alpha_F \neq 0$), increasing the resistivity of FM layer increases the average spin asymmetry of the entire structure. Since MR is caused by the asymmetry in spin transport, the increase in FM resistivity increases the MR ratio. Unlike FM, NM is spin-symmetric ($\alpha_N = 0$). Therefore increasing the resistivity of NM layer, decreases the average spin asymmetry of the entire structure and thus reduces the MR ratio.

These results also indicate that the resistivity of a particular layer affects the contribution of the spin-scattering of that layer to the overall spin transport of the device. As the resistivity of a layer increases, the spin scattering of that layer dominates the overall spin transport in the device. An increase in the resistivity of the FM (NM) layers will thus increase (decrease) the overall spin-dependence of electron scattering, and produce the expected trend of higher (lower) MR with increasing FM (NM) resistivity.

2.3.2 Effects of Conduction Polarization on MR optimization

Increase in α_F, increases the spin-asymmetry of FM layer, and thus MR of the device is enhanced as shown in figures 2.5(a) and (b). Therefore, in general, high spin-asymmetric materials such as half-metals (HM) are desirable to enhance MR.

2.3.3 Effects of Spin Diffusion Length (SDL) on MR optimization

The effects of spin relaxation are shown by the thin lines in the figures 2.5(a) and (b). Decrease in λ, i.e. increase in spin relaxation, causes two effects: 1) reduction in overall MR, and 2) an anomalous suppress of MR for high (low) FM (NM) resistivity. High spin relaxation reduces spin polarization and thus decreases the spin-asymmetry of the PSV. Therefore we obtain the overall reduction in MR [effect-1]. The physics of anomalous MR suppression [effect-2] is much complicated and it is studied in detail in this section. We represent the spin-dependent transport across a SV structure as described by the SDD theory by an effective two-channel model, in which the spin relaxation effects are globally absorbed into the two effective branch resistances. We found that i) the overall MR is much more sensitive to the spin relaxation effect in the NM layer, compared to that in the FM layers, and that ii) the effective SDL, λ_E in the NM layer is intrinsically linked to the resistivity of the NM and FM layers by $\lambda_E = \lambda_N \left(\rho_N/\rho_F\right)^{1/2}$. The analytical coupling between spin relaxation and resistivity explains the anomalous high-resistance suppression of MR when the resistivity ratio η exceeds a certain critical value η_C.

The two-channel (TC) model provides a global model of spin transport in SVs, that has successfully reproduced many experimentally observed trends. However, the TC model is valid only in the limit of infinitely long SDL, i.e. $\lambda \rightarrow \infty$. In the presence of finite λ, the constraint becomes more complicated than simply specifying the resistance ratio of each spin branch. Given the usefulness of the TC model, there have been previous attempts[94,95] to retain its basic framework of separate spin branches, while making modifications to account for the finite λ value. These take the form of introducing finite spin-flip resistances that connect the two spin branches. The disadvantage of this approach is that i) the interconnections reduce the globally diffused nature of spin relaxation to localized spatial positions, and ii) it complicates the TC model and lessens its usefulness as an analytical tool. We have developed an effective TC model that does not require spin-flip resistances interconnecting the two spin branches to represent spin transport, necessarily avoiding the problems associated with artificially localizing the spin relaxation process.

We applied the SDD method as outlined in Sec. 2.2 to obtain the resistances R^{P} and R^{AP}, respectively, for the P and AP configurations, in the case of finite λ. How-

ever, the exact expressions are complex and not useful in elucidating the effect of spin relaxation on MR, and the relationship between λ and resistivity ρ. Instead, we take the Taylor expansion in the limit of small λ. This limit is applicable for practical SV devices, since the SV multilayer thicknesses are, in general, significantly smaller than λ of the FM or NM layers. We found that the approximate R^{P} and R^{AP} can be mapped to an equivalent TC circuit model, thus yielding the effective resistances experienced by the majority and minority spin electrons, in the case of a finite λ.

Unlike previous models,[94,95] our effective TC model incorporates the distributed effect of spin relaxation across all layers of the PSV as a global influence on the MR of the SV device. In addition, the model is particularly useful for explaining several physical phenomena, e.g. why the overall MR is more strongly influenced by spin relaxation in the NM as opposed to that in the FM layers, and the change in the effective SDL, λ_E as a function of the resistivity ratio ($\eta = \rho_N/\rho_F$) of the NM and FM layers.

We found that the latter underlies the anomalous suppression of MR[96,97][refer Fig. 2.5], when the resistivity of the FM layer exceeds a certain critical value. This effect clearly diverges from the conventional TC model, which predicts a monotonic increase of MR with FM resistivity, to an asymptotic limit. There have been previous works, e.g. by Fert et al.,[26,37] which investigated the MR behavior in CPP multilayers in the presence of λ. However, to our knowledge, none has specifically addressed the underlying reason for the anomalous MR trend.

2.3.3.1 Results and Discussion

Applying the SDD derivations in Sec. 2.2 we obtain the expression for $R^P = \mu^P/j$ and $R^{AP} = \mu^{AP}/j$ as follows:

$$R^P = \rho_F \frac{\left(\begin{array}{c} \eta(d_N + 2d_F\eta)\lambda_F \cosh\left(\frac{d_N}{2\lambda_N}\right)\sinh\left(\frac{d_F}{\lambda_F}\right) \\ +\lambda_N(1-\alpha_F^2)(d_N + 2d_F\eta)\cosh\left(\frac{d_F}{\lambda_F}\right) \\ +2\alpha_F^2\lambda_N\lambda_F\eta\sinh\left(\frac{d_F}{\lambda_F}\right)\sinh\left(\frac{d_N}{2\lambda_N}\right) \end{array} \right)}{\eta^2\rho\lambda_F\cosh\left(\frac{d_N}{2\lambda_N}\right)\sinh\left(\frac{d_F}{\lambda_F}\right) + (1-\alpha_F^2)\eta\lambda_N\cosh\left(\frac{d_F}{\lambda_F}\right)\sinh\left(\frac{d_N}{2\lambda_N}\right)} \tag{2.16}$$

$$R^{AP} = \rho_F \frac{\left(\begin{array}{c} (1-\alpha_F^2)(d_N + 2d_F\eta)\lambda_N \cosh\left(\frac{d_F}{\lambda_F}\right)\cosh\left(\frac{d_N}{2\lambda_N}\right) + \\ 2\alpha_F^2\eta\lambda_F\lambda_N\sinh\left(\frac{d_F}{\lambda_F}\right)\cosh\left(\frac{d_N}{2\lambda_N}\right) + \\ \lambda_F\eta(d_N + 2d_F\eta)\sinh\left(\frac{d_F}{\lambda_F}\right)\sinh\left(\frac{d_N}{2\lambda_N}\right) \end{array} \right)}{\eta(1-\alpha_F^2)\lambda_N\cosh\left(\frac{d_F}{\lambda_F}\right)\cosh\left(\frac{d_N}{2\lambda_N}\right) + \eta^2\lambda_F\sinh\left(\frac{d_F}{\lambda_F}\right)\sinh\left(\frac{d_N}{2\lambda_N}\right)} \tag{2.17}$$

where $\eta = \rho_F/\rho_N$. Note that the expression for MR$= (R^{AP} - R^P)/R^{AP}$ [(2.14)] is a function of the resistivity ratio η, instead of the individual ρ_F or ρ_N values, which indicates experimental facts that MR of a SV is related to the ratio of the resistive change to the total resistance.

In order to elucidate the effect of finite λ_F and λ_N, we first consider the limiting case of small spin relaxation i.e. $(d_F/\lambda_F) << 1$ and $(d_N/\lambda_N) << 1$. This limit is usually approached in a practical SV device, due to the small layer thickness of typically a few nanometers. In this limit, R^P and R^{AP} in (2.16) and (2.17) can be approximated by taking the first-order Taylor's expansion of the hyperbolic function terms, which yields

$$R^P = \frac{d_N^2(1-\alpha_F^2) + 4d_N d_F\eta + 4d_F^2\eta^2}{d_N\eta(1-\alpha_F^2) + 2d_F\eta^2}\rho_F \tag{2.18a}$$

$$R^{AP} = \frac{d_N^2 d_F\eta + 2d_N d_F^2\eta^2 + 4d_F\eta\lambda_N^2 + 2d_N\lambda_N^2(1-\alpha_F^2)}{2\lambda_N^2\eta(1-\alpha_F^2) + d_N d_F\eta^2}\rho_F \tag{2.18b}$$

Interestingly, in the first-order expansion, R^P and R^{AP} and hence MR are independent of λ_F. This means that spin relaxation within the NM layer has a much more significant effect on the MR compared to that in the FM layers. Additionally, the first-order approximation of R^P is also independent of λ_N, while R^{AP} approaches the two-current limit of $R^{AP} = \frac{d_N(1-\alpha_F^2)+2d_F\eta}{\eta(1-\alpha_F^2)}\rho_F$ in the limit of vanishing spin relaxation, i.e. $\lambda_N \to \infty$. These are important results that will be used later to explain the numerically observed MR behavior. To map R^{AP} to an equivalent TC model, we reexpressed (2.18b) as a linear combination of R_N, $R_{F\downarrow}$ and $R_{F\uparrow}$ i.e.

$$R^{AP} = \frac{1+g(\lambda_N)}{1+f(\lambda_N)}R_{F\uparrow} + \frac{1}{1+f(\lambda_N)}R_{N\uparrow} + \frac{1+g(\lambda_N)}{1+f(\lambda_N)}R_{F\downarrow} \tag{2.19}$$

where $R_{F\uparrow(\downarrow)} = d_F\rho_{F\uparrow(\uparrow)}$ and $R_{N\uparrow} = d_N\rho_{N\uparrow} = 2d_N\rho_N$ are the discrete resistances in the TC circuit, corresponding to the majority(minority) FM, and NM layer resistances, respectively. The coefficients $f(\lambda_N)$ and $g(\lambda_N)$ in (2.19) are respectively given by $f(\lambda_N) = \frac{d_N d_F}{2\left(\lambda_N/\sqrt{\eta}\right)^2(1-\alpha_F^2)}$ and $g(\lambda_N) = \frac{d_N^2}{4\lambda_N^2} + \frac{d_N^2}{2\left(\lambda_N/\sqrt{\eta}\right)^2}$. From (2.19), we can construct a TC circuit in the presence of λ_F, as represented schematically in Fig. 2.6, where the resistance seen by the spin-up and down currents are $R_\uparrow^{AP} = R_\downarrow^{AP} = 2R^{AP}$.

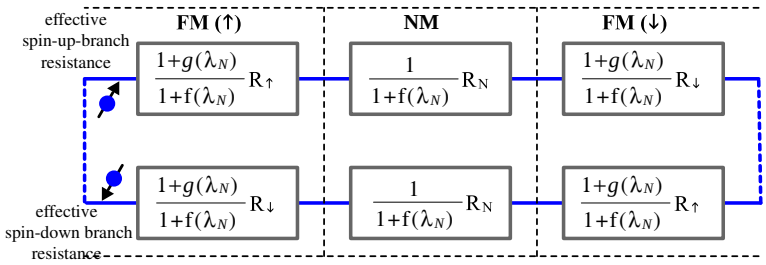

Figure 2.6: Schematic illustration of the spin up and down current in a SV trilayer with antiparallel magnetization alignment in the ferromagnetic layers.

In this way, we have transformed the complicated system obtained with SDD

theory to a simple TC circuit with the global effect of λ absorbed into the effective branch resistances. Our method avoids the need to localize the effect of spin relaxation at some arbitrary points, e.g. at the boundary between the FM and NM layers, as was done previously.[94,95] By examining the forms of $f(\lambda_N)$ and $g(\lambda_N)$ and (2.19), we can deduce that an increase in $\eta = \rho_F/\rho_N$ will increase the relative contribution of the NM layer resistance compared to that of the FM layer, and suppresses the overall MR. Furthermore in the case of large η (due to small ρ_N), both $f(\lambda_N)$ and $g(\lambda_N)$ become effectively a function of $\lambda_E = \left(\lambda_N/\sqrt{\eta}\right)$. We can thus regard λ_E as the effective spin relaxation length, which is dependent on the FM and NM resisitivity. Thus, for the case of a finite λ_N, an increase in the FM resistivity (i.e. increase in η) will lead to two competing effects: i) an increase in the spin-dependence of bulk scattering in the FM layers, and hence a positive impact on MR, and ii) an amplification of the effect of spin relaxation within the NM layer, which tends to moderate the increase of MR due to (i). It is effect (ii) which leads to the numerically observed anomalous suppression of MR at high FM layer resistivity values.

We will now utilize the earlier analysis leading up to the model, to clarify certain MR trends obtained from the full SDD theory. We first calculate the MR values as a function of ρ_N, for different values of ρ_F in Fig. 2.7. All the MR curves show the anomalous behavior, in which the MR ratio reaches a maximum at some critical NM resistivity ρ_N. Beyond this critical value, the MR ratio begins to decrease and diverge from the saturation MR value (as represented by the thin line), as predicted by the TC limit i.e. for infinitely long λ_F and λ_N. Note that the MR curves corresponding to different ρ_F values have the same profile, and are merely translated along the x- axis. This agrees with the MR expression [refer (2.16) and (2.17)], in which the MR ratio

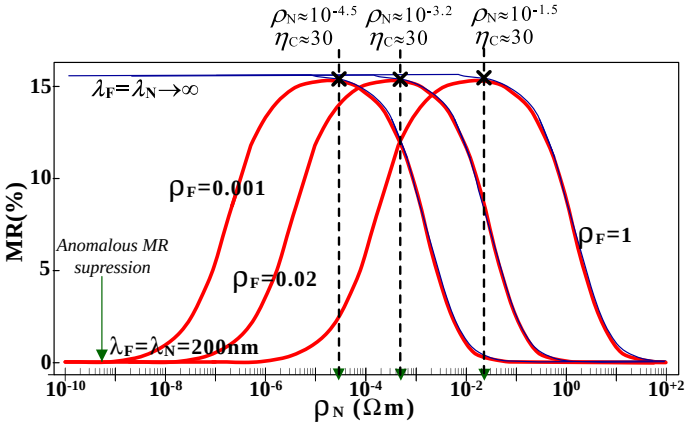

Figure 2.7: MR vs. ρ_N for different ρ_F. Thin (Thick) line shows the results without(with) spin relaxation effect. "X" indicates the point where anomalous effect begins, i.e. $\rho_F/\rho_N \approx \eta$. Dotted arrows indicate the region which shows anomalous behavior. $\alpha_F = 0.4$, $\lambda_F = \lambda_N = 200nm$.

is dependent only on the resistivity ratio η. Thus, at the points marked as "X", which coincide with the onset of the MR decrease, the critical resistivity ratio, $\eta_C \approx 30$ is found to be constant for all the MR curves.

The critical resistivity ratio η_C is a crucial quantity for studying the performance of SV devices, since it corresponds to the maximum MR ratio. Hence, we investigate the dependence of η_C on the spin diffusion lengths λ_F and λ_N. Figure 2.8 plots the calculated MR curves based on the full SDD equations, and shows the change in η_C as λ_F and λ_N are varied. We first vary λ_F while keeping λ_N fixed at some large value $(10^4 nm)$. For small λ_F (λ_F is comparable or smaller than d_F), the MR value is small because spin relaxation within the FM layers reduces the spin polarization of current. When λ_F is increased, the MR ratio increases and eventually saturates when $\lambda_F > 20nm$. At these λ_F values, $(d_F/\lambda_F) \approx 0.2$, so that the first-order Taylor expansion [used in deriving (2.18a) and (2.18b)] become reasonably accurate. The MR saturation at the relatively low value of λ_F confirms our earlier finding that the MR is to a first-order approximation, independent of λ_F. A further indication of the relative insensitivity

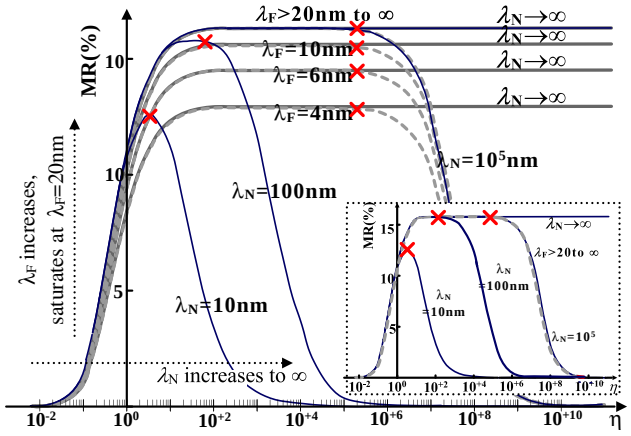

Figure 2.8: MR vs. η obtained with the full SDD equations for different λ. "X" indicates the point where anomalous effect begins, $\rho_F/\rho_N \approx \eta$. $\alpha_F = 0.4$. Inset: MR vs. $\log \eta$ obtained with the effective model for different λ.

of MR to λ_F is shown by the fact that η_C does not significantly vary with an increase of λ_F.

Next, we analyze the effect of λ_N on the η_C and the maximum MR ratio. We fix λ_F to be infinitely large, and increase λ_N from 10 to $10^4 nm$. Similar to the case of λ_F, we find that an increase in λ_N will improve the maximum MR ratio due to the reduction in spin relaxation. In addition, the maximum MR value saturates at large $\lambda_N \gg d_N$. However, there are two differences in the MR dependence on λ_N compared to its dependence on λ_F: i) The maximum MR reaches saturation at a much higher value of λ_N i.e. in excess of $100nm$, whereas saturation of MR has already occurred for $\lambda_F = 20nm$; ii) In addition, the critical value of η_C at which the MR starts to decrease is shifted to progressively higher values as λ_N is increased, but is insensitive to an increase in λ_F. These two differences thus affirm our earlier analysis that spin relaxation within the NM layer has a much stronger influence on the overall MR. From practical standpoint, this is a significant result, since it suggest that the effort to enhance MR via improvement to material quality should be focused on the NM spacer, instead

of FM layers.

We also observe from Fig. 2.8 that the anomalous decrease in MR at high FM resistivity (i.e. at high η) occurs for all finite values of λ_N. Furthermore, the decrease in MR disappears only when $\lambda_N \to \infty$, regardless of the value of λ_F. This shows that it is the spin relaxation within the NM layer, which is responsible for the anomalous decrease in MR in a SV trilayer. This behavior can be explained analytically by examining (2.18a) and (2.18b) , under three scenarios: i) In the absence of any spin relaxation i.e. $\lambda_{N,F} \to \infty$, the MR saturates at $\alpha_F^2 (= 16\%)$ when $\eta \to \infty$. ii) In the case of finite λ_N value, i.e. with spin relaxation in the NM layer, the MR falls to zero when $\eta \to \infty$. This decrease occurs regardless of the λ_F value, i.e. even at infinite λ_F. iii) When spin relaxation is eliminated from the NM layer, i.e. infinite λ_N, it can be shown that the anomalous behavior vanishes, i.e. the MR no longer decreases to zero when $\eta \to \infty$. Instead, from the SDD theory, the MR can be shown to converge to an asymptotic value of

$$\begin{aligned} MR &= \frac{(e^{2d_F/\lambda_F}-1)\alpha_F\lambda_F^2}{(e^{2d_F/\lambda_F}-1)\alpha_F\lambda_F^2 - d_F(\alpha_F^2-1)(e^{2d_F/\lambda_F}+1)} \\ &\approx \alpha_F^2 - \frac{1}{3}\alpha_F^2\left(1-\alpha_F^2\right)\left(\frac{d_F}{\lambda_F}\right)^2 + \mathrm{O}\left(\frac{d_F}{\lambda_F}\right)^4 \overset{\lambda_F\to\infty}{\to} \alpha_F^2, \end{aligned} \tag{2.20}$$

where the approximation is valid for thin layer thickness $(d_F/\lambda_F) \gg 1$, which is the limiting case assumed in deriving (2.18a) and (2.18b).

Note that the λ_F dependence of the asymptotic MR value of (2.20) is only of the second-order, which agrees with our previous analysis. It's worth noting here that we have used the theoretical analysis that led to the construction of the effective model to explain the underlying physics of the full numerical results of Fig. 2.7 and Fig. 2.8 which give important information to SV device experimentalists. Last, to confirm that

the effective model approximates the full SDD model, we repeated the numerical studies of Fig. 2.8 using the effective model. Results (inset of Fig. 2.8) show close approximation to that of Fig. 2.7, thus confirming that the simplified effective model has indeed provided the necessary decompositions to accurately explain the many MR behaviors, including its suppression at high resistance.

2.3.3.2 Conclusion

We have developed an effective TC model that does not require spin-flip resistances interconnecting the two spin branches to represent spin transport, necessarily avoiding the problems associated with artificially localizing the spin relaxation process. With this model, we deduced that an increase in the FM resistivity leads to a positive effect on MR. However, this trend is counter-acted by the corresponding amplification of spin relaxation within the NM layer, which depresses MR. The competition between these two effects underlies the anomalous suppression of MR at high FM layer resistivity values. A numerical simulation based on the SDD reveals that the decrease in MR disappears only when $\lambda_N \rightarrow \infty$, regardless of the value of λ_F. This is in agreement with our effective TC model, which shows that i) the branch resistances and hence MR are dependent (to the first order) on spin relaxation only within the NM layer, and that ii) the effective spin relaxation varies as $\lambda_E \propto \eta^{-1/2}$. In general, the TC model predicts that MR is much more sensitive to λ_N compared to λ_F. This analytical prediction is further supported by numerical calculations based on the full SDD model which show that MR saturates at a relatively low value of λ_F, and that the critical η_C corresponding to maximum MR does not vary significantly with λ_F. From a practical standpoint, these results suggest that efforts to enhance MR via improvement to material quality should

be focused on the NM spacer for small spin diffusion length.

2.3.4 Layer Thickness

Next, in this section we perform a theoretical study and analysis on the effect of modifying the layer thicknesses of a PSV on its MR ratio. An increase in the FM layer thickness results in i) an increase in the spin dependent component of its total resistance, thereby resulting in higher MR, but also leads to ii) greater spin relaxation in that layer, and iii) an anomalous MR effect in the high resistance regime, both of which–(ii) and (iii)– suppress the MR ratio. The interplay of these three effects results in a complex MR dependence on FM thickness, instead of the simple monotonic MR increase predicted by the TC model. It also explains the existence of an optimum FM thickness for maximum MR ratio, as evidenced by experimental data. The study of the combined effects of the FM layer thickness and resistivity, as well as the MR suppression in the high resistive limit is essential for optimizing the structure and material of a practical CPP SV to achieve high MR ratio.

In this section, we investigate the effects of varying the FM layer thickness (d_F) on the MR of a CPP device for the following reasons: i) there is room for an increase in d_F even for terabit density storage, since the layer thickness is much smaller than the lateral dimensions, and ii) there is an optimum value of d_F which maximizes the MR ratio, which has not been determined previously. It is well-known within the TC model[26] that a larger d_F increases the spin-dependent scattering of the conduction electron, and thus increases the overall MR. However, this increase in MR with d_F does not proceed indefinitely, due to the effect of spin relaxation which is not included in the TC model. Thus, a larger d_F also increases the spatial distance over which the electron spin relaxes, and thus results in a lower MR. It would thus be of interest to study the competition between these two effects on the overall MR behavior of a CPP sensor as the FM thickness d_F is varied. In addition, the effect of d_F on MR is further complicated by the existence of the MR suppression behaviors [refer Sec. 2.3.3], which lead to a decrease in MR with increased FM resistance even when the amount of spin relaxation is kept constant. These anomalous MR effects become especially significant for higher device resistance. The

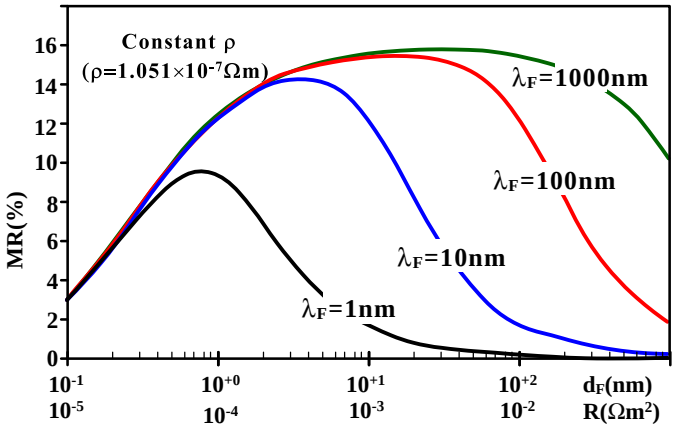

Figure 2.9: MR increases with increasing FM thickness for thickness, d_F much smaller than the λ_F. For thickness larger than the spin diffusion length, MR decreases due mainly to the effect of spin relaxation in FM. For very large thickness, MR fall could have been due to both spin relaxation as well as the anomalous MR behavior.

resultant effects of all the above mentioned factors on the CPP MR would be analyzed theoretically in this section.

2.3.4.1 Results and Discussion

Figure 2.9 shows the change of MR with increasing FM resistance due to increasing thickness d_F. It is seen that at small FM thickness, the MR scales with increasing d_F. This is because the increased FM thickness implies a greater proportion of spin-dependent (momentum) scattering in the overall device, and results in a higher MR. However, at some critical thickness, the MR peaks before decreasing at larger values of d_F. The critical thickness is closely related to the spin relaxation of electrons in the FM layer. When d_F exceeds the λ_F, the effect of spin relaxation of electrons becomes increasingly significant. Thus, although the increased travel length for electrons in the FM increases spin-dependent momentum scattering which favors an MR increase, it also increases spin relaxation due to the Yafet-Elliot[51,93] effects which favors a decrease in MR. It can thus be summarized that when d_F becomes comparable or larger than

the λ_F, a competition between the above two effects occurs. To further illustrate these competitive effects on MR, we repeated the calculations for larger λ_F values. Larger λ_F values imply weaker spin relaxation effects in the FM layers, and thus delay the onset of the MR decrease due to spin relaxation. An inspection of Fig. 2.9 shows that increasing λ_F indeed shifts MR peaks to the right, thus lending credence that the overall MR trend is primarily due to the competition between spin-dependent momentum scattering and spin relaxation effects.

Since an increase in d_F leads to a concomitant increase in the FM resistance, it is thus reasonable to believe that the drop in MR is due not only to the effect of spin relaxation, but also the anomalous MR trend at high resistance. Thus, it is useful to separate out the contributions of these two effects in the suppression of MR. To achieve this, we applied two means of varying the resistance of the FM layers i.e. i) by increasing d_F while keeping resistivity ρ_F of the FM material constant (as before), or ii) by increasing ρ_F while keeping d_F constant. We found that the two methods of varying the resistance result in similar trends of MR but significantly different values of critical resistance where maximum MR occurs, as shown in Fig. 2.10.

The MR suppression effect is clearly manifested in the MR variation due solely to changing ρ_F, while keeping d_F constant (dotted curves of Fig. 2.10). Since d_F is constant, the degree of spin relaxation remains the same, and we thus expect MR to increase montonically with ρ_F. However, all the dotted MR curves reach a maximum before decreasing to zero at large ρ_F. Thus, one can surmise that the value corresponding to the maximum MR marks the point where the anomalous MR suppression becomes strong enough to offset the gain in MR due to increasing FM resistance. We also observed in

Fig. 2.10, that the decrease of MR at high resistance R_F is more rapid by solely increasing the thickness d_F of the FM layer, instead of solely increasing the resistivity ρ_F. This is because in the former, MR is suppressed by both the anomalous MR effect and the spin relaxation within a larger spatial volume, while in the latter, MR is suppressed by the anomalous effect alone. The large divergence between the two indicates that spin relaxation is a much stronger effect compared to the anomalous MR effect in suppressing the MR ratio. This is consistent with previous findings [Sec. 2.3.3] which show that the anomalous MR effect is relatively weak and becomes significant only when the FM resistance is extremely large. We can thus infer from the results of Fig. 2.9 and Fig. 2.10 that the MR variation under the combined influence of the increase in length d_F and resistance R_F of the FM layers falls under three regimes: i) at low d_F (and hence low R_F, the increase in spin-dependent momentum scattering dominates and causes an MR increase with d_F), ii) when d_F exceeds the λ_F, the spin relaxation effect becomes more dominant and MR peaks and starts to decrease and iii) at very large d_F such that the overall resistance is also very large, the MR decrease is more rapid, due to the combined spin relaxation and the anomalous resistance effects.

An interesting point to note in Fig. 2.10 is that at small resistance R_F, the increase in MR due solely to increasing d_F almost coincides with that due to ρ_F increase alone (i.e. matching between dotted and solid lines). This is expected because at small FM thickness, the spin relaxation effect is negligible, and so an increase in either d_F or ρ_F will result in the same effect i.e. increased spin-dependent scattering. The only exception occurs for the case of extremely short λ_F of $1nm$. This is due to the significant spin relaxation for the case of constant d_F (dotted), since the chosen d_F value of $4nm$ is significantly larger than the λ_F.

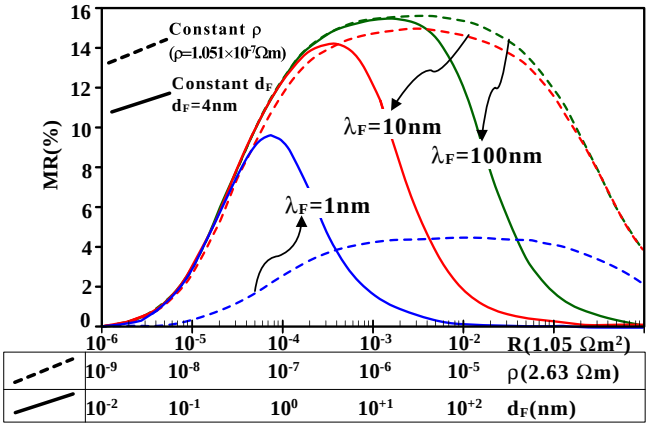

Figure 2.10: MR is studied by either varying d_F or resistivity ρ_F Both quantities are labeled in the different x-axes, as well as the corresponding resistance. The FM polarization is kept constant at 0.4. The MR falls drastically with d_F increases beyond the λ_F. The MR falls much more slowly with increasing resistance due solely to increasing resistivity, clearly showing that anomalous effect is weak and becomes significant only at very high resistance.

To investigate the effect of MR decrease due solely to the spin relaxation effect without the anomalous resistance effects, it would be necessary to keep the total R_F constant while increasing d_F. Figure 2.11 shows MR decreases with increasing d_F as resistivity ρ_F is decreased correspondingly to keep the areal resistance (R_F) constant. For all λ_F values, the MR is maximum at low d_F where there is negligible spin relaxation. As expected, the MR begins to decrease when d_F is comparable to λ_F. Comparing the MR variation of Fig. 2.11 with the solid MR curves of Fig. 2.10, we find that the decrease in MR at high R_F in both cases to be fairly similar. For instance, for both cases, the MR ratio is approximately halved at $d_F \sim (2\lambda_F)$. This thus confirms our earlier observation that spin relaxation is the dominant mechanism for the drop in MR ratio.

2.3.4.2 Conclusion

Based on the SDD equation, we have studied the interplay between spin-dependent bulk scattering, spin relaxation and the anomalous MR effect on the overall MR. All these

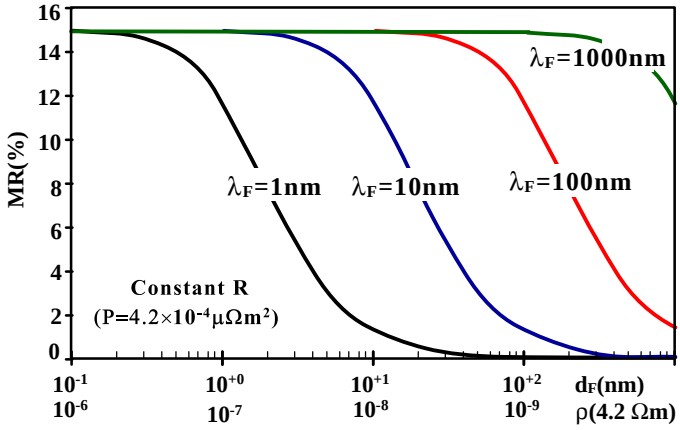

Figure 2.11: FM thickness is increased as resistivity is lowered accordingly to ensure that R_F is constant. Maintaining R_F at a constant value eliminates the anomalous MR effect due to increase in R_F. Thus, the change of MR is due solely to the effect of increasing spatial volume for spin relaxation.

three effects come into play when the FM layer thickness d_F is varied. At small values of d_F, the MR improves with increasing d_F due to greater contribution from bulk spin scattering within the FM layer. But as d_F approaches λ_F, spin relaxation and anomalous MR effects become increasingly prominent and suppress the MR ratio. Our analysis thus reveals the need for a careful optimization of the device geometry and material parameters, in order to achieve the maximum MR ratio.

2.4 Summary

In this chapter, we developed a mathematical model to compute spin accumulation, current polarization, potential variation and MR of a PSV device. Using this model, we analyzed the effect of material parameters on the MR of the device . In our analysis we focused mainly on understanding the physics of spin transport as well as optimizing the material parameters to achieve high MR ratio. We noticed various novel effects, i.e. i) the effect of spin-independent resistivity on spin-asymmetry, ii) an anomalous MR sup-

pression effect due to the coupling of spin relaxation with resistivity and iii) complex interplay between spin-asymmetry, spin relaxation and the anomalous MR suppression effect due to increase in the FM layer thickness. These effects were further utilized to enhance the MR ratio.

Chapter 3

Resistance Competitive Effect

In the previous chapter we studied the optimization of MR in a simple PSV structure. In this chapter we will study the optimization of MR when there are additional resistive components in the device. In a more realistic device the electron scattering at the interfaces between different layers give rise to additional resistive components. In the first section of this chapter, we analyze the effect of such interfacial resistances (IR) unto the MR of the device. In the second section, we propose an alternative method to enhance MR, i.e. by inserting additional layers in the PSV. The effect of such insertion is explored in detail. In both cases, the additional resistive components–IR and additional layers–give rise to an interesting effect, whereby each of the individual resistive components competes with each other in dominating the current polarization and thus the spin asymmetry of the device. The interplay among the different resistive components is termed as "resistance competitive effect". Our results show that this resistance competitive effect plays a very crucial role in MR optimization. We also analyze the interplay between resistance competitive effect and spin-relaxation for further optimization of the MR.

3.1 Effect of Interfacial Resistance

Increasing the spin anisotropic interfacial resistance in devices, and hence the spin-dependent scattering (scattering anisotropy) is an important means of improving MR in the CPP configurations. This is especially crucial for reduced CPP device sizes, because as Valet and Fert[26] have shown, interfacial scattering contributes to the bulk of the CPP-MR at small layer thicknesses of a few nanometers. Thus, the MR in the CPP configuration can be improved by increasing the spin selectivity of interfacial resistances (IR) in the multilayer. A highly spin selective IR also improves the SI efficiency from

FM layers into NM layers, as was predicted theoretically[26,37] and shown experimentally.[98–100] Generally, interfacial electron scattering, whether specular or diffusive, arises naturally in practical devices, due to the presence of e.g. potential steps, crystal defects, and interfacial roughness between adjacent layers.[101] However, in order to utilize the IRs to improve MR and SI efficiency, we need to systematically engineer IRs with the required properties. It has been shown both theoretically and experimentally that IRs may be engineered as either Schottky[37] or tunnel barriers,[37,102] or by the introduction of an ultrathin insulating (nano-oxide) layer.[99] For a CPP trilayer, an increase in the resistivity of the FM layers generally results in greater spin-dependent scattering, and hence higher overall MR. However in the presence of IRs, we conceptualized that increasing the resistance of either the spin-asymmetric IR or of the FM layers does not necessarily result in a higher overall MR. In fact, it is reasonable to conjecture that since both IR and FM provide spin-dependent scattering, a competition effect may arise between these two elements in their contribution to overall device MR.

To investigate this more complicated effect of IR, we perform analytical and numerical studies of spin transport and the MR effect in a CPP configuration, based on the phenomenological SDD equations [refer Sec. 2.2]. Our investigations are focused on the effect of IR on spin transport at the boundaries between the FM and NM layers of a basic PSV trilayer (FM-NM-FM). Our simulation results show that an increase in MR with the magnitude of IR or FM resistivity occurs only for a certain range, which is dependent on parameters such as the spin diffusion length, the intrinsic spin polarization ratio of the FM and NM materials, and the spin-selectivity of the IR. Here, we present two models to study the effect IR. In the first model IR is incorporated by considering potential discontinuities at the interfaces. The limitation of this model is that, spin must

be conserved across the interface, i.e. no interfacial spin-flip. In the second model we further include the effect of interfacial spin-flip by modeling the interfaces as ultra-thin layers, in the limit of the layer thickness approaching zero.

3.1.1 Model I: Without Interfacial Spin-flip

Here, we present a theoretical analysis of the spin transport and MR of a PSV trilayer device, taking into account the effects of IR between layers. We show that MR declines with increasing IR (FM resistivity) when the spin polarization of the IR (FM material) is lower than a critical value. We derive the critical spin polarization analytically, and explain these effects in terms of the relative competition between the bulk FM and IR in providing spin-dependent scattering. We also analyze the interplay between this resistance competitive effect and spin-relaxation in the layers for further optimization of the MR.

3.1.1.1 Theory

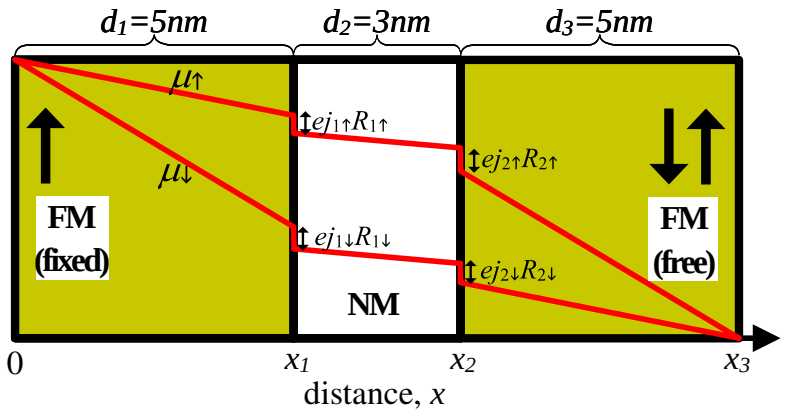

Figure 3.1: Schematic illustration of the trilayer device, consisting of the pinned and free (switchable) FM layers separated by a NM metal spacer layer. The position of the two interfaces is denoted by x_1 and x_2. Electrochemical discontinuity at interfaces is also illustrated.

The presence of IR gives rise to a electrochemical potential discontinuity at the multilayer boundaries as illustrated in Fig. 3.1. This discontinuity is modeled by includ-

ing potential discontinuity in (2.6) such that

$$-ej_{i\uparrow}(x_i)R_{Ii\uparrow} = \mu_{(i+1)\uparrow}(x_i) - \mu_{i\uparrow}(x_i), \tag{3.1a}$$

$$-ej_{i\downarrow}(x_i)R_{Ii\downarrow} = \mu_{(i+1)\downarrow}(x_i) - \mu_{i\downarrow}(x_i), \tag{3.1b}$$

where $R_{Ii\uparrow(\downarrow)} = \rho_{Ii\uparrow(\downarrow)}d_{Ii\uparrow(\downarrow)}$ is the areal IR experienced by majority (minority) spin electrons at interfaces between layers i and $(i+1)$. To simplify our analysis, IR is taken to be spin conserving, i.e. spin flip at the interface is neglected. We would thus like to emphasize that the effect of IR on MR would be qualitatively different than that due to any particular layer of finite thickness and specific SDL.

From (3.1), we can then express the boundary relation in terms of $\Delta\mu_i(x)$, i.e.

$$ej_{i\downarrow}(x_i)R_{Ii\downarrow} - ej_{i\uparrow}(x_i)R_{Ii\uparrow} = \Delta\mu_{(i+1)}(x_i) - \Delta\mu_i(x_i) \tag{3.2}$$

The IR at $x = x_2$ (i.e. boundary between layer-2 and layer-3) in AP configuration is given by $R^{AP}_{I2\uparrow,\downarrow} = R_{I2\downarrow,\uparrow}$. In general the IRs are spin-selective, so that $R_{Ii\uparrow}$ and $R_{Ii\downarrow}$ are different and can be expressed as follows:

$$R_{I\uparrow(\downarrow)} = \frac{2R_I}{1+(-)\gamma} \tag{3.3}$$

where $\gamma = (R_{I\downarrow} - R_{I\uparrow})/(R_{I\downarrow} + R_{I\uparrow})$ is the spin selectivity coefficient of the IR and $R_I = R_{I\uparrow}||R_{I\downarrow}$ refers to the total areal IR. With the IR incorporated as described above, and following the prescriptions of Sec. 2.2, we derive the MR expression which is used in our studies of the interfacial resistance effects.

3.1.1.2 Result and Discussion

3.1.1.2.1 Infinite Spin-Relaxation Length We will first investigate the IR effect in the absence of spin relaxation, i.e. in the limit of SDL approaching infinity. In this limit,

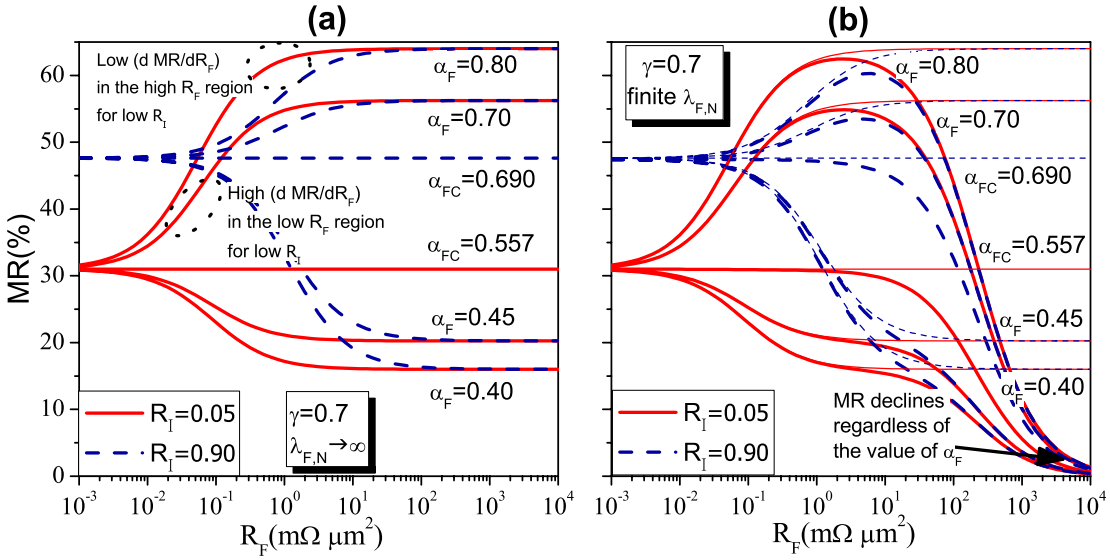

Figure 3.2: (a) Plot of MR ratio as a function of areal resistance R_F of the FM layers, for a PSV trilayer with interfacial resistances. The decrease in MR with increasing FM resistance occurs when $\alpha_F < \alpha_{FC}$. For illustrative purposes, we have calculated the MR versus R_F curves for different α_F values of the FM layer. (b) The thick curves show plot of MR ratio as a function of R_F of the FM layers for a PSV trilayer in the presence of finite spin relaxation in the layers [$\lambda_{CoFe} = 15nm$, $\lambda_{NiFe} = 5nm$ and $\lambda_{Cu} = 140nm$]. The anomalous decrease in MR with increasing FM resistivity occurs at high FM resistivity, regardless of whether α_F is greater or smaller than α_{FC}. The thin curves show the corresponding results obtained in the absence of spin relaxation i.e. $\lambda \rightarrow \infty$.

the spin polarization of current is constant within each layer, and the SDD model simplifies to the TC model. By applying the TC model on a simple FM-NM-FM trilayer, it is clear that an increase in the (spin-asymmetric) resistivity of the FM layers will result in a monotonic increase in MR. However, our results show that such relationship is no longer valid when the effects of IR at the FM-NM boundaries are taken into consideration. As shown in Fig. 3.2(a), the MR ratio can either increase or decrease with increasing FM resistivity, depending on the properties of the IR. For illustrative purpose, we assume two different magnitudes of IR, i.e. $R_I = 0.05m\Omega\mu m^2$ and $R_I = 0.9m\Omega\mu m^2$, but with the same spin selectivity of $\gamma = 0.7$.

Our numerical calculations reveal that, contrary to general expectation, the MR ratio decreases monotonically with FM resistivity for $R_I = 0.05(0.9)m\Omega\mu m^2$ when the

bulk spin polarization of the FM material α_F is less than some critical value $\alpha_{FC} = 0.557(0.690)$. The MR ratio reverts to the normal increasing trend with FM resistivity when α_F exceeds the critical value α_{FC}, which will be derived later.

Another notable feature of Fig. 3.2(a) is that the higher the IR value is, the less sensitive is the overall MR of the device to an increase in the resistance R_F of the FM layers. For instance, in the case of $R_I = 0.05 m\Omega\mu m^2$, the MR ratio undergoes a steep change over the R_F range of between 0.01 and $1 m\Omega\mu m^2 (\Delta MR/\Delta R_F \approx 30.3 m\Omega^{-1}\mu m^{-2})$, whereas for the case of $R_I = 0.9 m\Omega\mu m^2$, the marked change in MR occurs at a significantly higher R_F range of between 0.1 to $10 m\Omega\mu m^2 (\Delta MR/\Delta R_F \approx 1.0^{-1}\mu m^{-2})$. This is because the greater the IR value is, the greater is the contribution of the spin-selective scattering at the interfaces to the MR, thus rendering the device less susceptible to the variation of areal resistance of the FM layers.

The trend of decreasing MR with increasing FM resistivity can be explained in terms of competition between the FM layer resistance and the IRs in contributing to the overall MR of the device. For the case of $\alpha_F > \alpha_{FC}$, the FM layers effectively act as a stronger spin polarizer compared to the IRs. An increase in the resistivity of the FM layers will thus enhance the overall spin-dependence of electron scattering, and produce the expected trend of higher MR with increasing FM resistivity. Conversely, for the case of $\alpha_F < \alpha_{FC}$, the FM layer becomes more weakly polarizing compared to the IRs. Increasing the FM resistivity will increase the resistive contribution of the less spin-polarizing layer, and hence depress the overall MR. This results in the trend of decreasing MR with increasing FM resistivity. If $\alpha_F = \alpha_{FC}$, then both the FM layers and the IRs have the same effective spin polarizing strength. Hence increasing or

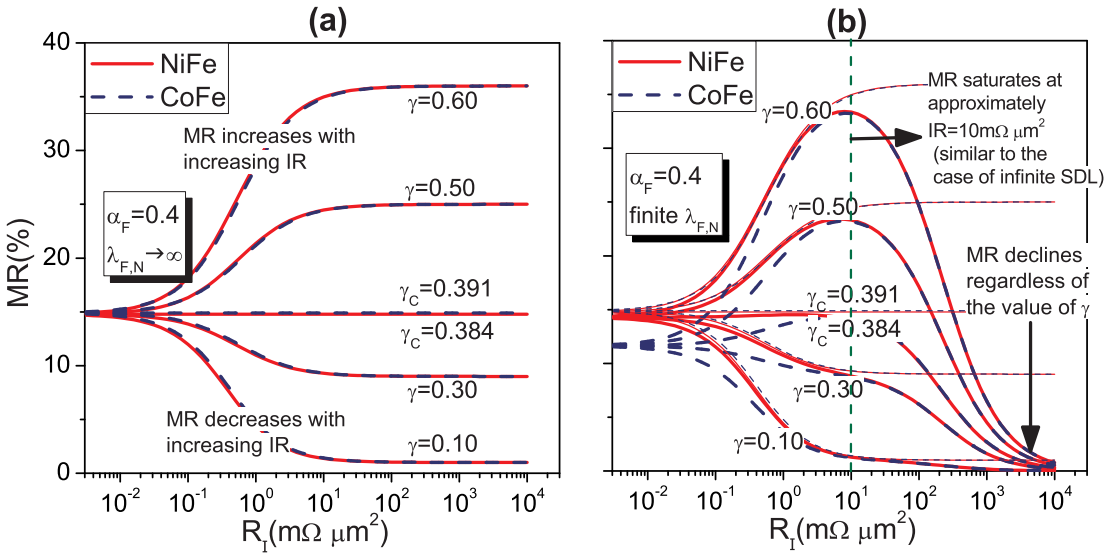

Figure 3.3: (a) Plot of MR ratio as a function of IR for a PSV trilayer with FM layers consisting of either CoFe or NiFe alloy. The decrease in MR with increase in IR occurs when $\gamma < \gamma_C$. For illustrative purposes, we have calculated the MR versus IR curves for different γ values of the interfacial resistance. (b)The thick curves show plot of MR ratio as a function of interfacial resistivity IR, for a PSV trilayer device with NiFe or CoFe as the FM layers, in the presence of finite spin relaxation in the layers [$\lambda_{CoFe} = 15nm$, $\lambda_{NiFe} = 5nm$ and $\lambda_{Cu} = 140nm$]. The decrease in MR with increasing IR occurs at high resistance, regardless of whether γ is greater or smaller than γ_c. The thin curves show the corresponding results obtained in the absence of spin relaxation.

decreasing the FM resistivity, and hence its relative contribution to the overall resistance, will not alter the MR of the trilayer. Note that, as shall be derived later, the critical α_{FC} is not necessarily identical to the spin-selectivity γ of the IRs, because one must account for the additional resistive (but not spin-scattering) contribution of the NM spacer.

In the following, we calculate the MR dependence on the magnitude R_I and spin-selectivity γ of the IRs, the results of which are plotted in Fig. 3.3(a). The MR dependence on R_I and spin-selectivity γ is analogous to its dependence on R_F and α_F of the FM layers, as depicted by Fig. 3.2(a). Thus, below (above) a critical value of γ, i.e. $\gamma < (>)\gamma_C$, we observe a trend of decreasing (increasing) MR with increasing magnitude R_I of the IR, and for $\gamma = \gamma_C$, the MR becomes independent of R_I. When NiFe (CoFe) is used as the FM material, the corresponding value of γ_C is 0.390 (0.384),

which is close to the spin polarization α_F of the FM layer (≈ 0.4). Compared to the critical FM polarization α_{FC} which marks the threshold for the normal trend of increasing MR with FM resistivity, the corresponding critical value for IR spin selectivity γ_C is much lower. This is due to the relatively low spin polarization of a typical FM material of ~ 0.4, compared to the spin-selectivity of IR of ~ 0.7 , which makes it easier for the IR layer to provide a stronger spin-scattering effect to the conduction electrons. One practical implication of these results is that the MR of the CPP device may be enhanced more readily by engineering an increase in the areal resistance of the IRs, rather than by focusing on its spin-selectivity γ , which is already high and hence more difficult to be improved further.

We have earlier qualitatively explained the origin of the trend of declining MR with increasing FM resistivity and magnitude of IR, in terms of the competitive contribution of the FM layers and the IRs to the overall spin-scattering of carriers across the PSV trilayer. By applying the limit of $\lambda_{N,F} \rightarrow \infty$, the analytical derivation of the critical thresholds α_{FC} and γ_C, as well as their dependence on other transport parameters of the device can be obtained. The expression for MR when $\lambda_{N,F} \rightarrow \infty$ is:

$$MR = \left[\frac{2R_I\gamma(\alpha_F^2-1)+\alpha_F R_F(\gamma^2-1)}{2R_I(\alpha_F^2-1)+(2R_F+R_N-\alpha_F^2R_N)(\gamma^2-1)}\right]^2 \tag{3.4}$$

Based on (3.4), we investigate the effect of IR and the FM layer on the MR. First, we derive the expression for α_{FC}. As shown in Fig. 3.2(a), when $\alpha_F < \alpha_{FC}$, MR shows a monotonic decreasing trend with increasing R_F. Therefore, α_F has to fulfill the

following condition:

$$\frac{dM_R}{dR_F} < 0 \Rightarrow \alpha_F < \frac{2\gamma R_0}{2R_0 + R_N(1-\gamma^2)} \equiv \alpha_{FC} \tag{3.5}$$

Conversely, for the behavior of increasing MR with R_F, α_F must be larger than α_{FC}. The critical value of γ_C for the IR spin selectivity can also be derived in a similar way:

$$\frac{dM_R}{dR_0} < 0 \Rightarrow \gamma < \frac{2\alpha_F R_F}{2R_F + R_N(1-\alpha_F^2)} \equiv \gamma_C \tag{3.6}$$

By substituting the assumed transport parameter values for CoFe, NiFe and the IR, it can readily be shown that (3.5) and (3.6) yield the same numerical values for α_{FC} and γ_C as those shown in Fig. 3.2(a) and Fig. 3.3(a).

3.1.1.2.2 Finite Spin-Relaxation Length In the previous section, we have assumed no spin relaxation via spin-flip of electron during its transport within the trilayer. In this section, the effect of spin-flip inside the layers (not at the interface). will be incorporated using the theoretical framework presented in Sec. 3.1.1.1. We will show that in the limit of bulk spin-diffusion length tending to infinity, i.e. $\lambda_{N,F} \to \infty$, the calculated results will approach those obtained via the TC model.

The MR dependence on FM resistance is investigated and the results are plotted in Fig. 3.2(b). In the range of small to moderate FM resistance, i.e. $R_F \approx 0$ to $100R_{NiFe}$, the MR dependence on R_F is similar to that of the TC model of Fig. 3.2(a), i.e. MR increases (decreases) with increasing FM resistivity when $\alpha_F > \alpha_{FC}$ ($\alpha_F < \alpha_{FC}$). These trends have been explained by the competition effect between the FM layers and IRs. However, for very high FM areal resistance, we observe that MR decreases to zero

with increasing FM resistance. Unlike the previous MR behaviour, this trend occurs for all values of α_F, even when α_F exceeds the critical value of α_{FC}. When $\alpha_F > \alpha_{FC}$, the MR initially increases with R_F, before saturating at a plateau value and then decreasing gradually towards zero with a further increase in R_F. For the case of $\alpha_F < \alpha_{FC}$, MR initially decreases with R_F, before saturating at a plateau and then resuming its descent towards zero. Figure 3.3(b) shows the MR dependence on IR in the presence of spin relaxation. The results are similar to the MR dependence on R_F as shown in Fig. 3.2(b). In this case, MR reduces monotonically to zero when $\gamma < \gamma_c$, while for $\gamma > \gamma_c$, MR initially increases to a plateau before decreasing towards zero for very high R_I. The suppression of MR towards zero at very high FM or IR is clearly due to the presence of spin relaxation, since it disappears in the limit of $\lambda \rightarrow \infty$. The physics of MR suppression at high resistance has been studied and explained in Sec. 2.3.3.

3.1.1.3 Conclusion

We investigated the spin transport across a CPP trilayer, with IR considered at the two FM-NM interfaces. We first considered the case of spin transport in the limit of infinite spin relaxation length. We found that in the presence of the IRs, the expected trend of increasing MR with increasing FM or IR resistances occurs only when the intrinsic spin polarization α_F of the FM material or the spin-selectivity γ of the IRs exceeds some critical value of α_{FC} and γ_C, respectively. Below these critical values, the MR shows a declining trend with increasing FM or IR, which may be attributed to the competition between the FM and the IR resistances in determining the overall MR of the trilayer. The critical thresholds α_{FC} and γ_C are analytically derived and their dependence on transport parameters such as resistivity of the NM spacer is determined, thus providing

useful knowledge for optimizing the MR of PSV devices. In the presence of spin-flip (i.e. finite spin relaxation length) in the layers, MR is suppressed at extremely high IR/FM resistances, irrespective of the intrinsic spin polarization of the IR/FM layers. Thus, in inserting IRs into a magnetic trilayer in order to improve its MR, one has to consider the complex interplay between the physics of charge transport (resistivity of the FM and NM layers) and spin transport (intrinsic polarization of the FM layers and spin relaxation effect), which gives rise to the two aforementioned trends in MR. The analysis of these effects could provide a useful guide to practical methods of optimizing the MR of CPP devices, in which IR cannot be ignored.

3.1.2 Model II: Finite Interfacial Spin-flip

In the previous section, we studied the effect of electron momentum scattering at the interface, while assuming that there is no spin scattering at the interfaces. In this section we develop a model to include the effect of spin scattering at the interface. Here we model the interfaces as ultra-thin layers, in the limit of the layer thickness approaching zero. Our analysis is focused on three important interfacial parameters, i.e. interfacial resistance (R_I), interfacial spin selectivity (γ), and interfacial spin-flip parameter (ζ). We compare the relative contribution of bulk scattering and interfacial scattering to the overall MR. We notice that when γ is greater (smaller) than a critical value, γ_C, then MR increases with increasing (decreasing) R_I. Larger FM resistivity results in lower MR if $\gamma > \gamma_C$. Finally we show the effect of ζ on MR. At high(low) ζ, which signifies spin coherence at the interface is conserved(depolarized), MR increases (decreases). We also analyze the competition between γ and ζ in contributing towards overall MR. Our results show that the negative effect on MR due to interfacial spin flip can be minimized by using higher R_I.

3.1.2.1 Theory

In the previous model (Model I), we have neglected the effect of spin-flip at the interfaces. In this model, we include the interfacial spin-flip effect. This is done by modeling the interfaces as ultra-thin layers, in the limit of the interfacial layer thickness δ_I approaching zero, i.e. $\delta_I \rightarrow 0$. This is illustrated in Fig. 3.4. "Interfacial resistiviy (ρ_I)" and "interfacial spin diffusion length (λ_I)", is related to the interfacial resistance (R_I)

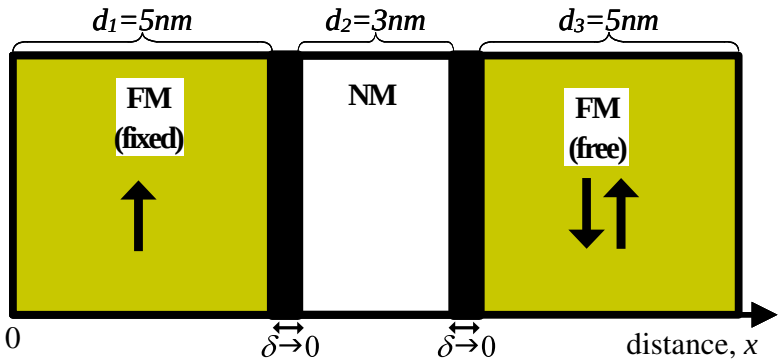

Figure 3.4: Schematic illustration of the trilayer device in which interfaces are modeled as ultra-thin layers

and interfacial spin flip parameter (ζ), respectively, by the following relations:

$$\rho_I \rightarrow R_I/\delta_I, \tag{3.7a}$$

$$\lambda_I \rightarrow \zeta\delta_I, \tag{3.7b}$$

As far as interfacial parameters are concerned, the MR expression obtained in this manner is only dependent on R_I, ζ, and γ but independent of other boundary parameters such as δ_I. Therefore this expression is suitable for ultra-thin interfaces, i.e. $\delta_I \rightarrow 0$. In the numerical calculations, the bulk SDL is assumed to be much longer than the thickness of each layer. This enables us to study the effect of spin flip in the interfacial regions exclusively.

3.1.2.2 Result and Discussion

3.1.2.2.1 Interfacial Momentum Scattering We study the variation of MR as a function of γ for different values of R_I. The calculated results are shown in Fig. 3.5 and Fig. 3.6. The dotted lines in both figures refer to the MR curve when CoFe is replaced by a hypothetical FM material with resistivity five times greater than CoFe i.e.

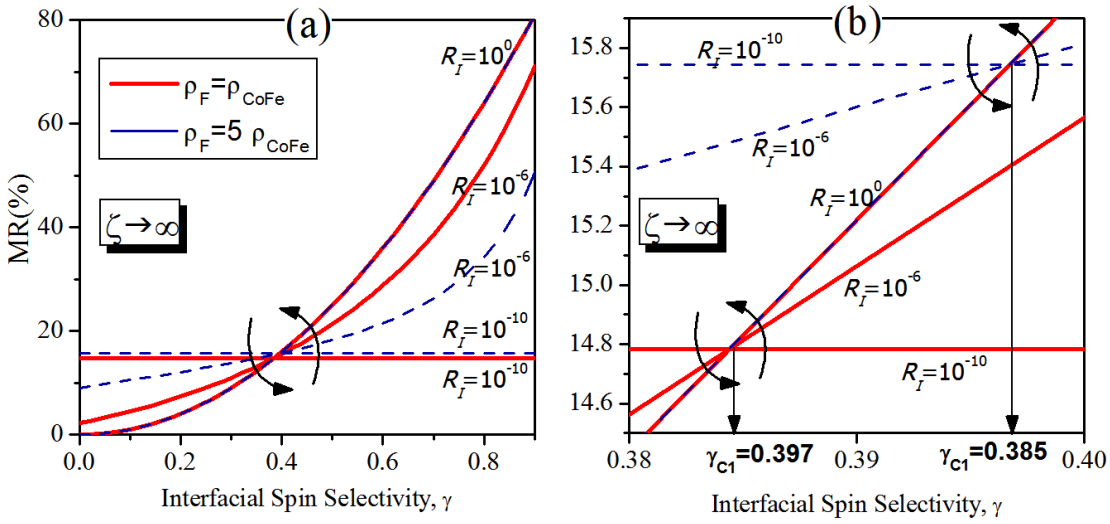

Figure 3.5: (a) MR as a function of γ, for different R_I values, (b) Magnified region of Fig. 2(a) in the range of γ =0.38 to 0.4. The critical values γ_C corresponding to the different ρ_{F} are indicated. The curved arrows denote increasing R_I, which is expressed in units of Ωm^2. ζ is set to ∞, i.e. no spin-flipping at the interfaces for both (a) and (b).

$\rho_{\mathrm{FM}} = 5\rho_{\mathrm{CoFe}}$, but having the same intrinsic conductance polarization.

Figure 3.5 shows the effect of γ on the MR of the device, neglecting the effect of interfacial spin flip, i.e. $\zeta \rightarrow \infty$. As shown in the figure, the MR variation with increasing γ is dependent on the value of R_I. As indicated by the arrow in Fig. 3.5, if γ is greater (smaller) than a critical value γ_C, the MR ratio increases (decreases) with increasing R_I. The derivation of γ_C is already shown in Sec. 3.1.1 [refer (3.6)].

It is worth noting that γ_C is equivalent to the effective bulk polarization of the trilayer with perfect interface, i.e. no interfacial spin flip and no interfacial scattering. The MR behaviour in Fig. 3.5 can be explained as follows: when R_I increases, interfacial scattering becomes more dominant compared to bulk scattering. Therefore, if the interfacial spin-selectivity is larger than the effective bulk spin polarization, i.e. γ_C, then the overall MR will increase with increasing R_I. Likewise, a larger FM resistivity can actually result in a lower MR if $\gamma > \gamma_C$, which is contrary to general expectation. This

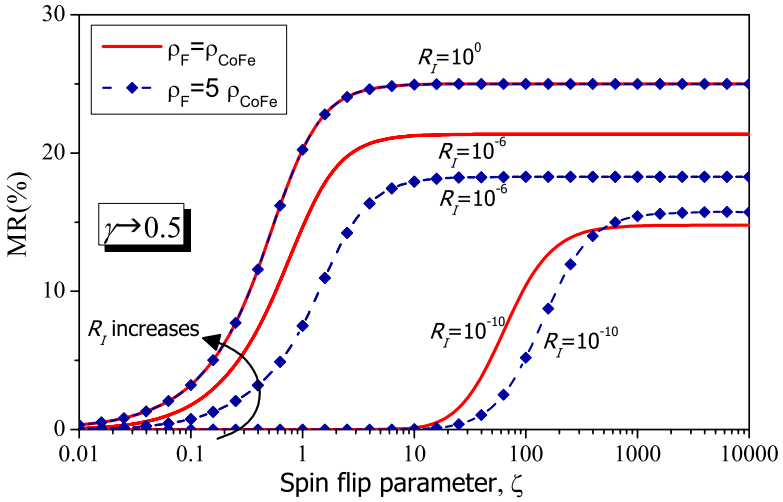

Figure 3.6: MR versus spin-flip parameter ζ for different R_I values, expressed in Ωm^2. Curved arrows denote increasing R_I. Spin selectivity γ is fixed at 0.5.

can be seen by comparing the solid and dotted lines of Fig. 3.5.

It can also be noted that for the smaller value of R_I considered, i.e. $R_I = 10^{-10}$ $\Omega\mathrm{m}^2$, the MR ratio is a constant value, independent of the value of γ. On the other hand when R_I is very large i.e. $R_I = 1$ $\Omega\mathrm{m}^2$, then MR ratio is independent of the resistivity of the FM layer. This is because for very small (large) value of R_I, the bulk (interfacial) spin scattering is the predominant mechanism, such that the other contribution has practically no effect on MR. Note that although the values of R_I considered are relatively higher than the typical interfacial resistances of clean FM-NM interfaces ($\sim 10^{-15}\Omega\mathrm{m}^2$),[101] they are comparable to experimental values after incorporation of thin nano-oxide layers.[103] Note that these effects of γ is consistent with the previous model in Sec. 3.1.1.

3.1.2.2.2 Interfacial Spin-Flip Scattering Figure 3.6 shows the effect of interfacial spin-flip on MR. A higher ζ (i.e. smaller degree of spin flip) will cause an increase in the MR ratio for any given value of R_I. Therefore an interface which preserves spin coherence (with a high ζ value) enables a high MR value to be attained. Conversely, a

strongly depolarizing interface will suppress MR, so that MR$\rightarrow 0$ as $\zeta \rightarrow 0$.

When $\zeta \rightarrow \infty$, MR achieves the maximum value corresponding to the MR ratio when there is no interfacial spin flip, i.e. MR($\zeta \rightarrow \infty$). A careful examination of Fig. 3.6 shows when R_I is high (relative to FM resistivity), MR not only achieves higher value but also saturates at a smaller ζ value. These results suggest that the negative effect of interfacial spin flip on MR can be reduced by engineering an interface with higher R_I. However, it should be noted that the increase in R_I may result in an overall reduction of MR if $\gamma < \gamma_C$, as we have shown in Fig. 3.6. It is therefore important for experimentalists to estimate the value of γ_C, and prepare the sample such that, $\gamma > \gamma_C$. A crude approach to ensure that $\gamma > \gamma_C$, is to choose γ which is much greater than α_F. When this is achieved, effort should be focused on increasing R_I so that MR increases sharply with the reduction of spin flip as well as achieves higher saturation value. Reduction of interfacial spin flip can be achieved by using clean interfaces especially with respect to the absence of magnetic impurities or spin orbit coupling effects.

3.1.2.3 Conclusion

We develop a model to include the effect of spin scattering at the interface. Our results show that proper engineering of the interface is an important factor to enhance the MR of a CPP SV structure. If the interface has high spin-selectivity, i.e. $\gamma > \gamma_C$, then higher R_I is preferred. Otherwise, R_I should be minimized. Interfaces with high ζ always results in high MR. The effect of ζ on MR reduction can be minimized by increasing R_I. However, it should be noted that the increase in R_I may result in an overall reduction of MR if $\gamma < \gamma_C$. Therefore, interfaces with higher γ, i.e. $\gamma > \gamma_C$ and R_I is preferable for enhancing MR as well as reducing the spin flip effect.

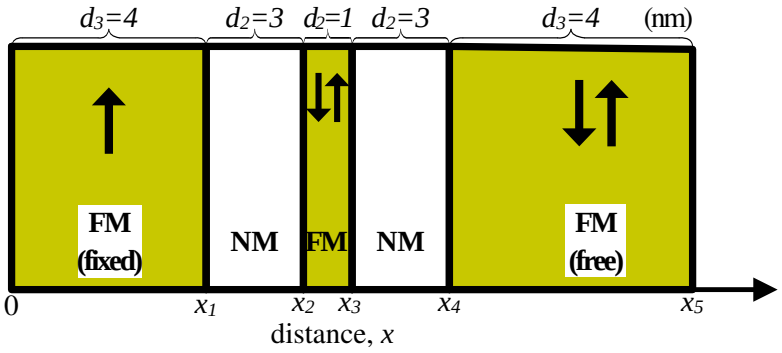

Figure 3.7: Schematic illustration of the penta-layer SV, consisting of a basic spin-valve trilayers with FM2 insertions within the NM layer. The four interfaces of the device are denoted by x_1, x_2, x_3, and x_4.

3.2 Effect of Layer Insertion

In the previous sections we have incorporated the effect of IR in the PSV device. Here, we propose an alternative method to improve he MR by inserting a thin FM layer into the NM spacer of a basic SV tri-layer (FM1-NM-FM1), thus creating a pentalayer SV structure (FM1-NM-FM2-NM-FM1). We investigate the effect of increasing the resistivity (ρ_{F2}) of the FM2 on overall MR. For finite ρ_{F2}, the MR profile is dependent on the intrinsic conductance polarization (α_{F2}) of FM2. It is found that MR can be doubled by inserting a FM layer with high α_{F2}, such as the half-metallic Cr_2O. We have numerically calculated MR_{max} and the corresponding ρ_{F20} values for different α_{F2} values. Finally we also study the effect of spin relaxation on the MR of the CPP SV.

3.2.1 Theory

We apply modified SDD model as described in Sec. 2.2 by increasing the number of layers into five [Fig. 3.7] and applying the boundary conditions at each interfaces. We study the effect of varying resistivity and conductance polarization of the FM2 layer on the overall MR of the CPP SV. First we set the FM2 to be a free layer and performed our calculation in the limit of SDL of all the layers approaching infinity, i.e. $\lambda \to \infty$. We analyzed the MR behavior of this device, and then utilize these behaviors to enhance overall device MR. Following this, we studied the MR when a finite spin relaxation, λ is taken into consideration.

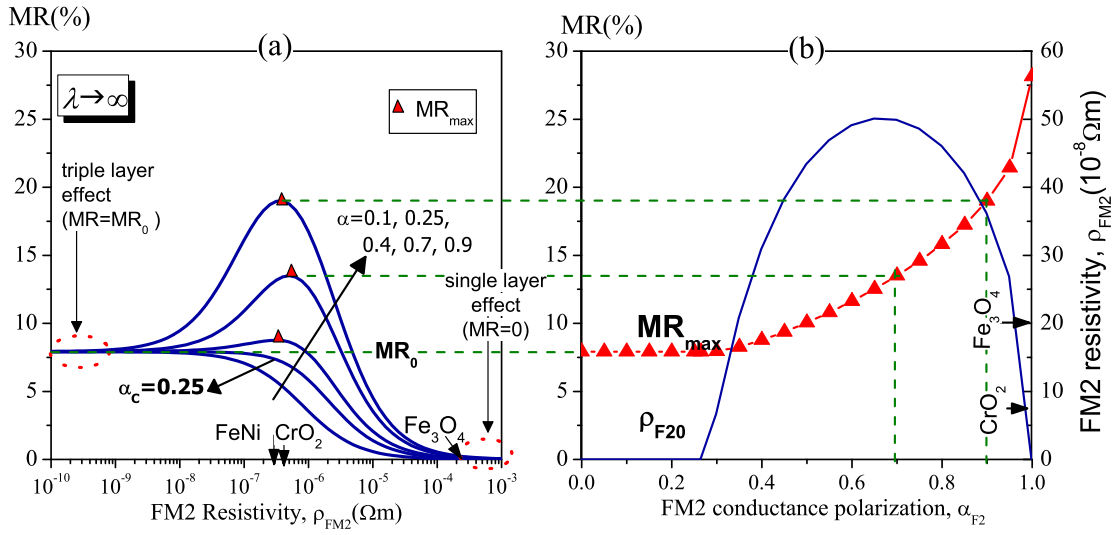

Figure 3.8: (a) Plot of MR as a function of resistivity of FM2 layer, for the penta-layer device. Infinite SDL is assumed. MR shows a monotonic decrease with increasing ρ_{F2} when $\alpha_{F2} < \alpha_{2C}$. When $\alpha_{F2} > \alpha_{2C}$ MR increases to a maximum before decreasing to zero. The maximum is marked with a "red" triangle. (b) Maximum MR, MR_{max} and corresponding value of FM2 resistivity, ρ_{F20} for varying α_{F2} is shown.

3.2.2 Results and Discussion

In the limit of $\lambda \rightarrow \infty$, spin flip does not occur. Under this condition, the analytical expression of MR for the device in Fig. 3.7(a) is given by

$$MR = \frac{400\alpha_{F1}R_{F1}(\alpha_{F1}R_{F1}(1-\alpha_{F2}^2)+\alpha_{F2}R_{F2}(1-\alpha_{F1}^2))}{(2R_{F1}(1-\alpha_{F2})+(1-\alpha_{F1}^2)(R_{F2}+2R_N(1-\alpha_{F2}))(2R_{F1}(\alpha_{F2}+1)-(1-\alpha_{F1}^2)(R_{F2}+2R_N(1+\alpha_{F2}))} \tag{3.8}$$

The MR curves with increasing ρ_{F2} for different values of α_{F2} are plotted in Fig. 3.8(a). For highly resistive FM2 layer, i.e. $\rho_{F2} \rightarrow \infty$, MR approaches zero regardless of the value of α_{F2}. This is because at high ρ_{F2}, the resistance of FM2 layer becomes dominant compared to the resistance of both FM1 layers. Since FM2 is a single free magnetic layer, the SV structure effectively becomes a single soft magnetic layer, where $R^{AP} = R^{P}$. Therefore there is no MR effect observed in this structure. To the other extreme, when ρ_{F2} is zero, MR converges to a finite value, MR_0. This finite MR_0 is a constant independent of the conductance polarization of FM2 layer. Substituting

$\rho_{F2} = 0$ (or $R_{F2} = 0$) into (3.8), we obtained the expression the basic SV tri-layer without FM2 insertion, i.e.

$$\text{MR}_0 = \frac{100\alpha_{F1}^2 R_{F1}^2}{(R_{F1} + R_N - \alpha_{F1}^2 R_N)^2} \tag{3.9}$$

This is because at zero resistivity of FM2, the contribution of FM2 to overall MR becomes insignificant. FM1 layers become dominant and thus the pentalayer SV reduces to a basic trilayer SV with no additional layers.

For a finite ρ_{F2}, MR profile is more complicated and is strongly dependent on the values of α_{F2}, due to resistance competitive effect. As shown in Fig. 3.8(a), there is a critical value for the conductance polarization of FM2 layer i.e. α_{2C}, below which MR show a monotonic decreasing trend with increasing FM2 resistivity. When $\alpha_{F2} > \alpha_{2C}$, then MR increases to a maximum of MR_{max}, before decreasing to zero at large FM2 resistivity. These results show that insertion of new FM layer can only be effective in enhancing MR if conductance polarization of that layer is greater than α_{2C}.

The analytical expression of α_{2C} can be derived from (3.8) and (3.9), by equating MR to MR_0. Two values of FM2 resistivities, $\rho_{F2a} = 0$ and ρ_{F2b} are obtained. MR is higher than MR_0 within the range of $\rho_{F2a} < \rho_{F2} < \rho_{F2b}$. Therefore to ensure MR>MR_0, ρ_{F2b} has to be greater than $\rho_{F2a} = 0$. Thus the critical value, α_{2C} is derived by setting $\rho_{F2b} = \rho_{F2a} = 0$.

$$\alpha_{2C} = \frac{\alpha_{F1}\rho_{F1}d_{F1}}{\rho_{F1}d_{F1} + \rho_N d_N(1 - \alpha_{F1}^2)} \tag{3.10}$$

By solving $d\text{MR}(\rho_{F2})/d\rho_{F2} = 0$, MR_{max} and the corresponding FM2 resistivity, ρ_{F20} can be obtained. We have verified that the expression of α_{2C} is the same as the effective conductance polarization of the structure without FM2 insertion. This shows that an increasing trend of MR can only be obtained when the conductance polarization of

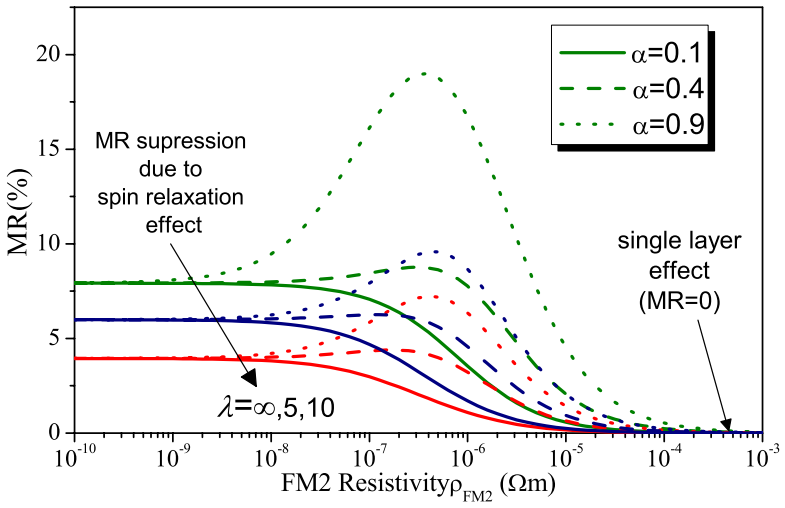

Figure 3.9: Plot of MR as a function of resistivity of FM2 layer for the SV penta-layer device with finite λ_F. MR value is lower when the when λ_F is shorter.

the FM2 layer exceeds the effective polarization of all other layers combined. Otherwise increasing ρ_{F2} results in decreasing MR. It is important to note that α_{2C} is smaller than α_{F1}. To relate our theoretical prediction to practical need, we numerically calculated MR$_{max}$ and ρ_{F20} values, for different α_{F2} values. As shown in the Fig. 3.8(b), the range of ρ_{F20} and α_{F2} can be readily achieved in halfmetallic FM materials, e.g. CrO_2 and Heusler alloys. It is found that MR can be doubled by inserting a FM layer with high intrinsic conductance polarization, such as half-metallic Cr_2O.

Next based on the same SDD approach, we will consider the effects of spin relaxation. Fig. 3.9 shows the MR behavior of the SV penta-layer with finite λ_F. The simulation results shows similar trend as in Fig. 3.8(a), with suppression of MR at higher λ_F. This is because finite λ_F causes spin relaxation which reduces the polarization throughout the SV.

In the above computation we assumed FM2 has a free magnetization (**M**) that rotates together with the **M** of the free layer, which implies it has a low coercivity.

This greatly limit the scope of material selection for FM2. Alternatively for the SV pentalayer, FM2 can be a fixed layer. Repeating the above derivation by fixing the **M** for the FM2, we obtained the same MR results as in Fig. 3.8 and Fig. 3.9. These results show that the magnetic switching property of the FM2 material would not affect the MR behavior of our proposed SV penta-layer.

3.2.2.1 Conclusion

We have inserted FM2 layer in between the NM layer. We investigated the effect of ρ_{F2} on the overall MR. We found that MR can be doubled by inserting a FM layer with high conductance polarization, such as half-metallic Cr_2O. We have also shown that spin relaxation reduces the MR of the SV device.

3.3 Summary

In this chapter, we studied the optimization of MR by including additional resistive components–1) IR and 2) additional layers–into a basic PSV device. In both cases, we found that there is a competition between all the individual resistive components in dominating the current polarization and thus the spin asymmetry of the device. Our results show that this resistance competitive effect plays a very crucial role in MR optimization. Due to this effect, an increase in the resistance of a layer/interface results in higher MR only if the conduction spin polarization of the layer/interface is greater than a critical value. We also analyzed the interplay between resistance competitive effect and spin-relaxation for further optimization of the MR.

Chapter 4

Current Confinement Effects

In the previous chapter, we studied the effects of additional resistive components in a SV device. In this chapter, we continue to study the effect of patterning/engineering the layers in a SV device. Patterning of layers not only effects the resistance due to areal change, but also gives rise to the current confinement effect which further causes other phenomenon such as current crowding and spreading resistance. Therefore, to optimize MR all these effects have to be considered. We have also shown that by carefully utilizing these effects, device performance can be highly enhanced.

4.1 Effect of Spreading Resistance on Magnetoresistance

We derive the MR that takes into consideration the effect of spreading resistance (SR) due to the patterned layer in a SV structure. Our analysis is based on the i) SDD model and ii) finite-element Poisson (FEP) solver. The SDD model does not take into consideration the effect of SR due to patterning, whereas FEP includes the effect of SR. This enables us to compare and analyze the contribution of both patterning and SR to the MR of the device. In a FM-NM-FM structure, the NM layer was patterned into i) single and ii) multiple cylindrical structures. We find that the spacer patterning and the resulting SR causes a significant increase (by 50%) of MR at low area ratio of the patterned layer. Yet, MR of the patterned structure is lower compared to the MR of the original structure. To overcome this problem, we pattern a FM layer inserted within the NM spacer [refer Sec. 3.2]. This results in significantly higher MR.

Recently, in order to further enhance its MR ratio, and so maintain the high rate of growth in the areal storage density of magnetic recording media towards 1 Tbit/in^2 and beyond, intense research are done to modify the basic CPP GMR SV structure. One of the proposed modifications is a confinement of the current path either across the spacer layer[?,89] or the FM layer.[92] In this section, we analyze the effect of current confine-

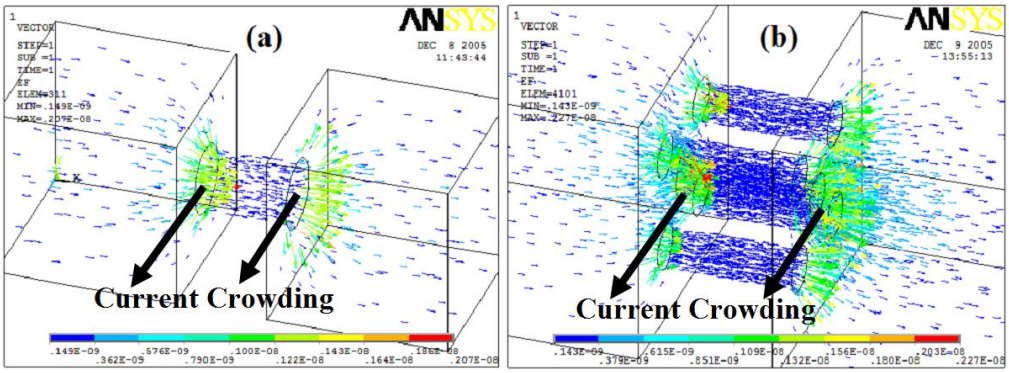

Figure 4.1: Schematic diagram of the spreading electric field lines between the NM spacer layer in the middle and the adjacent FM layers of a spin valve structure. The spacer has been patterned into (a) single patterning, and (b) multiple (5) patterning

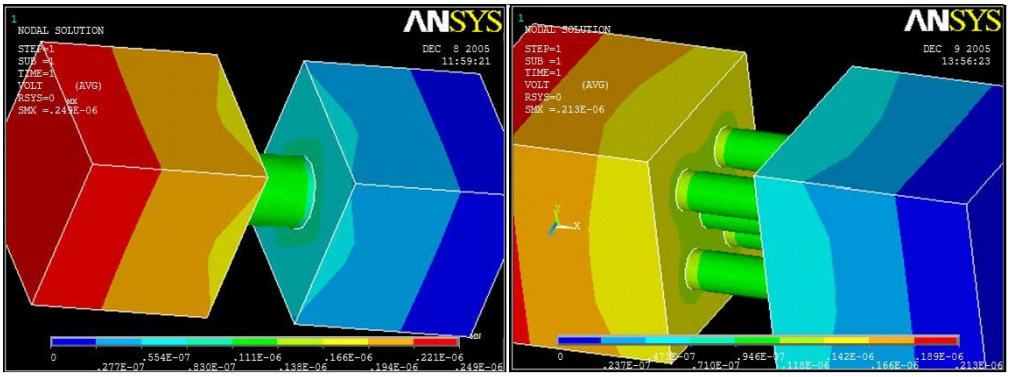

Figure 4.2: Simulated potential drop across the (a)single patterned device, and (b) multiple (5) patterning.

ment achieved by patterning selected layers of the CPP SV into cylindrical nanopillar structures. Our analysis includes not only the resistive increase in the patterned layer, but also the significant spreading resistance (SR) in the adjacent layers, due to the non-parallel current flow into and out of the nanopillars. In order to determine the optimal patterning, the effect of SR on the overall MR ratio is investigated for different nanopillar geometry, such as cross-sectional area and packing density.

4.1.1 Theory

The analytical SDD model [Sec. 2.2] calculates the spin transport through the trilayer in the presence of spin relaxation. It accounts for the resistance increase due to the patterning and the resulting current confinement in the spacer layer. However, the SDD model does not take into consideration the effect of SR arising from the patterning. SR effect is studied by using the finite-element-poison (FEP) method.

Next we describe the FEP method. The equilibrium current flux and potential distribution across the device is calculated numerically by solving the Poisson equation, using the ANSYS finite element (FE) solver. In the FE calculation, the device structure is first discretized by tetrahedral meshing, and a unit current load is specified on every FE node on the left boundary of the device, while the voltage is set to be zero at the right boundary of the device [refer Appendix B].

We apply this FEP method to calculate the effect of SR arising from the patterning of the spacer layer. The MR of the device is obtained by substituting these conductivity values into the TC model which gives a good approximation since λ of each of the three layers is much longer than the layer thicknesses. From the FE model, we obtain the potential drop corresponding to the different possible spin-dependent channels of the TC model as shown in Fig. 4.3. Hence we obtain the overall potential drop across the trilayer for the parallel, $V^P = V_{\uparrow\uparrow} + V_{\downarrow\downarrow}$) and anti-parallel, $V^{AP} = V_{\downarrow\uparrow} + V_{\uparrow\downarrow}$ configurations. The MR ratio is given by $MR = (V^{AP} - V^P)/V^{AP}$.

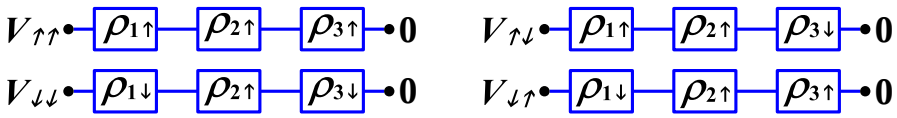

Figure 4.3: Four different possible spin-dependent current branches in two current model relative to the trilayer structure.

4.1.2 Results and Discussion

4.1.2.1 Current Confinement

We first investigate the effect of the patterning of the spacer layer on SR in the FM layers. Fig. 4.1 shows the calculated electric field lines and spreading flux between the constrained current paths in the middle spacer layer and the adjacent FM layers. The spacer layer is patterned either as a (a) single or (b) multiple nanopillar structures, which are cylindrical in shape. As shown in Fig. 4.1, the patterning of the spacer layer leads to current crowding near the interfaces, which in turn gives rise to SR in the FM layers, and thus increases the overall resistance of the FM layers. Fig. 4.2 shows the potential variation across the device. Due to SR effect we can observe potential invariance in y- and z- direction near the interfaces.

4.1.2.2 Magnetoresistance and Spreading Resistance

4.1.2.2.1 Trilayer Structure Next we analyze the MR ratio of the trilayer for three different cases: (i) based on the SDD model, (ii) based on the FEP model but with the spacer layer patterned into a multi-cylindrical (5-cylinders) structure, and (iii) based on the FEP model, with the spacer layer patterned into a single cylindrical pillar structure. In all three cases, the total cross-sectional (conducting) area of the spacer is reduced to the same ratio $A_R(< 1)$ compared to the non-patterned FM layers. Note that the

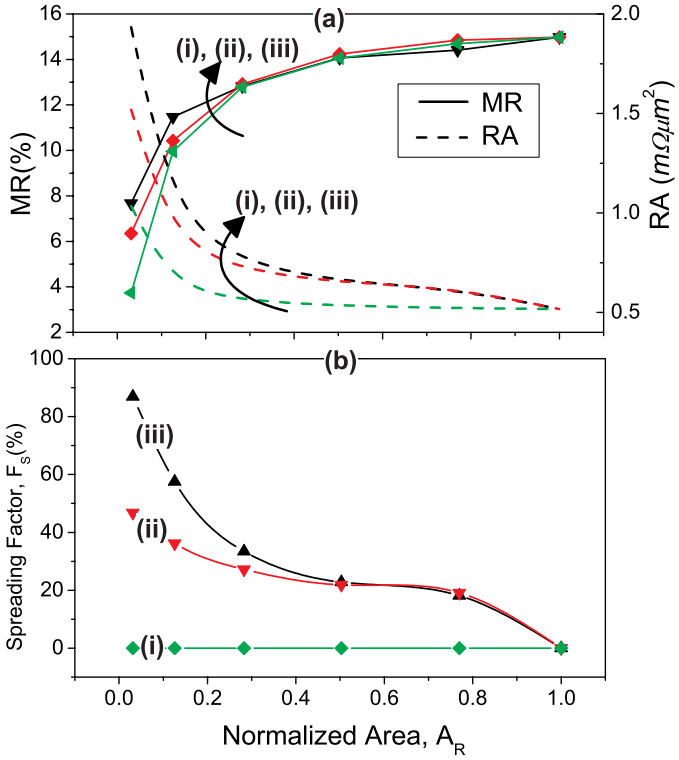

Figure 4.4: (a) Solid (dashed) line shows MR (areal resistance, RA) as a function of the normalized patterned area, A_R for different types of patterning. (b) Spreading factor, F_S as a function of the A_R. Curve (i),(ii), and (iii) represents results from, SDD model, FEP model with multiple (5) patterning, and FEP model with single patterning, respectively.

SDD model includes only the effect of current confinement within the spacer, but not SR. Thus MR is only dependent on the patterned area A_R but not on the number of cylindrical nanopillars. However, the results from the FEP model are dependent on the number of nanopillars, since the effect of the spreading field lines and hence SR will differ for single and multiple patterning. Fig. 4.4(a) shows the MR dependence on the normalized spacer area A_R for cases (i), (ii), and (iii). The difference in MR of curves (i), (ii), and (iii) of Fig. 4.4(a) is solely due to the effect of SR. We define a parameter, spreading factor (F_s) to characterize the SR:

$$F_s = \frac{V^{FE} - V^{SDD}}{V^{SDD}}, \tag{4.1}$$

where V^{FE} and V^{SDD} are the potential difference across the patterned trilayer structure obtained via the FEP and SDD models, respectively. The dependence of F_s on A_R in the AP configuration is plotted in Fig. 4.4(b). As the size of the patterned spacer area (A_R) reduces, the effect of SR increases, and this is reflected by a monotonic increase of F_s with decreasing A_R. The value of F_s is also dependent on the number of patterned nanopillars. This is especially so for low A_R values, where F_s is almost twice as large for a single nanopillar patterning compared to multiple nanopillar patterning. The difference is mainly due to the suppression of SR due to the interference of the spreading field lines out of adjacent nanopillars. As A_R approaches one, i.e. in the limit of no patterning of the spacer layer, F_s expectedly decreases to zero, indicating the absence of spreading factor.

From Fig. 4.4(a), we found that the effect of the SR in the FM layers is to cause a significant increase in the MR ratio (by more than 50%) for a highly constricted spacer (i.e. low A_R). This is especially so when the spacer is patterned as a single cylindrical nanopillar, for which the MR is about double compared to the MR obtained from the SDD model, which neglects SR. Yet, patterning of the spacer still results in an overall lowering of the MR ratio, i.e. the MR ratio of the patterned structures $(A_R < 1)$ is lower compared to that of the original trilayer without any patterning $(A_R = 1)$. This is because patterning causes two opposing effects on the MR ratio: i) lowering of MR due to the increase of NM layer resistance as a result of its lower cross sectional area, and ii) increase of MR due to higher FM layer resistance as a result of SR. Thus, as shown in Fig. 4.4(a), the first effect dominates over the second, leading to an overall decreasing trend in MR when A_R is reduced.

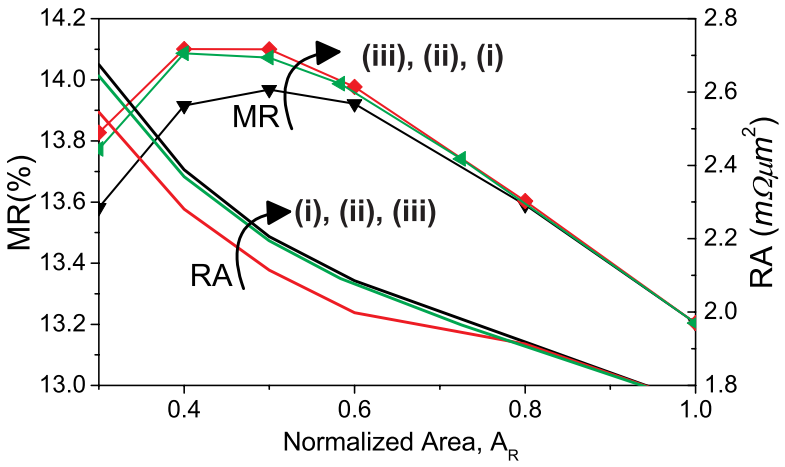

Figure 4.5: Plots show MR and areal resistance, RA as a function of the normalized patterned area, A_R for a penta-layer spin valve device with patterned FM insertions. Curve (i),(ii), and (iii) represents results from, SDD model, FEP model with multiple (5) patterning, and FEP model with single patterning, respectively.

This runs counter to our objective of enhancing MR via patterning and current confinement. Thus, we propose further modifications to the trilayer SV structure, to ensure that patterning will have a net positive effect on the MR ratio.

4.1.2.2.2 Pentalayer Structure The first modification is that a thin FM layer is inserted within the spacer layer to create a pentalayer structure [similar to the structure discussed in Sec. 3.2]. The MR behavior of this structure has been studied in Sec. 3.2. The second modification is that it is the FM layer instead of the NM spacer which is patterned. The thickness of the inserted FM layer is $0.5nm$. Fig. 4.5 shows the calculated MR ratio of the proposed pentalayer as a function of the normalized cross sectional area A_R of the patterned FM insertion. As before, we consider the three different cases of SDD model with no SR, and SR with single and multiple patterning. Unlike Fig. 4.4(a), a decrease in A_R due to patterning enhances the MR ratio up to a maximum point at A_R of approximately 0.4 to 0.45 for the structure under consideration. Further patterning causes the MR ratio to decrease. Thus, an optimal amount of patterning has

to be performed to the FM insertion in order to achieve the maximum MR. Unlike the earlier patterned trilayer structure, patterning the FM insertion into multiple cylindrical nanopillars yields a higher MR compared to the single nanopillar patterning. To account for this, we note that patterning of the FM insertion i) increases its resistance due to lower cross sectional area, and ii) increases the resistance of the adjacent NM layers due to SR. The first effect enhances the MR while the second effect reduces MR, which is a reversal of the effects of patterning the NM spacer in the trilayer structure. Since patterning into multiple nanopillars reduces the second effect, it therefore results in a higher MR ratio compared to single nanopillar patterning. Thus, in order to utilize the patterning and current-confining method for MR optimization in a practical SV device, one can for instance apply the partial oxidation technique, which has previously been applied to a Cu-Al alloy[89] to achieve a multiple nanopillar patterning.

4.1.3 Conclusion

We derived the MR that takes into consideration the effect of SR due to the patterned layer in a SV structure. In a FM-NM-FM structure, the NM layer was patterned into i) single and ii) multiple cylindrical structures. We found that the spacer patterning and the resulting SR causes a significant increase of MR at low area ratio of the patterned layer. Yet, MR of patterned structure is lower compared to the MR of original structure. This was overcome by patterning a FM layer inserted within the NM spacer.

4.2 High Spin injection with nanopillar FM nanostruture

In this section, we report the prediction of a high SI ratio γ into a SC contact, by using a FM, small-sized, cylindrically patterned nanopillar as the spin injector. The increase in spin scattering within the FM nanopillar injects spin current into the SC, effectually mitigates the blockage of SI due to conductance mismatch. To minimize the SR which arises due to areal discontinuity at FM-SC interface, a thin low resistance metal is inserted at the interface such that SR is contained within it. With the insertion, we obtained γ of as high as 40%, compared to just 3% without insertion, and an even lower value of 0.5% without the nanopillar patterning.

Semiconductor (SC) based spintronics[4] allows the exploitation of spin as well as the charge property of the electron for operation in devices. The inherently long SDL[27,28] and the manipulation of spin coherence by electrical and magnetic[104,105] means in semiconductors have led to potential spin-based memory, optoelectronic, and spin field-effect transistor applications.[15] A crucial element for the functioning of such devices is the injection of spin polarized current into semiconductor.[20,33,34] Previous efforts which utilize a FM metal layer for direct SI into the semiconductor layer have not proved effective, mainly as a result of the large conductance mismatch[35–39] between FM and SC. Although SI through a tunnel barrier can potentially achieve a high spin injection ratio,[36] the device operation is susceptible to defect and impurity states in the barrier.[106]

In this section, we propose the use of a FM nanopillar as a spin injector into a semiconductor layer with a much larger cross sectional area. Additionally, a nonmagnetic metal insertion layer is required between the FM nanopillar and the semiconductor layer, to act as a buffer layer to contain the high, spin-independent spreading resistance (SR) that arises from the areal mismatch between the nanopillar and the device. Such SR effect tends to reduce SI if it is not contained within a low-resistivity metal layer. Here we show that high SI into SC can possibly be achieved with the use

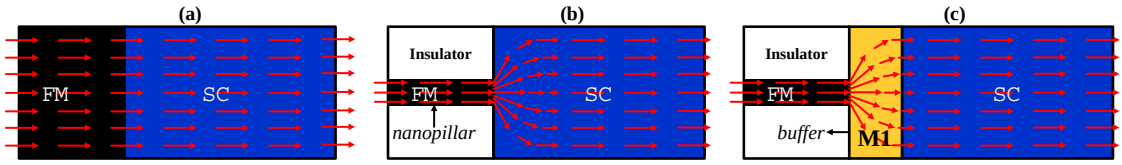

Figure 4.6: Schematic illustration of the hybrid spin injection device. M1, SC, and FM denote low resistive metallic conductor, semiconductor, and ferromagnetic metal, respectively. Arrow shows current direction.

of a FM pillar injector and a Cu insertion layer. Our main discussion will be focused on the basic working principles of our proposed spin injection device. We have neglected interfacial effects like trap and defect states, as these do not have direct relevance to the working principles of the device.

4.2.1 Theory

The structure under investigation is a hybrid FM-SC bilayer with a low resistance non-magnetic metal (M1) inserted in between the FM and the SC layers, as illustrated in Fig. 4.6. In our analysis we use NiFe, Cu, and GaAs for the FM, M1, and SC material, respectively. The following material and transport parameters are assumed throughout the paper: spin diffusion length, $\lambda_{NiFe} = 10nm$, $\lambda_{Cu} = 140nm$, $\lambda_{GaAs} \rightarrow 10,000nm$; intrinsic conductance polarization, $\alpha_{NiFe} = 0.4$, $\alpha_{Cu} = \alpha_{GaAs} = 0.0$; and resistivity, $\rho_{NiFe} = 1.16 \times 10^{-7}\Omega m$, $\rho_{Cu} = 1.68 \times 10^{-8}\Omega m$, $\rho_{GaAs} = 10^{-3}\Omega m$. For comparison, we first investigate the SI ratio into the SC layer in a FM-SC bilayer structure without patterning into the pillar structure, and without the M1 buffer insertion [Fig. 4.6(a)]. We define the SI efficiency into SC layer as:

$$\gamma = \left.\frac{I_{\uparrow}(x) - I_{\downarrow}(x)}{I_{\uparrow}(x) + I_{\downarrow}(x)}\right|_{x = x_{sc}} = (2\beta(x) - 1)|_{x=x_{sc}} \tag{4.2}$$

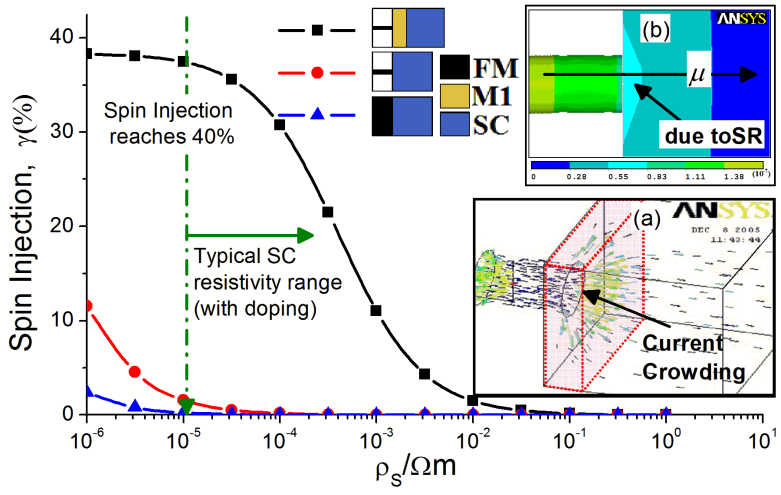

Figure 4.7: Spin injection vs. ρ_S for different structures. [triangular] basic FM-SC structure, [circle] FM injector is patterned into pillars of smaller cross sectional area, $A_{FM} = 4\pi nm^2$, [square] an additional M1 layer inserted in between patterned FM and SC. Arrow indicates the typical resistivity range for GaAs which can be varied by varying doping concentration. Inset (a) shows the effect of current crowding. Inset (b) shows the non-uniform potential distribution due to spreading resistance

By applying the SDD equations [refer Sec. 2.2], the SI efficiency can be derived as follows:

$$\gamma = \frac{\alpha_F \lambda_F \rho_F}{\lambda_F \rho_F + d_S \rho_S \left(1 - \alpha_F^2\right) \coth\left(d_F/\lambda_F\right)}. \tag{4.3}$$

4.2.2 Results and Discussion

The calculated results are denoted by "triangular" curve in Fig. 4.7. For the typical resistivity range of the SC layer (as indicated by the arrow in Fig. 4.7), SI efficiency is extremely low, i.e. $\gamma < 0.001\%$. The low γ value is expected, due to the presence of the highly resistive nonmagnetic SC layer compared to the FM metal injector, thus reducing the overall spin asymmetry of the device. As shown in the graph, a possible method to improve the SI is by reducing the resistance of the SC material, and hence the conductivity mismatch between the SC and FM metal. This can be achieved by

increasing the doping concentration of the SC material. However, doping concentration in excess of $10^{20}cm^{-3}$ is technically difficult to achieve over a large layer depth.

Here we have proposed another method to increase the SI, i.e. by patterning the FM layer into nanopillars with a small cross sectional area, as shown in Fig. 4.6(b). After the FM injector is patterned into cylindrical pillars of cross-sectional radius r of $2nm$, the resulting SI efficiency γ is plotted as "circle" curve in Fig. 4.7. Patterning the injector into a pillar structure leads to an enhancement of γ. For instance, at a SC resistivity of 10^{-5}, γ is increased from 0.5% to 3% due to patterning. However, despite the improvement in γ, its value is still low ($\sim 1-3\%$) at the typical SC resistivity.

To explain the relatively low γ value, we note that the large areal discontinuity between the FM injector and the SC layer results in a current crowding [Sec. 4.1.2.1] effect in the latter. The arrows in Fig. 4.6 show the schematic illustration of current direction, hence the current crowding effect in the device due to patterned injector. In Fig. 4.6(b), the current crowding effect is concentrated at the vicinity of the interface but rapidly diminishes as we move further into the SC layer away from interfaces [refer the insets of Fig. 4.7].

The result of the simulation is shown in the inset (a) of Fig. 4.7, where the current direction becomes parallel as current propagates away from the interface. Current crowding is responsible for depressing the γ value, as it results in a large SR in the SC layer, and thus increases the effective resistance of the SC layer. Inset (b) of Fig. 4.7 shows that the electrochemical potential distribution becomes non-uniform in the SC layer. Non-uniform potential distribution is due to the abrupt interfaces and gives rise to SR.

The magnitude of the SR can be estimated by considering the analytical SR value of $\rho/4r$[107] which occurs in the limit of $(A_{SC}/A_{FM}) \rightarrow \infty$, where A_{SC} and A_{FM} are the cross-sectional area of the SC and FM layers, respectively. Based on this approximation the effective resistance of the SC layer is approximately given by:

$$\rho_{SC,eff} = \rho_{sc}\left(\frac{\sqrt{\pi}}{4\sqrt{A_{FM}}}\frac{A_{SC}}{d_{SC}} + 1\right) \tag{4.4}$$

Thus, the patterning of the FM injector results in two competing effects, i.e. 1) an increase in the resistance of the FM injector and 2) the formation of SR in the SC layer and hence the increase in the effective resistance of the SC as shown in (4.4). The first (second) effect increases (reduces) the overall spin asymmetry of the device which in turn increases (decreases) the γ. From Fig. 4.7 we can see that the first effect is more dominant and thus improvement in SI is achieved due to patterning of FM injector. However such SI value is still too low for practical device application. Therefore, to increase the SI value we need to reduce the effect of SR.

Since SR is directly proportional to the material resistivity, the effect of SR can be minimized by containing the SR in a low resistivity metal (M1) rather than the high resistivity SC layer. To this end, we insert a thin Cu layer in between FM and SC, as illustrated in Fig. 4.6(c). The current flux that is injected from the FM injector initially radiates in all direction in the M1 layer, but eventually becomes collinear in the perpendicular to plane direction prior to entering the SC layer. Therefore, there would not be any current crowding and hence no SR effect in the SC layer. As shown by "square" curve in Fig. 4.7, this insertion results in a very significant increase in γ, i.e. γ increases from 3% to 37% with the insertion of M1 layer at a typical $\rho_{SC} = 10^{-5}\Omega m$.

The M1 layer plays a crucial role in raising SI, thus we need to study the effect

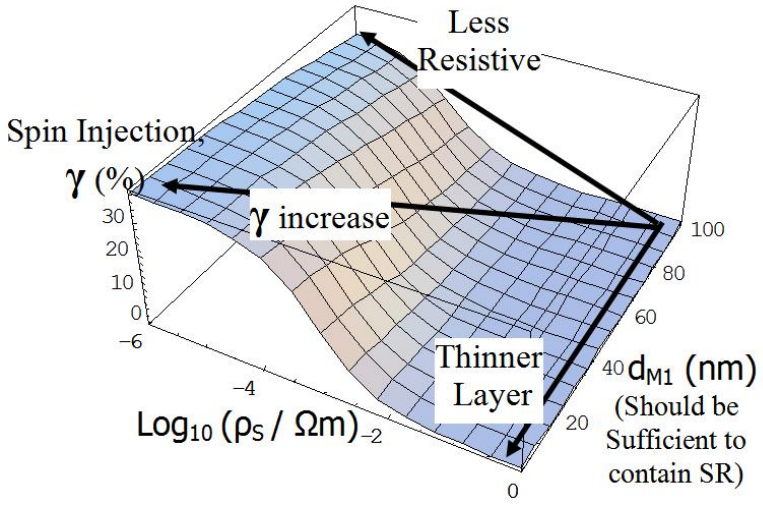

Figure 4.8: 3-D plot showing the variation of spin injection with ρ_S and d_{M1}. Spin injection decreases with the increase of both ρ_S and d_{M1}.

of the thickness of the inserted M1 buffer layer (d_{M1}) and the SC resistivity (ρ_{SC}) on SI. The calculated results are shown by the 3-D plot in Fig. 4.8. In the calculations, we have assumed that the SR is completely contained within the M1 layer. Figure 4.8 shows that SI decreases monotonically with both increasing SC resistivity and M1 layer thickness. The M1 buffer layer is nonmagnetic, just like the SC layer, and thus increasing its thickness d_{M1} will decrease the overall spin asymmetry of the device. Additionally, an increase in d_{M1} will also result in greater spin-flip probability within the M1 layer, which further reduces the overall SI. However, as mentioned earlier M1 plays the crucial role of containing the SR. Therefore, in real device the M1 layer should be of the minimum thickness required to contain the SR. In numerical finite-element calculation of the current flux, we found that a small thickness of $5 - 6nm$ is sufficient to accommodate the current crowding effect.

4.2.3 Conclusion

We have presented a simple but effective method to enhance SI into SC from a FM injector, by patterning the injector into a nanopillar, such that its cross-sectional area is much smaller than that of the SC layer ($A_{FM} \ll A_{SC}$). However the areal discontinuity at the interface gives rise to the SR effect which reduces the γ. To minimize SR effect, we insert a thin low resistive metallic (M1) layer at the interface and thus contained the SR within the low resistive M1 layer. By containing SR in M1 layer we manage to obtain very high γ, i.e. $\gamma = 40\%$ compared to only $\gamma = 3\%$ (without the M1 layer) and $\gamma = 0.5\%$ (without patterning of the FM injector). Our results could provide useful guidance to experimentalists intending to use FM material to polarize as well as inject spin current into semiconductors.

4.3 Summary

We have studied the current confinement effect which rises due to the effect of patterning the layers in a SV device. The current confinement effect further causes other phenomenon such as current crowding and spreading resistance. To optimize MR all these effects was considered. We showed that device performance can be highly enhanced by carefully utilizing these effects.

Chapter 5

Oscillatory MR due to Resonant Tunneling Effect

In the previous chapters, we studied the electron and spin transport properties in a purely diffusive regime. In this chapter, we study electron and spin transport across a 2DEG structure, in which ballistic transport is assumed, given the long MFP within the 2DEG. We find that the transport properties of the device, such as the transmission probability, the SI efficiency and the MR ratio, all exhibit oscillatory behavior when electron energy is varied. The basis of these oscillations is the resonant transport across the 2DEG. By utilizing this resonant transport property, we further propose a SC-based gate controlled MR device that could perform the function of a metallic SV, but with the advantage that its MR can be optimized (post-fabrication) and its stability enhanced by controlling a gate bias voltage.

5.1 Resonant Tunneling in Diffusive-Ballistic-Diffusive Regime

Here, we investigate the spin polarized resonant transport in a hybrid HEMT structure, with source and drain electrodes made of FM material, while the channel consists two-dimensional electron gas (2DEG). The electron transport in the FM layer is modeled using SDD model, while across the 2DEG layer, ballistic transport is assumed, given the long MFP within the 2DEG. By solving the two transport models self-consistently, we find that the transport properties of the device, such as the transmission probability, the SI efficiency and the MR ratio, all exhibit oscillatory behavior when the 2DEG layer width or the 2DEG Fermi energy is varied. The basis of these oscillations is the resonant transport across the 2DEG, which is reminiscent of the spin-polarized resonant tunneling (SPRT), observed recently in magnetic tunnel junctions (MTJ). The hybrid device has distinct advantages over the metal-based MTJ structures in the practical utilization of the SPRT effect. This is because the ballistic charge conduction through the 2DEG enables easy tunability of the MR ratio and SI efficiency, by varying the doping density and gate bias, while avoiding the exponential suppression of MR with barrier thickness, which occurs in MTJ devices. Numerically, the hybrid HEMT device is predicted to be capable of achieving a maximum MR and SI ratios approaching 20% and 40%, respectively, at the crest of

their respective oscillations.

Quantum effects resulting in resonant oscillatory MR behavior, have been experimentally observed and theoretically predicted in double-barrier structures based on DMS,[21] and hybrid FM-SC materials,[108] respectively. Such oscillatory behavior may potentially be utilized to manipulate and optimize the MR and SI ratios in SC-based devices, as well as provide additional functionalities, such as spin-dependent resonant tunneling devices in the coherent tunneling regime. The oscillatory MR behavior was first observed in MTJ, where a thin NM metal layer is inserted in between the insulating tunnel barrier and one of the FM metal electrodes.[109] The effect is ascribed to the spin-polarized resonant tunneling (SPRT) effect involving quantum well states, and exhibits TMR oscillations as the NM layer thickness is varied. Theoretically, the SPRT effect was first modeled by a single band models,[110,111] which demonstrate a nonzero TMR in the presence of the NM insertion, thus contradicting the classical theory of tunneling. Subsequently, Mathon *et al.*[112] provided a more refined theoretical model of SPRT by incorporating more realistic band structures. Experimentally, various studies have been conducted to investigate the SPRT effect in metal MTJ structures.[109,113–118] However, the SPRT oscillatory effect is found to be small[109,118,119] or virtually unobservable.[113–117] Although, the use of double-MTJ structures[120] may enhance some of the quantum size effects, there are key obstacles to its realization in metal-based MTJs: i) the TMR ratio decays rapidly (exponentially) with increasing thickness of the NM insertion, ii) the oscillatory frequency is very high with modulation period of only $\sim$ 1-2 nm, given the large Fermi wave-vector in the NM metal insertion, and iii) there appears to be only one (rather inconvenient) method to modulate the TMR modulation, i.e. by

changing the NM thickness.[109,113,118–120]

Thus, to overcome these difficulties, we propose the utilization of a hybrid high-electron-mobilty-transistor (HEMT) structure, with source and drain made of FM material, as shown in Fig. 5.1 to achieve the SPRT effect. The channel of the HEMT structure consists of a highly-doped n^{++} AlGaAs-GaAs 2DEG layer. Electron transport in the FM layer is modeled using SDD model, in which the electron undergoes momentum and spin scattering while traveling inside the FM layers. In the 2DEG layer, electron transmission is modeled as ballistic transmission, where the electron is transmitted across the layer without any scattering. Spin polarization and momentum are preserved during this transmission. Ballistic transmission in the 2DEG layer is achieved by ensuring that the thickness of the layer is smaller than the MFP of electron in the layer.

The ballistic transport yields an oscillatory behavior, reminiscent of the SPRT effect. Utilizing the SPRT effect may provide a potential method of optimizing the MR ratio of the device, e.g. by setting the lateral dimension of the device to coincide with one of the resonant MR peaks. The key advantages of this oscillatory MR effect in SC as opposed to metallic MTJ devices are: i) ballistic transport can occur in the free conduction instead of tunneling regimes, so that the transmission probability is not exponential suppressed with the barrier width, ii) the low Fermi wavevector in the 2DEG allows for larger modulation period, and hence obviates the need for precise optimization of the 2DEG thickness, and iii) the use of the versatile 2DEG material allows for other avenues of MR modulation. For instance, the MR ratio can be tuned or controlled externally either by application of a gate bias or by changing the 2DEG doping level, thus providing an added functionality compared to the usual metallic SV

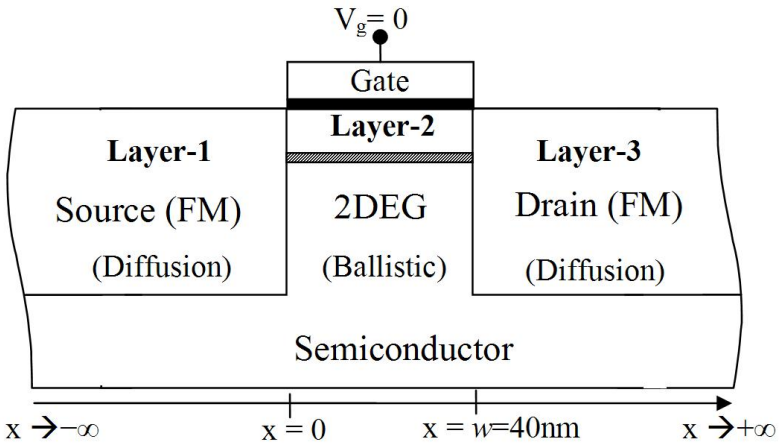

Figure 5.1: Schematic illustration of the hybrid SC-FM device based on the HEMT. It consists of a 2DEG conducting channel between FM source and drain electrodes.

devices.

5.1.1 Theory

5.1.1.1 Spin drift-diffusive transport in the FM electrodes

We first present the spin transport model within the FM source and drain electrodes. w refers to the width of the 2DEG layer. The subscript and superscript $\uparrow$ ($\downarrow$) represent the majority (minority) spin component, while the subscript S (F) refers to the semiconductor 2DEG (FM) layer. As described in Sec. 2.2, the general solution for the spin accumulation $\Delta\mu_i(x)$ in the FM electrodes (i.e. layers i=1 and 3) can be expressed as:

$$\Delta\mu_i(x) = P_i \exp\left(\frac{x}{\lambda_i}\right) + Q_i \exp\left(-\frac{x}{\lambda_i}\right). \tag{5.1}$$

The coefficients P_1, Q_1, P_3 and Q_3 can be solved by applying the following boundary conditions at the FM-2DEG interfaces ($x = 0$ and $x = w$):

$$ej_{\uparrow}(0)\rho_{1\uparrow} - ej_{\downarrow}(0)\rho_{1\downarrow} = -\left.\frac{\partial \Delta\mu_1(x)}{\partial x}\right|_{x=0}, \tag{5.2}$$

$$ej_{\uparrow}(w)\rho_{3\uparrow} - ej_{\downarrow}(w)\rho_{3\downarrow} = -\left.\frac{\partial \Delta\mu_3(x)}{\partial x}\right|_{x=w}, \tag{5.3}$$

and at the terminals of the semi-infinite FM contacts ($x = \pm\infty$), where spin accumulation vanishes:

$$\Delta\mu_1(x \to -\infty) = \Delta\mu_3(x \to +\infty) = 0. \tag{5.4}$$

Additionally, the continuity of the electrochemical potentials dictates that

$$\Delta\mu_3(w) - \Delta\mu_1(0) = -(\Delta U_2^{\uparrow} - \Delta U_2^{\downarrow}), \tag{5.5}$$

where $\Delta U_2^{\downarrow,\uparrow}$ refers to the electrochemical potential drop of spin-up (down) current across the 2DEG layer. Equation (5.2) and (5.3) are derived from (2.2) by considering the spin current at the interfaces. Due to ballistic transmission, we assume no spin flip scattering in the 2DEG layer, and thus $j_{\uparrow,\downarrow}(0) = j_{\uparrow,\downarrow}(w)$. Solving the above boundary conditions i.e. (5.2) to (5.5) simultaneously, yields the following expressions for P_1, Q_1, P_3 and Q_3, and the current polarization at the two FM-2DEG interfaces $\beta(0)$ and $\beta(w)$:

$$P_1 = \frac{\Delta U_2^{\uparrow} - \Delta U_2^{\downarrow}}{2}, \tag{5.6a}$$

$$Q_3 = \frac{e^{w/\lambda_F}(\Delta U_2^{\downarrow} - \Delta U_2^{\uparrow})}{2}, \tag{5.6b}$$

$$Q_1 = P_3 = 0, \tag{5.6c}$$

$$\beta(0) = \beta(w) = \frac{(1+\alpha_F)}{2}\left(\frac{(1-\alpha_F)(\Delta U_2^{\uparrow} - \Delta U_2^{\downarrow})}{4ej_F\lambda_F\rho_F} + 1\right). \tag{5.6d}$$

Note that $\beta(0) = \beta(w)$ due to the absence of spin flip in the 2DEG layer. From the above results, the spatial variation of spin accumulation $\Delta\mu$ in (5.1) can be determined. Subsequently, the spatial profile of $\beta(x)$ across FM layers are obtained by considering (5.2) and (5.3) for an arbitrary position x. The solution $\beta_i(x)$ is then substituted into (2.2), and after integration, the spatial dependence of the electrochemical potential for both spins, $\mu_{\uparrow,\downarrow}(x)$, is obtained within each FM layer.

To analyze the MR, we let layer-1 be the pinned FM layer with a fixed magnetization, while layer-3 is the free FM layer, whose magnetization orientation can be switched by an external field. The solutions in (5.6a) to (5.6d) apply for the case of P configuration. We repeat the above analysis for the AP configuration, where the magnetization of layer-3 is in opposite direction to that of layer-1. The spin-dependent resistivity of the FM layers in the P and AP configurations $\rho_{F\uparrow,\downarrow}^{P(AP)}$, are related to one another as follows: $\rho_{F\uparrow,\downarrow} = \rho_{F\uparrow,\downarrow}^{P} = \rho_{F\downarrow,\uparrow}^{AP}$.

In computing the MR ratio, we consider the electrochemical potential drop between $x = -\lambda_F$ and $x = w + \lambda_F$, i.e. a thickness of λ_F in each of the FM contacts. This is because λ_F is the lengthscale across which the spin dependent resistance changes will occur.[35] The explicit expression for MR is given by:

$$\begin{aligned} \mathrm{MR} &\equiv \frac{R^{AP} - R^{P}}{R^{P}} = \frac{\Delta\mu_0^{AP} - \Delta\mu_0^{P}}{\Delta\mu_0^{P}} \\ &= \frac{\alpha_F \left((1-\alpha_F^2)(\Delta U_2^{\uparrow} - \Delta U_2^{\downarrow}) + 4ej_F\alpha_F\lambda_F\rho_F \right)}{(1-\alpha_F^2)\left((1+\alpha_F)\Delta U_2^{\uparrow} + (1-\alpha_F)\Delta U_2^{\downarrow} + 4ej_F\lambda_F\rho_F \right)}, \end{aligned} \tag{5.7}$$

where $R^{AP}(R^P)$ refers to the overall resistance in the AP(P) configuration, and $\Delta\mu_0^{P,AP} = \mu_0^{P,AP}(x = -\lambda_F) - \Delta\mu_0^{P,AP}(x = w + \lambda_F)$. μ_0 is the linear (ohmic) component of elec-

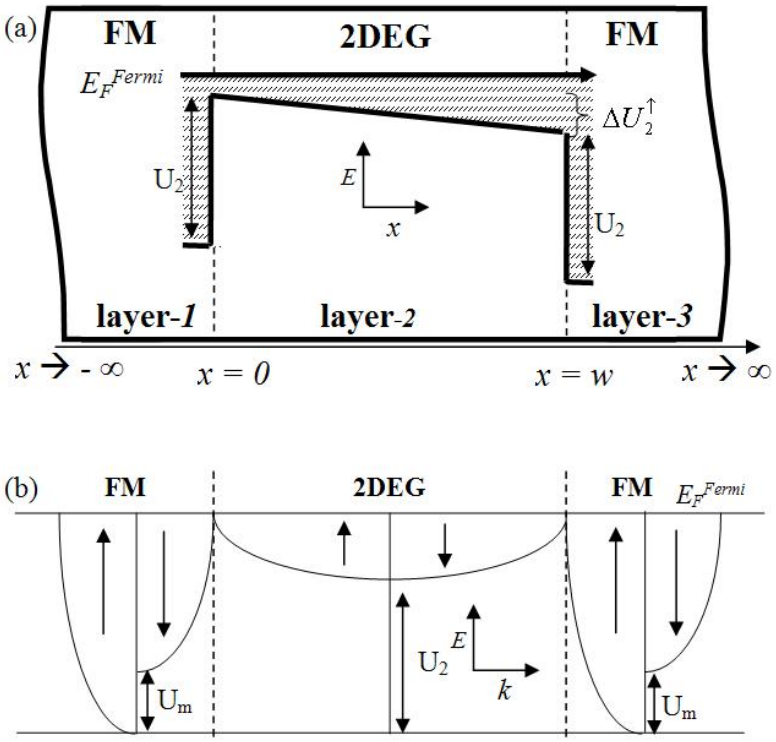

Figure 5.2: (a) Schematic diagram showing the energy barrier in the hybrid HEMT structure. Only spin-up component is shown. (b) Schematic band-diagram of the structure showing the origin of U_2 and U_m.

trochemical potential, which is the equilibrium spin-independent component of either $\mu_{\uparrow}(x)$ or $\mu_{\downarrow}(x)$.

5.1.1.2 Ballistic transport model within the 2DEG

Next we model the electron transport in the layer-2, i.e. the 2DEG layer. We assume the electron's MFP to be longer than the 2DEG layer width, so that electron conduction can be described by a ballistic spin-dependent transmission model. We consider the parabolic-band effective-mass approximation, so that (by referring to Fig. 5.2), the

Schrödinger equation for layers-1 to 3 can respectively, be written as:

$$-\frac{\hbar^2}{2m_F}\frac{\partial^2\Psi_1^{\uparrow,\downarrow}(x)}{\partial(x)}+U_1^{\uparrow,\downarrow}\Psi_1^{\uparrow,\downarrow}(x) = (E_{FM}+\delta\mu_1^{\uparrow,\downarrow})\Psi_1^{\uparrow,\downarrow}(x), \quad (5.8a)$$

$$-\frac{\hbar^2}{2m_S}\frac{\partial^2\Psi_2^{\uparrow,\downarrow}(x)}{\partial(x)}+\left(U_2-\frac{\Delta U_2^{\uparrow,\downarrow}}{w}x\right)\Psi_2^{\uparrow,\downarrow}(x) = (E_{FM}+\Delta U_2^{\uparrow,\downarrow})\Psi_2^{\uparrow,\downarrow}(x) \quad (5.8b)$$

$$-\frac{\hbar^2}{2m_F}\frac{\partial^2\Psi_3^{\uparrow,\downarrow}(x)}{\partial(x)}+U_3^{\uparrow,\downarrow}\Psi_3^{\uparrow,\downarrow}(x) = (E_{FM}+\delta\mu_3^{\uparrow,\downarrow})\Psi_3^{\uparrow,\downarrow}(x). \quad (5.8c)$$

For the FM layers, the above equations [i.e. (5.8a) and (5.8c)] are applicable only at the interfacial regions ($x = 0$ and $x = w$), where ballistic transmission occurs between the FM and 2DEG layers. Away from the interfaces i.e. within the bulk FM, the electron transport is more accurately described by the SDD equations of (2.2) and (5.1). The potential energy in the FM regions in the P configuration are given by $U_1^{\uparrow} = 0, U_1^{\downarrow} = U_m, U_3^{\uparrow} = -\Delta U_2^{\uparrow}$, and $U_3^{\downarrow} = U_m - \Delta U_2^{\downarrow}$, where U_m is the energy difference between majority and minority spins due to the molecular magnetic field within the FM material (see Sec. 1.2.1.1), and $\Delta U_2^{\uparrow(\downarrow)}$ is the potential energy drop across the 2DEG for spin up (down) electrons, respectively.

In the AP configuration, we assume the magnetization of layer-3 is reversed. Thus, in layer 3, the potential energy terms for the two spin orientations are interchanged, i.e. $U_3^{AP\uparrow} = U_m - \Delta U_2^{\uparrow}$, and $U_3^{AP\downarrow} = -\Delta U_2^{\downarrow}$. As shown in Fig. 5.2(b), U_2 in (5.8b) is the shift in potential energy so as to align the 2DEG Fermi level with the Fermi level of the FM layers. Thus, $U_2 = E_{FM} - E_{FS}$, where E_{FM} and E_{FS} are the equilibrium Fermi levels of FM and 2DEG layers, respectively. m_F and m_S are the effective electron mass in the FM and 2DEG layers, respectively, while $\delta\mu_{1(3)}^{\uparrow,\downarrow}$ represents the non-linear part of the electrochemical potential at the left (right) FM-2DEG interface. This non-linear

component is the deviation of the electrochemical potentials of the two spin channels $\mu^{\uparrow,\downarrow}$ from the ohmic electrostatic potential, due to spin accumulation at the interface. The relationship between $\delta\mu_{1,3}^{\uparrow,\downarrow}$ and the spin accumulation $\Delta\mu_{1,3}$ of (5.1) is given by $\delta\mu_1^{\uparrow} + \delta\mu_1^{\downarrow} = \Delta\mu_1(0)$, and $\delta\mu_3^{\uparrow} + \delta\mu_3^{\downarrow} = \Delta\mu_3(w)$, respectively. Solving the above Schrödinger equation yields the following electron wave function in each region:

$$\Psi_1^{\uparrow,\downarrow}(x) = C_1^{\uparrow,\downarrow}\exp(ik_1^{\uparrow,\downarrow}) + D_1^{\uparrow,\downarrow}\exp(-ik_1^{\uparrow,\downarrow}), \tag{5.9a}$$

$$\Psi_2^{\uparrow,\downarrow}(x) = C_2^{\uparrow,\downarrow}\mathrm{Ai}\left[\frac{(E_{FM}-U_2)w + \Delta U_2^{\uparrow,\downarrow}x}{\Delta U_2^{\uparrow,\downarrow}}\left(\frac{2m_S\Delta U_2^{\uparrow,\downarrow}}{w\hbar^2}\right)^{1/3}\right] + D_2^{\uparrow,\downarrow}\mathrm{Bi}\left[\frac{(E_{FM}-U_2)w + \Delta U_2^{\uparrow,\downarrow}x}{\Delta U_2^{\uparrow,\downarrow}}\left(\frac{2m_S\Delta U_2^{\uparrow,\downarrow}}{w\hbar^2}\right)^{1/3}\right], \tag{5.9b}$$

$$\Psi_3^{\uparrow,\downarrow}(x) = C_3^{\uparrow,\downarrow}\exp(ik_3^{\uparrow,\downarrow}) + D_3^{\uparrow,\downarrow}\exp(-ik_3^{\uparrow,\downarrow}), \tag{5.9c}$$

where the wave vector at the FM layers interfaces are

$$k_{1,3}^{\uparrow,\downarrow} = \frac{\sqrt{2}\sqrt{m_F E_F^{Fermi} + m_F\delta\mu_{1,3}^{\uparrow,\downarrow} - m_F U_{1,3}^{\uparrow,\downarrow}}}{\hbar}. \tag{5.10}$$

The coefficients $C_{1,2,3}^{\uparrow,\downarrow}$ and $D_{1,2,3}^{\uparrow,\downarrow}$ are determined by applying flux and wave function matching at the FM-2DEG interfaces:

$$\psi_1^{\uparrow,\downarrow}(0) = \psi_2^{\uparrow,\downarrow}(0), \tag{5.11a}$$

$$\psi_2^{\uparrow,\downarrow}(w) = \psi_3^{\uparrow,\downarrow}(w), \tag{5.11b}$$

$$\frac{1}{m_F}\frac{d\psi_1^{\uparrow,\downarrow}(x)}{dx}\bigg|_{x=0} = \frac{1}{m_S}\frac{d\psi_2^{\uparrow,\downarrow}(x)}{dx}\bigg|_{x=0}, \tag{5.11c}$$

$$\frac{1}{m_S}\frac{d\psi_{2i}^{\uparrow,\downarrow}(x)}{dx}\bigg|_{x=w} = \frac{1}{m_F}\frac{d\psi_3^{\uparrow,\downarrow}(x)}{dx}\bigg|_{x=w}, \tag{5.11d}$$

$$D_3^{\uparrow,\downarrow} = 0, \tag{5.11e}$$

Equation (5.11a) and (5.11b) are obtained by applying wave function matching at the interfaces. Equation (5.11c) and (5.11d) are obtained by applying flux matching at the interfaces. Since there is no reflected wave at the final FM layer (layer-3), (5.11e) denotes zero amplitude of the reflected wave there. By solving these equations we obtained the ratio, $\left(C_3^{\uparrow,\downarrow}/C_1^{\uparrow,\downarrow}\right)$. The ballistic transmission probability across the 2DEG layer is then given by:

$$T^{\uparrow,\downarrow} = \frac{k_3^{\uparrow,\downarrow}}{k_1^{\uparrow,\downarrow}} \left| \frac{C_3^{\uparrow,\downarrow}}{C_1^{\uparrow,\downarrow}} \right|. \tag{5.12}$$

Assuming perfect ballistic transmission, the (areal) resistance across the 2DEG layer can be obtained from Landauer's formula as:

$$R_2^{\uparrow,\downarrow} = \frac{2\pi\hbar}{e^2 T^{\uparrow,\downarrow}} n_m \times A_F \tag{5.13}$$

where n_m is the number of transverse modes and A_F is the cross-sectional area(in y-z plane) of the device. To simplify our analysis, we restrict our analysis to one transverse conductance mode only ($n_m = 1$). This may be achieved in practice e.g. by constricting the FM-SC interface to a narrow channel, so that it acts as a mode filter, which allows only one transverse mode to pass through. We have also neglected any effects arising from Schottky barriers at the FM-2DEG interfaces. This is because, the presence of a Schottky barrier, although it may possibly increase the overall MR ratio,[121] is an undesirable feature in practical GaAs/AlGaAs 2DEG heterostructures, for which ohmic contacts are much preferred.[122]

5.1.1.3 Ballistic-Diffusive Self-consistent approach

To complete the transport calculations, we have to unify the ballistic and diffusive transport within the 2DEG and FM layers, respectively. This is performed based on our

earlier scheme,[123] in which the link between the two transport regimes is established by considering the spin accumulation component of the potential $\delta\mu^{\uparrow,\downarrow}$. The values of $\delta\mu^{\uparrow,\downarrow}$ at the FM-SC interfaces are determined by the SDD relations [i.e. (2.2) and (5.1). These, in turn, contribute to the kinetic energy of electrons undergoing ballistic transmission at the FM-2DEG interfaces, and hence affects $T^{\uparrow,\downarrow}$ across the 2DEG [from (5.10) and (5.12)]. Additionally, we assume the conduction electrons are sufficiently equilibrated after undergoing ballistic transmission across the 2DEG, so that the total potential drop experienced by the electrons across the 2DEG is given by $\Delta U_2^{\uparrow,\downarrow} = j_F^{\uparrow,\downarrow} R_2^{\uparrow,\downarrow}$. For simplicity, we have the neglected the detailed analysis of thermobalistic current in the equilibration process.[124] Conversely, as can be seen from (5.9a) to (5.9b), and (5.13), $T^{\uparrow,\downarrow}$ itself is also a function of $\Delta U_2^{\uparrow,\downarrow}$. Based on the above interdependence, a self-consistency loop can be established between the ballistic and SDD transport calculations to solve for $T^{\uparrow,\downarrow}$ and hence $R_2^{\uparrow,\downarrow}$ across the 2DEG. The self-consistency calculations are performed until the values of $R_2^{\uparrow,\downarrow}$ have converged to better than 0.1% accuracy.

In the numerical calculations, we assume the hybrid structure to be composed of the following materials: FM electrodes of nominally half-metallic $\mathrm{Fe_3O_4}$, and the SC conducting layer consisting of a highly-doped n^{++} AlGaAs-GaAs 2DEG. Unless otherwise specified, the following parameter values are assumed: $E_{FS} = 3.5\mathrm{meV}, \alpha_F = 0.7, j_F = 1\mathrm{A/m}^2, \rho_F = 10^{-4}\Omega\mathrm{m}, A_F = 50$ nm $\times 50$ nm (in *y*-*z* plane), $\lambda_F = 100$ nm, $m_F = 1m_e = 9.1 \times 10^{-31}$ kg, $m_S = 0.067m_e, E_{FM} = 11.10$ eV, $U_m = 0.25$ eV and $w = 40$ nm.

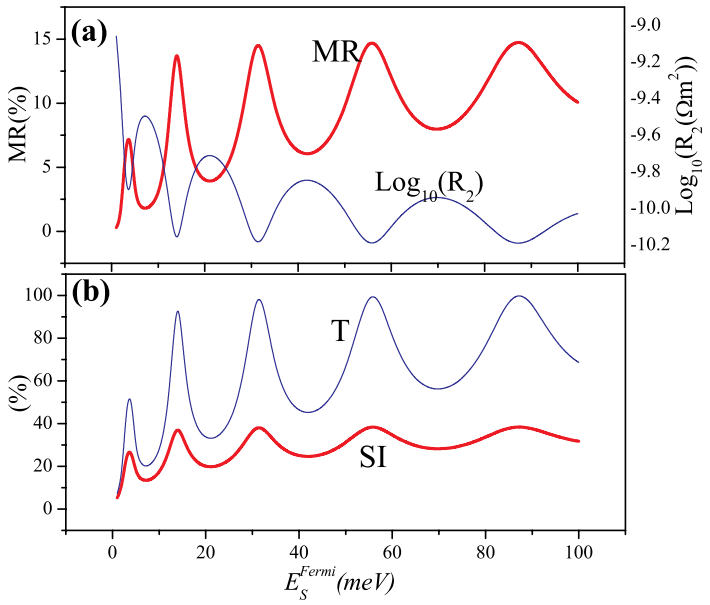

Figure 5.3: (a) Thick (Thin) line shows the MR ($\log_{10}(R_2)$) variation with change in Fermi energy of the 2DEG. (b) Thick (Thin) line shows the variation of the SI ratio (T) with the 2DEG Fermi energy.

5.1.2 Results and Discussion

Based on the self-consistency transport model described above, we investigated the spin transport behavior in the hybrid FM-2DEG structure. We focus our analysis on the effects of varying the following parameters of the 2DEG layer: i) Fermi energy (E_{FS}), and ii) width (w), on transport properties such as the MR and SI ratios, 2DEG resistance R_2, and the transmission probability T. Since the transmission curves of both spin-up and down electrons show similar oscillations with respect to E_{FS} and w, we have therefore considered the mean transmission probability, $T = (T^{\uparrow} + T^{\downarrow})/2$ across the 2DEG layer. The mean value of T is also used in calculating the MR ratio, thus indicating that the oscillatory MR effect originates from both spin channels.

Referring to Fig. 5.3(a), we obtain a general trend of decreasing resistance of 2DEG layer as the electron energy in the Fermi level, E_{FS} is increased. This is due to the

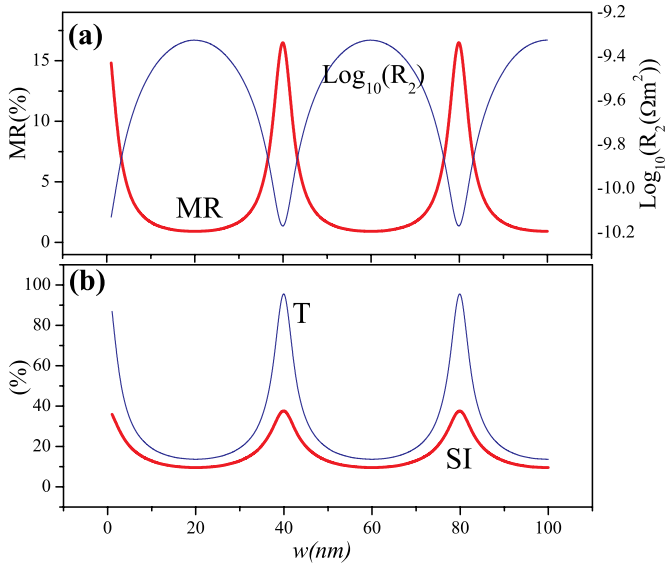

Figure 5.4: (a) Thick (thin) line shows the MR ($\log_{10}(R_2)$) variation with change in SC thickness, w. (b) Thick (thin) line shows the transmission probability, SI (T) variation with change in SC thickness, w.

fact that electrons with higher kinetic energy can transmit across the 2DEG layer more easily, as shown by the dotted curve in Fig. 5.3(b). However, the decrease in R_2 is not monotonic, but exhibits an oscillatory behavior with increasing E_{FS}. This oscillatory behavior is due to the resonant ballistic transport across the 2DEG layer of finite width w. It should be noted that in the ballistic transport, the electron energy is always larger than the potential barrier height U_2 within the 2DEG layer [see Fig. 5.2(a)]. At the resonant peaks of transmission, T approaches almost perfect transmission of 100%. Noting that R_2 is inversely proportional to electron transmission probability T [see (5.13)], the curve for R_2 in Fig. 5.3(b) thus shows an inverse dependence on E_{FS} compared to that of T.

The MR ratio exhibits an opposite trend, i.e. oscillatory increasing trend with E_{FS}, compared to R_2 [see Fig. 5.3(a)]. This may be explained as follows: when the resistance R_2 of the 2DEG layer is higher, the spin-dependent scattering within the FM layers becomes relatively less dominant. Since the spin asymmetry of R_2 is much lower

than that in the FM layers, the relative decrease in FM resistivity reduces the overall spin asymmetry of transport across the FM-2DEG structure, and thus depresses the MR ratio. The results indicate that we can in general improve the MR ratio by increasing the doping density of the SC layer, i.e increasing the Fermi level within the 2DEG conduction band. More importantly, the strongly oscillatory MR behavior can be exploited for certain applications. For instance, by changing E_{FS} either by changing the 2DEG doping level or by applying an external gate bias, one can induce a large increase in MR. This is especially at for low values of $E_{FS} < 20$ meV, where the MR changes from a low of 2% to a high of 17% within $\Delta E_{FS} \approx 5$ meV.

Next we analyze the effect of increasing 2DEG layer thickness w on the spin-dependent transport. As before, the resonant ballistic transport across the 2DEG results in an oscillatory behavior in T and hence R_2 with changing w, as shown in Fig. 5.4(a). We assume the range of w considered to be within the MFP of electrons in the 2DEG. For the parameter values used, the minimum R_2 occurs when the thickness of $w = 40$ nm, and this minimum value repeats for every $\Delta w = 40$ nm increment in the 2DEG thickness. Due to the inverse relation between MR and R_2, the MR ratio reaches a maximum value at the minimum R_2, and varies with the same period as R_2. The period of oscillation is significantly larger than the MR oscillations seen in MTJs, where Δw is typically $\sim$1-2 nm.[109,118,119] Another striking difference is the constancy of the amplitude of oscillations in the hybrid FM-2DEG device, as w is varied. By contrast, the amplitude of oscillations in MTJ devices undergoes a rapid (exponential) decrease with w.[109,118] This is because in the MTJ devices, the SPRT effect arises charge tunneling and quantum well states within the NM spacer, while in hybrid FM-2DEG devices, it is due to the ballistic transmission of free electrons across the 2DEG. The two differences

result in greater practical convenience to modulate the MR ratio in the hybrid device, because i) the large Δw values means that it is unnecessary to achieve high resolution of within a few Å in optimizing w, and ii) the constant amplitude of MR oscillations means that w can be varied without incurring an exponential suppression of MR and conductance.

In addition to the MR ratio, another important parameter for SC-based spintronics devices is the SI efficiency between the FM and SC layers. The SI ratio is defined as the spin polarization of current at the FM source electrode-2DEG interface, i.e. $\mathrm{SI} = (j_{F\uparrow} - j_{F\downarrow})/j_F = 2\beta(x = 0) - 1$. SI is calculated in parallel configuration.

The variation of SI as a function of E_{FS} and w is represented by the thick curves in Fig. 5.3(b) and Fig. 5.4(b), respectively. To explain the SI trend in Fig. 5.3(b), we note that an increase (decrease) in the 2DEG resistance R_2, and concomitant decrease (increase) in the relative contribution from the FM lead resistances, result in an overall increase (decrease) of the spin asymmetry of current through the structure. This in turn, causes a decrease (increase) in the excess majority spin current, $\Delta j = j_\uparrow - j_\downarrow$, and hence a reduction (increase) in the SI efficiency into the 2DEG. We thus obtain a variation of SI with E_{FS} [Fig. 5.3(b)] which is in tandem with that of MR, and in opposing trend to that of R_2. As for the SI trend with the width of the 2DEG layer (w) as plotted in Fig. 5.4(b), we observe an oscillatory variation of SI with w, which is similar to that of MR. In general, the SI efficiency is significantly higher than the MR ratio, and attains a maximum value of 40%, compared to the maximum MR of 16%. This is in agreement with the general approximation that $\mathrm{MR} \approx (\mathrm{SI})^2$ (see e.g. Ref[35]).

The ballistic mode of transport through the 2DEG confers the ability to tune the

SI efficiency by modifying the doping concentration or the width of the 2DEG layer, similar to the case of the MR. For instance, at low E_{FS} <20 meV, one can effect a four-fold increase in SI from 10% to almost 40% within ΔE_{FS} ≈5 meV. As for the case of MR, the ballistic mode of transport through the 2DEG confers the ability to tune the SI efficiency by modifying the doping concentration or the width of the 2DEG layer. Ballistic transmission also enables a much higher SI and MR ratios to be attained compared to hybrid SC-FM devices operated in the diffusive regime. In the latter, direct SI from a FM metal into a SC material suffers from the conductivity mismatch problem, thus yielding a SI efficiency of only $\sim 0.1\%$ and an even smaller MR ratio of $\lesssim 10^{-2}\%$.[35] By contrast, our calculations predict that in the presence of resonant ballistic transport, a maximum SI efficiency approaching 40% is attainable [see Fig. 5.3(b) and Fig. 5.4(b)]. This compares favorably even with hybrid FM-SC structures which utilize tunnel or Schottky barriers, where SI efficiency of $\sim 32\%$ has been observed.[40] In addition, in the latter structures which are based on tunneling transport, high MR and SI ratios are usually attained by increasing the tunneling resistance and hence suppressing the device conductance. They also do not exhibit the tunability of MR and SI ratios by external means, which is afforded by the resonant ballistic transport in our device, as described earlier.

5.1.3 Conclusion

We developed a model that combines the semiclassical SDD transport inside the FM electrodes, with the ballistic transmission of electrons across the 2DEG layer. Based on a self-consistency scheme, we numerically calculate the spin transport across the hybrid

FM-2DEG structure. We focus our analysis on the effects of varying the Fermi level E_{FS} and width w of the 2DEG layer, on transport properties such as the MR and SI ratios, and T across the 2DEG layer. Our calculations reveal strong oscillatory behavior in both the MR and SI ratios, owing to the ballistic resonant transport across the 2DEG, and reminiscent of the SPRT effect, recently observed in metal-based MTJ structures. Our proposed hybrid HEMT structure has several distinct advantages compared to MTJ in practical realization of the SPRT effect in future devices. These include the easy tunability of the MR and SI ratios either by changing the 2DEG doping level or gate voltage bias (which is not possible in metal-based devices) and the absence of any exponential suppression of MR with barrier thickness. Based on realistic parameter values, we predict that the hybrid HEMT is capable of achieving a maximum MR and SI ratios of approximately 20% and 40%, respectively.

5.2 Active MR device

In this section, we further propose a SC-based gate controlled MR device that performs the function of a metallic SV, but with the advantage that its MR can be optimized (post-fabrication) and its stability enhanced by controlling a gate bias voltage. Our device is a HEMT structure with electrical gates fabricated on top of the electron conduction channel. The source and the drain of the device are made of FM materials. We analyze the MR and SI behavior of this device. We also investigate the effect of the following parameters on the performance of the device: 1) channel length, 2) 2DEG and FM material choices, 3) magnetic exchange energy and 4) multiple gates vs. single gate.

As explained in the previous section, due to long MFP, ballistic transmission can be achieved in the 2DEG structure. This promises a form of low resistance tunneling MR device compared to the multilayer TMR spin valve. Another advantage of using a 2DEG structure is the ability to control electron transport by using gate voltage.[15,125–128] This enables us to optimize the MR (post-fabrication) by adjusting the gate bias. Gate

controlled MR and and spin transport have already been shown experimentally in carbon nanotube and graphene.[129–131] In this section, we proposed a SC-based MR device that could perform the function of a metal SV, but with the advantage that its MR can be optimized (post-fabrication) and its stability enhanced by controlling the gate bias voltage.

Our device consists of a HEMT structure with electric gates deposited on top of the 2DEG channel to control the electron transport.[125–128] The source and drain electrodes are made of FM materials, in which the density-of-states (DOS) of majority and minority electron states are not symmetrical. For MR measurement, the source's magnetization is fixed in one direction, while the drain's magnetization is free to rotate. The device is considered to be in the P (AP) configuration if the magnetization of both source and drain electrodes are aligned parallel (anti-parallel) to each other. Due to asymmetry in DOS, the potential barrier experienced by the electron differs in the P and AP states, and thus the electron transmission probability (T) as well as the channel resistance is different for P and AP configurations. In this design, care is taken to ensure that the electron conduction channel is much shorter than the electron's MFP in 2DEG, so as to ensure electron transport is strictly ballistic in the 2DEG.

5.2.1 Theory

To investigate electron transmission (T) across the channel we set the wave function in each region-i as follows:

$$\Psi_i(x) = \begin{pmatrix} A_i & B_i \end{pmatrix} \begin{pmatrix} \exp(+ik_i x) \\ \exp(-ik_i x) \end{pmatrix} \tag{5.14}$$

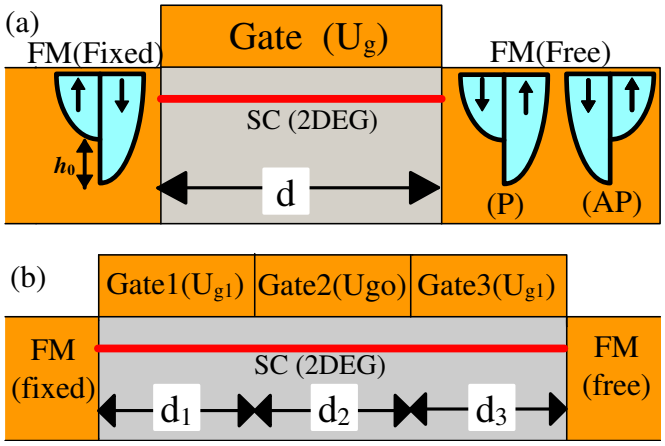

Figure 5.5: Device structure for (a) a single-gate device, (b) a triple-gate device. The band diagram and magnetic exchange energy (h_0) for FM materials in P and AP configuration are shown in (a).

where A_i and B_i are unknowns that need to be determined. The wave vector k_i is given by: $k_i = \sqrt{\frac{2m_i}{\hbar^2}(E_n - U_i)}$, where E_n is the total energy of the electron, m_i is the effective mass of the electron, and U_i is the electric potential experienced by the electron. To obtain the values of A_i and B_i at each region, we set the following boundary conditions:

$$\Psi_i(x_i) = \Psi_{i+1}(x_i) \tag{5.15a}$$

$$\frac{1}{m_i}\frac{d\Psi_i(x)}{dx}\bigg|_{x=x_i} = \frac{1}{m_{i+1}}\frac{d\Psi_{i+1}(x)}{dx}\bigg|_{x=x_i} \tag{5.15b}$$

Equation (5.15a) shows the continuity of wave function across the device and (5.15b) shows the continuity of electron flux across the device. The spatial position of the boundary in between region-(i) and ($i+1$) is given by x_i. Since there is no electron reflection in the drain electrode, B_{drain} is set to zero. Once A_i and B_i are solved, transmission

probability, T across the device is obtained as follows:

$$T = \frac{v_{\text{drain}}}{v_{\text{source}}} \frac{|A_{\text{drain}}|^2}{|A_{\text{source}}|^2} \equiv \frac{k_{\text{drain}}/m_{\text{drain}}}{k_{\text{source}}/m_{\text{source}}} \frac{|A_{\text{drain}}|^2}{|A_{\text{source}}|^2} \tag{5.16}$$

where subscripts "source" and "drain" refers to the left and right FM electrodes, respectively. Actually, a more rigorous calculation should take into consideration the self-consistent alignment of spin electrochemical potential in the FM contacts with the Fermi levels of the semiconductors. To simplify calculation, we will only focus on the ballistic spin-dependent transmission across the 2DEG channel in this case, which ultimately describes the same MR oscillatory behavior.

For a singly gated device, we divide the device into 3 regions, i.e. 1) source electrode, 2) 2DEG channel, and 3) drain electrode as shown in Fig. 5.5(a). In the P configuration, minority spin electrons in both the left and right leads will experience a potential barrier of strength h_0 due to the magnetic exchange energy in the FM layers. In AP configuration, minority spin electron in the left lead, and majority spin electron in the right lead will experience a potential barrier of strength h_0.

In the channel region, the Fermi level of 2DEG (E_{FS}) aligns with the Fermi level of the FM leads (E_{FM}). Thus, at zero gate bias, the total energy of an electron through out in the device, $E_n = E_{FM}$. Due to Fermi level alignment, the build in potential barrier in the channel region is given by, $\Delta E_F = E_{FM} - E_{FS}$, where E_{FS} is the Fermi energy of the 2DEG layer. When a gate bias voltage of V_g is applied in the channel region, the electrons in the channel region experience a potential energy of U_g which is caused by the potential barrier due to the Fermi level alignment (ΔE_F) and the potential energy due to gate bias voltage (eV_g), i.e. $U_g = \Delta E_F + eV_g$. For simplicity, in this paper

we assume U_g to be the effective gate potential, and thus the effective electron (kinetic) energy in the channel is given by, $E_{\text{eff}} = E_n - U_g = E_{FM} - U_g$. Thus the wave vector in each region is

$$k^P_{\uparrow(1,2,3)} = \sqrt{\frac{2m_{(1,2,3)}}{\hbar^2}E_n - (0, U_g, 0)} \tag{5.17a}$$

$$k^P_{\downarrow(1,2,3)} = \sqrt{\frac{2m_{(1,2,3)}}{\hbar^2}E_n - (h_0, U_g, h_0)} \tag{5.17b}$$

$$k^{AP}_{\uparrow(1,2,3)} = \sqrt{\frac{2m_{(1,2,3)}}{\hbar^2}E_n - (0, U_g, h_0)} \tag{5.17c}$$

$$k^{AP}_{\downarrow(1,2,3)} = \sqrt{\frac{2m_{(1,2,3)}}{\hbar^2}E_n - (h_0, U_g, 0)} \tag{5.17d}$$

Region-1,2, and 3 (as indicated by the subscript) refers to source, channel, and drain regions, respectively. Note that the potential barriers in the source and drain regions differ for different magnetization configuration, i.e. P or AP. Solving the flux and wave function continuity, we obtained the analytical expression for the transmission probability across the device as follows,

$$T = \left| \frac{4K_2\sqrt{K_1K_3}}{e^{i2dk_2}(K_1 - K_2)(K_3 - K_2) - (K_1 + K_2)(K_3 + K_2)} \right|^2 \tag{5.18}$$

where $K_i = k_i m_i$, and d is the channel length. By replacing (5.17) into (5.18), we can obtain T for minority and majority current in both P and AP configurations, i.e. $T^P_\uparrow$, $T^P_\downarrow$, $T^{AP}_\uparrow$, and $T^{AP}_\downarrow$.

5.2.2 Results and Discussion

Based on simple asymmetrical transmission theory, we will analyze that the resulting MR and SI of a strictly ballistic lateral device shows interesting oscillatory behavior

that can have important implications to experimental detections. In this section, we will investigate the MR and SI variation with applied gate bias voltage for two different structures, namely the 1) singly gated [Fig. 5.5(a)], and 2) triply gated [Fig. 5.5(b)] devices. We also study the effect of material and structural parameters, such as the effective mass of electron in the 2DEG (m^*_{2DEG}), the magnetic exchange energy (h_0), and the channel length (d) on the performance of this device. For the following simulation, unless otherwise stated, we use the following parameters: Fermi level in FM electrodes, $E_{\rm FM} = 5eV$, $h_0 = 0.6E_{\rm FM}$, $d = 25nm$, and $m^*_{2DEG} = 0.04me$ (InAs).

Figure 5.6 shows the variation of a)MR and b)SI with $E_{\rm eff} = E_n - U_g$. In varying $E_{\rm eff}$, we set $En = E_{\rm FM}$ and varied U_g. Therefore, $E_{\rm eff}$ indicates the change in the applied gate bias. Here we define MR and SI as:

$$MR = (G^P - G^{AP})/(G^P + G^{AP}) \tag{5.19}$$

$$SI = (G^P_\uparrow - G^P_\downarrow)/(G^P_\uparrow + G^P_\downarrow) \tag{5.20}$$

where $G^{P,AP}_{\uparrow,\downarrow} = (q^2/h)T^{P,AP}_{\uparrow,\downarrow}$.[132] Note that SI was calculated at parallel configuration.

The plot in Fig. 5.6(a) shows an oscillating MR trend with increasing $E_{\rm eff}$. In fact MR oscillates between positive and negative values in the low energy range. In the higher energy range, i.e, $E_{\rm eff} > 0.5E_{FM}$, oscillation occurs mainly within the positive MR region. The oscillatory behavior we revealed here provides important information to experimentalists with respect to device optimization. Before device fabrication, channel length and other device parameters have to be carefully optimized. Once the device has been optimized during fabrication, gate bias provides the fine tuning of the MR strength to achieve high MR. At some voltage points, MR can be eliminated completely from the

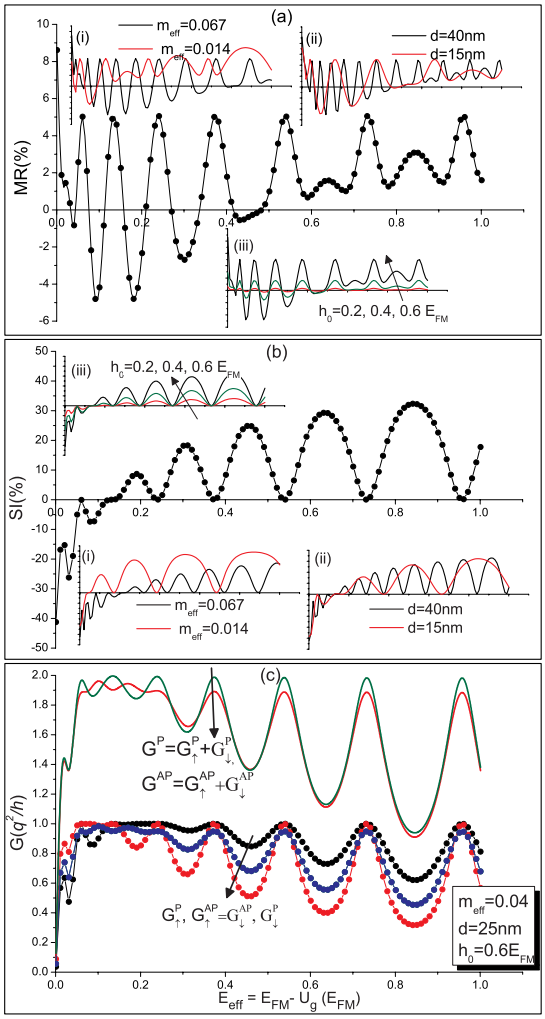

Figure 5.6: (a) MR (b) SI variation for a single-gate device. (i), (ii),and (iii) shows the effects of 2DEG effective mass, channel length and magnetic exchange energy of the FM material, respectively. (c) Conductance variation for majority and minority current in P and AP configurations. Unless otherwise indicated on the graph the material parameters are shown in the box at the right of the figure. SI is computed at P configuration.

device, in which case the device provides only simple functions of biasing and matching; in electrical term, this device acts as a buffer.

Figure 5.6a(i) shows the MR oscillation when different materials are used for the 2DEG layer. Materials with lower effective mass, e.g. InAs ($m^* = 0.014me$) results in a lower frequency of MR oscillation. Besides, the average MR value is also higher when the effective mass is lower. The reduction in the MR oscillation frequency also causes the device to be less sensitive to small changes in gate voltage. This effect is desirable

as it increases the stability of the device while maintaining the advantage of fine-tuning MR with gate voltage. Next we analyze the effect of increasing the channel length in Fig. 5.6a(ii). Our results show that when the channel length is 15nm as opposed to 40nm, MR oscillation reduces its frequency. In the case of shorter channel length with lower frequency, we also noticed that the MR oscillation shifts to mainly within positive values at a lower energy value. Thus device with shorter channel length and lower 2DEG effective mass is more preferred as far as the ease of optimization is concerned. Unlike effective mass and channel length, results in Fig. 5.6a(iii) show that variation in the magnetic exchange energy of the FM material has no effect on the frequency of the MR oscillation. However, the average MR values increases considerably with increasing h_0. This observation is consistent with well-accepted understanding that FM materials with higher spin-asymmetry in DOS could increase the MR values of SV devices.

The variation of SI with E_{eff} is plotted in Fig. 5.6(b). The SI vs. E_{eff} curve also shows an oscillatory trend with an increasing average magnitude. The effect of h_0, d, and m_{eff} on SI is similar to the effect of these parameters on MR. However the oscillation frequency of the MR curve is two times greater than the oscillation frequency of the SI curve. The oscillation of both MR and SI is related the oscillation of the conductance, G [refer Fig. 5.6(c)]. It can be seen that a peak in MR curve is obtained whenever there is either a peak or a valley in the G curve. This result is significant as it enables us to obtain high MR (MR peak) at high conductance (conductance peak). However the relation between SI and G is different. Each peak (valley) in the SI curve corresponds to a valley (peak) in the G curve. This result is undesirable because large SI is obtained when the G is low. Therefore the gate bias should be tuned such that both SI and G are optimized.

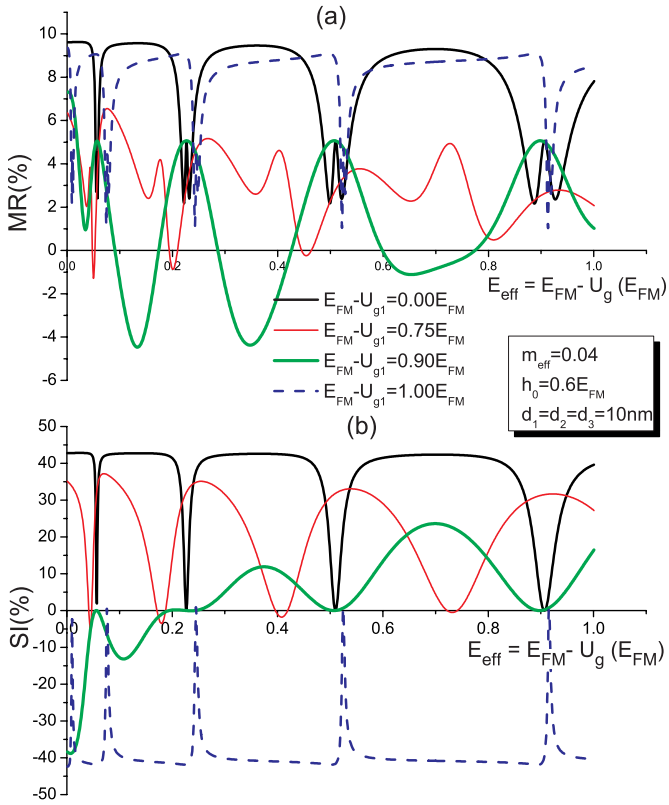

Figure 5.7: (a) MR and (b) SI variation for a triple-gate device. Unless otherwise indicated on the graph the material parameters are shown inside the box atthe right of the figure.

We will now study the MR and SI variation in a similar device but with three gates as shown in Fig. 5.5(b). In this structure, we designed the channel to be of total length $d = 30nm$ with each gate taking up a length of $10nm$. The effective gate potential, U_{g1} or U_{g0}, is applied at the gates in the way shown in Fig. 5.6(b). In Fig. 5.7, we varied U_{g0} while fixing the value of U_{g1}. For extreme values of U_{g1} values, i.e. $U_{g1} = 0E_{FM}$ and $U_{g1} = 1E_{FM}$, high average and relatively less oscillatory MR values has been obtained for a large range of U_{g0}. This simple simulation shows that the magnitude of MR and SI as well as the stability of the device can be improved rather significantly by using a triple gate device structure when optimized with appropriate gate bias values.

5.2.3 Conclusion

We have designed a semiconductor based MR device that could perform the function of a metal SV, but with the advantage that its MR can be optimized (post-fabrication) and its stability enhanced by modulating resonant transmission of electron with gate bias voltage. We showed that short channel length and low effective mass reduces MR oscillation frequency, a feature we call stabilization which makes MR optimization easy to carry out. Our observation of average MR increasing with the magnetic exchange energy is consistent with general understanding of the role played by spin asymmetry in FM materials in contributing to MR. Last, we designed a triple-gate ballistic device that shows even more predictable MR behavior compared to the single-gate structure. With lateral device feature size approaching sub-10nm in CMOS technology, ballistic oscillatory MR behavior should be evident in the device we proposed above and should be investigated in greater depth for possible applications in recoding or low field sensing.

5.3 Summary

We studied electron and spin transport across a 2DEG structure. Across the 2DEG layer, ballistic transport is assumed, given the long MFP within the 2DEG. We found that the transport properties of the device, such as the transmission probability, the SI efficiency and the MR ratio, all exhibit oscillatory behavior when the 2DEG layer width or the 2DEG Fermi energy is varied. The basis of these oscillations is the resonant transport across the 2DEG. By utilizing this resonant transport property, we further proposed a SC-based gate controlled MR device that could perform the function of a metallic SV, but with the advantage that its MR can be optimized (post-fabrication) and its stability

enhanced by controlling a gate bias voltage.

Chapter 6

Introduction to Green's Function

6.1 Mesoscopic Transport

Recently, the advancement in nanofabrication has led to the introduction of various nanostructures such as quantum wire, quantum dots, and molecular devices. The dimensions of these structures are so small that electron transport is no longer governed by classical diffusive equations. In the mesoscopic regime, electron phase is conserved and electronic transport is highly influenced by the quantum nature of electron. Interest in quantum transport in mesoscopic regime is increasing enormously. Recently many researchers have adopted Green's Function[84–86] method for modeling electron transport at the atomic level. Electron transport in carbon nanotubes,[133] metal nanowires,[134,135] atomic/molecular[136–138] devices have also been numerically studied using the Green's function method.

6.2 Electron Transport

6.2.1 Macrosopic (*Top-Down*) View

In macroscopic view, the length of a device is long enough such that electron diffuses along the channel, being scattered many times. According to Ohm's Law, when there is a potential difference, V and the resultant current is I, the conductance of the channel, $G = I/V$ is given by $G = \sigma A/L$, where A, L, and σ are cross sectional area, length and conductivity of the channel, respectively. The conductivity is a function of scattering time, τ, density of state, n and effective mass, m, i.e. $\sigma = e^2 n\tau/m$. However, in nanoscale transport, this description fails to describe the electron motion. For example in a ballistic device, there is no scattering and thus τ is undefined. Similarly, in molecular conductors, m and n are undefined.

6.2.2 Microscopic (*Bottom-Up*) View

6.2.2.1 Electron as Particle

In this section we will describe the electron transport from a microscopic view. Referring to Fig. 6.1, when we apply a finite potential bias, V_b across the source (left lead) and drain (right lead), there will be a finite difference between the electrochemical potential of the left, μ_L and right, μ_R leads, i.e. $\mu_L - \mu_R = eV_b$. At zero temperature, the current flows through the channel only when there is at least one energy state (filled or empty) in between μ_L and μ_R. Under such condition, the left lead tries to fill up the state and the right lead tries to empty the state, hence there is steady state electron flow. For energy states located above (below) μ_L (μ_R), both the source and drain will try to fill up (empty)

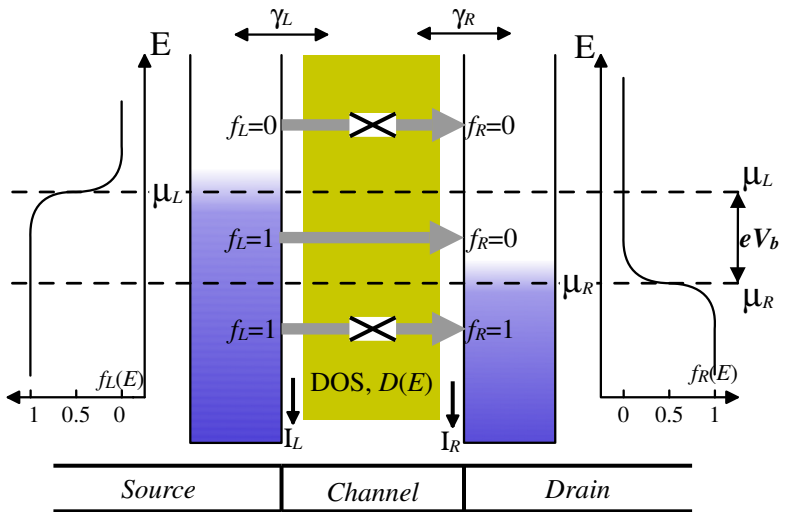

Figure 6.1: Electron transmission from source to drain in a nanodevice.

these states. Therefore no current flows across these states. In other words, for current to flow the Fermi function on the left, f_L and right, f_R of an existing energy state, E must be different, i.e. $f_L(E) \neq f_R(E)$.

Note that the above explanation is valid only when the temperature is 0 K. For higher temperature Fermi function will broaden and thus there will be current flow in the vicinity of μ, i.e. slightly above (below) $\mu_{1(2)}$.

Next we analytically derive the current, I across the device. The number of electron on the left (right) contacts are given by,

$$N_{L(R)} = 2f_{L(R)}(E), \tag{6.1}$$

where $f_{L(R)}(E) = f_0(E - \mu_{L(R)})$ and $f_0(E) = 1/(1 + e^{E/k_BT})$ is the Fermi distribution function. We set $\mu_{L(R)} = E_F + (-)eV_b/2$, where E_F is the intrinsic Fermi level of the leads. The factor 2 in (6.1) is due to the fact that each state can be occupied by two electrons (spin-up and spin-down). Current, $I_L(I_R)$ from (to) left (right) contact is given

by

$$I_L = e\frac{\gamma_L}{\hbar}(N_L - N) \tag{6.2a}$$

$$I_R = e\frac{\gamma_R}{\hbar}(N - N_R) \tag{6.2b}$$

where N is the total number of electrons at steady state in the channel, and escape rate, $\gamma_{L(R)}/\hbar$ [1/*time*] is the rate at which electron crosses from the lead to the channel. Escape energy, γ [*energy*] indicates how easily electron can escape into contacts. In the steady state, the number of incoming electrons are equal to the number of outgoing electrons, and hence the steady state current, $I = I_L = I_R$. Thus I and N are obtained as follow

$$N = \frac{\gamma_L N_L + \gamma_R N_R}{\gamma_L + \gamma_R} \tag{6.3}$$

$$I = \frac{2e}{\hbar}\frac{\gamma_L \gamma_R}{\gamma_L + \gamma_R}\left(f_L(\varepsilon) - f_R(\varepsilon)\right) \tag{6.4}$$

Note that, as explained earlier, current is finite only when $f_L(E) \neq f_R(E)$. To simplify further discussions, we assume $\gamma = \gamma_L = \gamma_R$ and obtain a simpler expression for current, i.e.

$$I = \frac{e}{\hbar}\gamma\left(f_L(E) - f_R(E)\right) \tag{6.5}$$

Using Taylor's expansion under the small bias condition where $V_b \to 0$, we obtain

$$\lim_{V_b \to 0}\left[f_L(E) - f_R(E)\right] = e\Delta V \cdot F_T\left[E - E_F\right] \tag{6.6}$$

where $e\Delta V = \mu_L - \mu_R|_{V_b \to 0} \to 0$ and $F_T(E) = -df_0(E)/dE = \left[4k_BT.\cosh^2(E/2k_BT)\right]^{-1}$. Substituting this into (6.5), we derive the current at small voltage:$\Delta I = \frac{e}{\hbar}\gamma \cdot e\Delta V F_T[E - E_F]$. From this equation, the expression for conductance, $\Delta I/\Delta V$ appears to be: $(e^2/\hbar)\gamma F_T[E -$

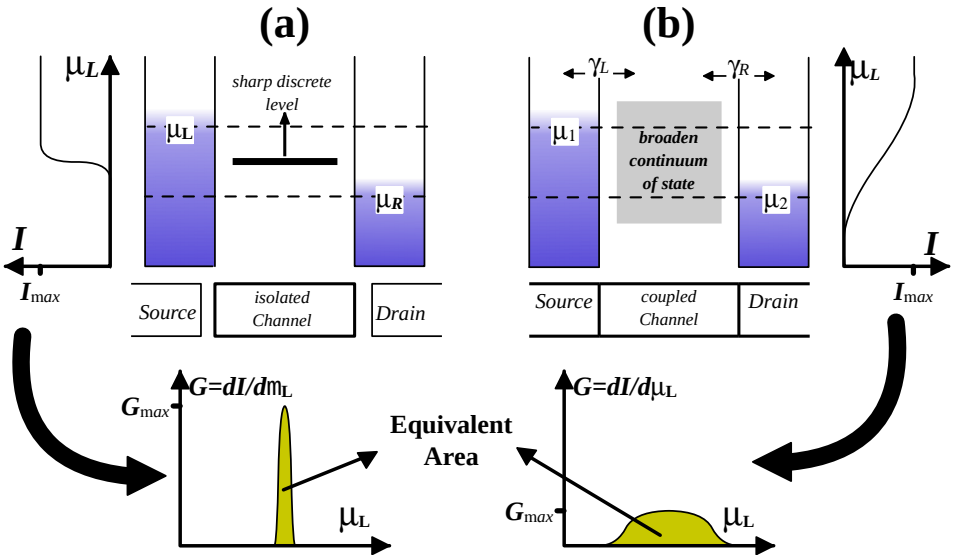

Figure 6.2: A discrete energy state in a isolated channel broadens when the channel is coupled with external contacts. This coupling effect lowers the resultant G_{max}. The graph in (a) are plotted assuming no broadening in the energy state when external contacts are connected to the channel.

$E_F]$. This expression does not have an upper limit since $F_T \rightarrow \infty$ at temperature T=0K. However in reality, there is an upper limit for conductance in a ballistic channel.

This upper limit is due to the energy broadening in the channel. When voltage is applied to the contacts, each sharp discreet state in the channel broadens out and becomes a continuum of states. The continuum of states formed by one discreet state is electronically equivalent to one state, i.e. can only accommodate one pair of electrons. Figure 6.2(b), illustrates how the current curve "broadens out" due to the broadening of states. As the state broadens out, some of it will lie within the non-conducting regions, i.e. much above (below) $\mu_1(\mu_2)$. Since there is no current flow in the non-conducting regions, the total current and maximum conductance is reduced [see Fig. 6.2(a)].

Density of states (DOS) indicates the number of states per unit energy. The broadened DOS, $D(E) = \frac{\gamma/\pi}{(E-\varepsilon)^2+\gamma^2}$, where ε is the energy level of the discreet state. The total

current through all the states is given by

$$\begin{aligned} I &= \int_{-\infty}^{+\infty} \underbrace{dE \cdot D(E)}_{\text{total states}} \cdot \underbrace{\frac{e}{\hbar}\gamma\left(f_1(E) - f_2(E)\right)}_{\text{Current/state}} \\ &= \frac{e}{\pi\hbar}\int_{-\infty}^{+\infty} dE \cdot T(E) \cdot \left(f_1(\varepsilon) - f_2(\varepsilon)\right) \end{aligned} \tag{6.7}$$

where transmission probability $T(E) = D(E)\pi\gamma$. Note that T(E) varies from 0 to 1. At low temperature F_T approaches delta function, i.e. $\lim_{T\to 0K} F_T\left[\varepsilon\right] = \delta(\varepsilon)$. From (6.6) and (6.7), the total current at small voltage, $V_b \to 0$ and low temperature, $T \to 0K$ is given by

$$\begin{aligned} \lim_{V_b\to 0} \Delta I &= \frac{e^2}{\pi\hbar}\int_{-\infty}^{+\infty} dE \cdot T(E) \cdot \Delta V F_T[E - E_F] \\ \lim_{V_b\to 0, T\to 0K} \Delta I &= \frac{e^2}{\pi\hbar}\int_{-\infty}^{+\infty} dE \cdot T(E) \cdot \Delta V \delta[E - E_F] \\ &= \frac{e^2}{\pi\hbar} T(E_F).\Delta V \end{aligned} \tag{6.8}$$

The maximum conductance, G_{max} occurs when the transmission is maximum, i.e. T(E)=1. Thus G_{max} is given by

$$G_{\max} = \frac{\delta I_{\max}}{\delta V} = \frac{q^2}{\pi\hbar} T(E_F)_{\max} = \frac{2q^2}{h}(1) = \frac{1}{12.9} k\Omega^{-1} \tag{6.9}$$

The maximum conductance is also known as quantum conductance. Quantum conductance is the maximum conductance of a mesoscopic channel.

6.2.2.2 Electron as wave (Quantum Regime)

6.2.2.2.1 Wave function (WF) In the previous section transport mechanism was studied in terms of electron density. In quantum regime electrons behave as wave, and

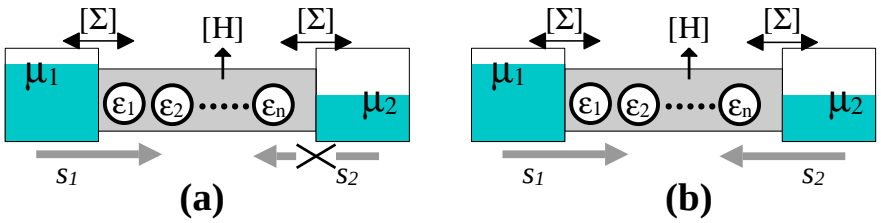

Figure 6.3: Modeling electron transport in quantum regime.

thus calculations are done in terms of wave function(WF), ψ, where the electron density is given by, $n = \psi\psi^*$. The electron energy of an isolated channel is described by the following Schrödinger equation

$$E\psi = \varepsilon\psi \Rightarrow (E - \varepsilon)\psi = 0 \tag{6.10}$$

ε is the average energy level in the channel. When the isolated channel is connected to the contacts, the above equation is modified as follows:

$$[E - \varepsilon + i\gamma_L/2 + i\gamma_R/2]\,\psi = 0 \tag{6.11}$$

where γ_L and γ_R are energy terms due to left and right contacts, respectively. This can be justified by analyzing the time dependent Schrödinger equation (i.e. by replacing $E = -i\hbar d/dt$). Equation (6.11) shows that at steady state there are no electrons in the contacts. This is because we did not include the source term in the above model. Now, we include an electron source in the left contact (there is no electron coming from right contact). The Schrödinger equation for the model with only one electron source is given by

$$[E - \varepsilon + i\gamma_L/2 + i\gamma_R/2]\,\psi = s_L \tag{6.12}$$

where the source term, s_L describes the electron that come in from the left contact. The strength of this source is set to $s_L s_L^* = \gamma_L f_L$, such that we obtain results consistent

with previous calculations. With this substitution we obtain the expressions for WF (ψ), electron density (n_L), and the total number of electron (N_L) as follows

$$\psi(E) = \frac{s_L}{E - \varepsilon + i\gamma_L/2 + i\gamma_R/2} \tag{6.13a}$$

$$n_L(E) = \psi(E)\psi^*(E) = \frac{\gamma_L f_L}{(E-\varepsilon)^2 + (i\gamma_L/2 + i\gamma_R/2)^2} \tag{6.13b}$$

$$N_1 = \int \frac{dE}{2\pi} n_1(E) = \frac{\gamma_L f_L}{\gamma_L + \gamma_R} \tag{6.13c}$$

The expression for N_L is consistent with that we obtained previously [refer (6.3)] .

Until now, we studied the electron transport by considering a single grid point with an average energy level, ε in the channel region. For a more general model, the channel is discretized into multiple grid points (MGP), with a series of energy levels–$\varepsilon_1, \varepsilon_2, \varepsilon_3, ...$– [refer Fig. 6.3] . In MGP model, all the physical parameters will be replaced with matrices, and thus the Schrödinger equation is

$$[E\mathbf{I} - H - \Sigma_L - \Sigma_R]\{\psi\} = \{S_L\} \tag{6.14}$$

where [**I**] is an identity matrix, $\Sigma_{L(R)}$ are self energy matrix due to the contacts, and S_L is the source matrix. H is the Hamiltonian matrix which describes the energy in each grid point, ε_i and the coupling energy, t between the points. For a system with n grid points, the explicit form of $\Sigma_{L(R)}$ and S_L matrix is as follows:

$$\Sigma_{L(R)} = \begin{bmatrix} -\frac{i\gamma_L}{2}\,(0) & 0 & \cdots & 0 \\ 0 & \vdots & \vdots & \vdots \\ \vdots & \vdots & \vdots & 0 \\ 0 & \cdots & \cdots & 0\left(-\frac{i\gamma_R}{2}\right) \end{bmatrix}; S_L = \begin{bmatrix} s_L \\ 0 \\ \vdots \\ 0 \end{bmatrix}$$

The explicit form of $[H]$ depends on the Hamiltonian of the system. The matrix version of $\gamma_{L(R)}$ is given by the broadening matrix, $\Gamma_{L(R)} = i\left[\Sigma_{L(R)} - \Sigma^{\dagger}_{L(R)}\right]$.

Till now we have considered only one source term, S_L [Fig. 6.3a]. Next, we will try to incorporate the second source term (from the right contact), S_R [Fig. 6.3b]. Note that S_R cannot be simply added to S_L, because WFs excited by uncorrelated sources cannot be added. Such addition will result in incorrect expressions for n_L and N_L. To overcome this problem we introduce the concept of correlation Green's function (GF).

6.2.2.2.2 Non Equilibrium Green's Function (NEGF) Since we cannot superimpose the WF from different source, we define a correlation GF

$$G^n(\equiv -iG^<) = \psi\psi^\dagger \tag{6.15}$$

The diagonal element of G^n indicates the electron density at each point. Next, we define the retarded GF,

$$G^R = [EI - H - \Sigma_1 - \Sigma_2]^{-1} \tag{6.16}$$

G^R is the impulse response of the system, i.e. the response obtained when the system is excited by a unit source. From (6.12) and (6.16), we obtain the WF due to single source, $S_L : \psi = G^R S_L$. Referring to (6.15), we express the G^n in terms of the source term

$$G^n = \psi\psi^\dagger = G^R S_L S_L^\dagger G^{R\dagger} = G^R \Gamma_L f_L G^A \tag{6.17}$$

where $S_L S_L^\dagger = \Gamma_L f_L$ and $G^A = G^{R\dagger}$. G^A is known as advanced GF. To add another source, S_R, we can just superimpose the correlation function of the second source and obtain

$$G^n = f_L G^R \Gamma_L G^A + f_R G^R \Gamma_R G^A \tag{6.18}$$

From GF, we can derive other physical parameters as follows:

Spectral Function

$$A = G^R \Gamma_L G^A + G^R \Gamma_R G^A = i\left[G^R - G^A\right]$$

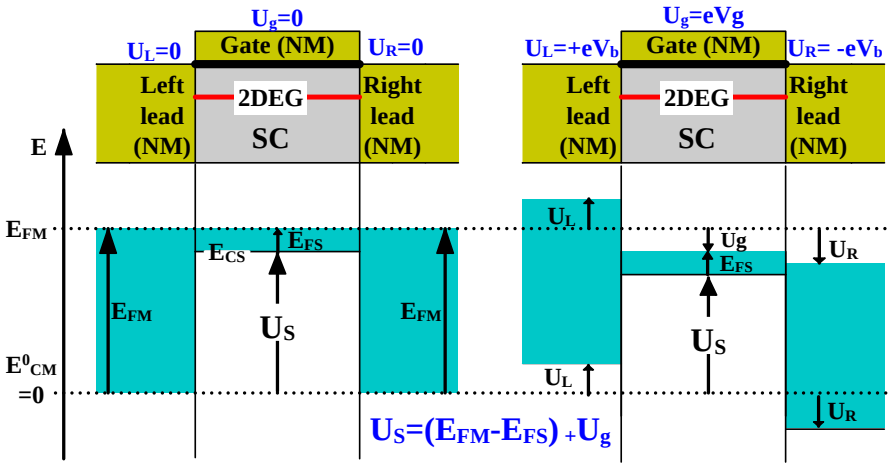

Figure 6.4: (a) Schematic illustration of the 2DEG-based field device and the band-diagram subject to external bias.

Note that spectral function is obtained by setting $f_L = f_R = 1$ in G^n [(6.18)].

Transmission Probability

$$T(E) = Trace(\Gamma_L G^R \Gamma_R G^A)$$

Current(Coherent transport)

$$I = \frac{q}{h} \int dE\ T(E)\ \ (f_R - f_L)$$

Current(general version)

$$I_{L(R)} = \frac{q}{\hbar} Trace\left(\Gamma_{L(R)} A f_{L(R)} - \Gamma_{L(R)} G^n\right)$$

6.3 Tight Binding Greens Function formulation for a mesoscopic system with magnetic and electric barriers

In this section, we will use GF to model the electron transport and compute the current in a ballistic 2DEG system with applied external magnetic and electric fields spatially

distributed in the x direction.

6.3.1 Matrix Representation of Hamiltonian

First, we obtain the matrix representation of the Hamiltonian operator. The system under consideration is a 2DEG system having translational invariance along the transverse y direction, and applied external magnetic and electric fields spatially distributed in the x direction. For this system the Hamiltonian is described as follows:

$$H = \frac{\left[i\hbar\nabla + \mathbf{A}\right]^2}{2m^*} + U_S + \frac{g\hbar\sigma B_z}{4m_0} + E_y \tag{6.19}$$

where m^* is the electron effective mass, m_0 is the electron mass in vacuum, g is the effective Land g-factor and U_S is the total potential energy of the electron in the semiconductor. B_z is the vertical external magnetic field at x, A is the corresponding magnetic vector potential chosen in the Landau gauge $(0, A_y(x), 0)$, and σ is $+1/-1$ denotes spin up/down, respectively and where the spin quantization axis is defined along the vertical magnetic fields. The electron conduction path in the x direction is discretized into n lattice points of equal distance a apart, i.e. the discrete points are denoted by $x_j = ja$, where $1 < j < n$.

We can now derive the matrix representation of the Hamiltonian of (6.19) by applying the finite difference approach, in the limit of small a. If $F(x)$ is the eigenfunction of the system, which need not be solved analytically, then from (6.19), we have:

$$HF\left(x\right) = -\frac{\hbar^2}{2m}F''\left(x\right) + \frac{i\hbar A_x\left(x\right)}{m}F'\left(x\right) + \left(\frac{A_x\left(x\right)^2}{2m} + U\left(x\right) + \frac{g\hbar\sigma B_z\left(x\right)}{4m} + E_y\right)F\left(x\right) \tag{6.20}$$

For small a, i.e. $a \to 0$, the first and second derivatives of $F(x)$can be approxi-

mated as:

$$F'(x)|_{x=ja} \approx \frac{F_{j+1/2} - F_{j-1/2}}{a}, \tag{6.21}$$

$$F''(x)|_{x=ja} \approx \frac{F_{j+1} - 2F_j + F_{j-1}}{a^2} \tag{6.22}$$

where for compactness, $F_j = F(x)|_{x=ja}$. With the above approximations, and denoting $A_y(x)$, $U(x)$, and $B_Z(x)$ at $x = ja$ by A_j, U_j, and B_j, respectively, we can rewrite (6.20) as:

$$\begin{aligned} HF(x)|_{x=ja} &= -\frac{\hbar^2}{2m}\left(\frac{F_{j+1} - 2F_j + F_{j-1}}{a^2}\right) + \frac{i\hbar A_j}{m}\left(\frac{F_{j+1/2} - F_{j-1/2}}{a}\right) \\ &\quad + \left(\frac{A_j^2}{2m} + U_j + \frac{g\hbar\sigma B_j}{4m} + E_y\right) F_j \end{aligned} \tag{6.23}$$

or equivalently,

$$HF_j = (-t_j)\,F_{j-1} + (-iq_j)\,F_{j-1/2} + (2t_j + \omega_j + Z_j + U_j + E_y)\,F_j + (iq_j)\,F_{j+1/2} + (-t_j)\,F_{j+1} \tag{6.24}$$

where $t = t_j = \hbar^2/2ma^2$, $q_j = \hbar A_j/2ma = (A_j a/\hbar)\,t$, $\omega_j = A_j^2/2m = (A_j a/\hbar)^2\,t$, and $Z_j = g\hbar\sigma B_j/4m_0$. Taking $q_j F_{j+1/2} \approx q_{j+1/2} F_{j+1}$ and $q_j F_{j-1/2} \approx q_{j-1/2} F_{j-1}$ to simplify calculation, one obtains the difference equation $HF_j \equiv Q_j^* F_{j-1} + P_j F_j + Q_j F_{j+1}$, where $P_j = 2t_j + \omega_j + Z_j + U_j$, $Q_j = -t_j + iq_{j+1/2}$. Note that $q_{j+1/2}$ is obtained by evaluating $A_j(x)$ at halfway between x_j and x_{j+1}. Equation (6.24) can be written in

a more compact form: $HF(x)|_{x=ja} = \sum_i H(j,k)F_j$, where

$$H(j,k) = \begin{cases} Q_j^*, & k = j+1, \\ P_j, & k = j, \\ Q_j, & k = j-1, \\ 0, & \text{otherwise}, \end{cases} \tag{6.25}$$

Thus in matrix form, the Hamiltonian is given by:

$$H = \begin{bmatrix} P_1 & Q_1^* & 0 & \cdots & 0 \\ Q_1 & P_2 & \ddots & \ddots & \vdots \\ 0 & \ddots & \ddots & \ddots & 0 \\ \vdots & \ddots & \ddots & P_{n-1} & Q_{n-1}^* \\ 0 & \cdots & 0 & Q_{n-1} & P_n \end{bmatrix} \tag{6.26}$$

where n is the number of discrete points in the 2DEG.

6.3.2 Green's Function and Self-Energy

We model our device as a finite-sized conduction path in the 2DEG, which is connected on either side to semi-infinite leads. Thus, from the discretized Hamiltonian of (6.26), we can then derive the retarded Green's function matrix, G^R for the 2DEG region, fol-

lowing standard methods[84][refer (6.16)].

$$
\begin{aligned}
G^R &= \left[E\mathrm{I} - H - \left(\sum_L^R + \sum_R^R\right)\right]^{-1} \\
&= \begin{bmatrix}
E_x - P_1 - \sum_L^R(1,1) & -Q_1^* & 0 & \cdots & 0 \\
-Q_1 & E_x - P_2 & \ddots & \ddots & \vdots \\
0 & \ddots & \ddots & \ddots & 0 \\
\vdots & \ddots & \ddots & E_x - P_{n-1} & -Q_{n-1}^* \\
0 & \cdots & 0 & -Q_{n-1} & E_x - P_n - \sum_R^R(n,n)
\end{bmatrix}
\end{aligned}
\tag{6.27}
$$

where E represents the total electron energy, E_x is the electron energy in the propagation (x)-direction, and $\sum_L^R$ and $\sum_R^R$ are the self-energies of the left and right lead, respectively. Note that G^R is independent of the kinetic energy in the transverse direction $E_y = \left(\hbar^2 k_y^2 / 2m^*\right)$, due to the cancelation of the E_y component in E and H in (6.27). Since electron transport is constrained to the $x-y$ plane of the 2DEG, the confinement in the z-direction will lead to the formation of sub-bands. We would not discuss the details concerning the sub-bands, and assume that transport occurs only within the lowest sub-band. The component G_{ij}^R describes the propagation of electron between the points x_i and x_j within the 2DEG channel, while the self-energy terms of $\sum^R = \sum_L^R + \sum_R^R$ represent the perturbative effect of the entire semi-infinite leads on the electron propagation within the channel. $\sum_{L,R}^R$ is related to the surface Green's function of the isolated leads, $g_{L,R}$, and can be expressed as follows:

$$
\sum_L^R(j,i) = \begin{cases} t_L g_L t_L, & i=j=0 \\ 0, & else\ where \end{cases} \quad ; \quad \sum_R^R(j,i) = \begin{cases} t_R g_R t_R, & i=j=n \\ 0, & else\ where \end{cases} \tag{6.28}
$$

where $t_{L(R)}$ is the coupling energy between the right (left) edge of the left (right) lead with the leftmost (rightmost) discrete point of the 2DEG. In the flat-band approximation, the Green's function of an isolated semi-infinite lead is given by $g_{L,R} = -\frac{1}{t}\exp\left(ik_{L,R}a_{L,R}\right)$, where $a_{L,R}$ is the unit cell length of the discretized lead, $k_{L(R)} = \sqrt{2m\left(E - (E^0_{CM} + U_{L(R)})\right)/\hbar^2}$, E^0_{CM} is defined to be the bottom conduction energy level of the metallic lead in the absence of external potential. This energy level is set to zero for convenience. Potential energy could be imparted to the system by applying bias $U_{L,(R)} = +(-)eV_b$ to the left (right) lead [refer Fig. 7.1].

As explained in Sec. 6.2.2.2, we note that the advanced Green's functions and self-energies are given by the complex conjugates of the corresponding retarded functions, respectively, i.e. $G^A = \left[G^R\right]^\dagger$ and $\sum^A_{L.R} = \left[\sum^R_{L.R}\right]^\dagger$, while the coupling function of the conductor to the lead can be obtained from the relation $\Gamma_{L,R} = i\left(\sum^R_{L,R} - \sum^A_{L,R}\right)$.

6.3.3 Spin Dependent Transmission Probability and Current

Following Caroli et al. and others,[139–143] the spin current expression is given by:

$$I_{\uparrow,\downarrow} = \sum_{k_y} \frac{q}{h} \int_{-\infty}^{+\infty} \left(f_L(E) - f_R(E)\right) T_{\uparrow,\downarrow}(E) dE \tag{6.29}$$

where $T_{\uparrow,\downarrow}(E) = \text{trace}\left[\Gamma_L G^R_{\uparrow,\downarrow} \Gamma_R G^A_{\uparrow,\downarrow}\right]$, with $G^{A,R}_{\uparrow(\downarrow)}$ being the Green's functions corresponding to $\sigma = +1\,(-1)$.

This expression for current is identical with the expression in (6.29). Recalling from Sec. 6.2.2, $f_{LR}(E) = \left[1 + \exp\left(\frac{E-\mu_{LR}}{kT}\right)\right]^{-1}$ is the Fermi-Dirac function of the left and right leads, taking into account the electrochemical potential at the leads, $\mu_{L(R)} = E_F + (-)eV_b/2$, with E_F being the intrinsic Fermi energy of the lead.

Considering single-mode transport, i.e. corresponding to a single transverse wave-vector k_y, neglecting the sub-band energies due to confinement in the $-$direction, the single-mode spin current is then given by:

$$I^S_{\uparrow,\downarrow}(k_y) = \frac{e}{h}\int \left(f_L\left(E_x+E_y\right) - f_R\left(E_x+E_y\right)\right) T_{\uparrow,\downarrow}\left(E_x\right) dE_x$$

, where the superscript S denotes single-mode transport.

6.3.4 Conductance at zero bias and zero temperature

Equation (6.29) can be simplified under small bias condition, i.e. $(\mu_L - \mu_R) = eV_b \rightarrow 0$, where the difference in the Fermi-Dirac functions becomes $\lim_{V_b\rightarrow 0}\left[f_L\left(E\right) - f_R\left(E\right)\right] = F_T\left(E-E_F\right)eV_b$, with $F_T\left(\varepsilon\right) = -df_{L,R}\left(\varepsilon\right)/d\varepsilon$. Further simplification occurs in the limit of low temperature, where $F_T\left(\varepsilon\right)$ approaches the Dirac delta-function, i.e. $\lim_{T\rightarrow 0} F_T\left(\varepsilon\right) = \delta(\varepsilon)$. In the low bias, low temperature limit, the above simplifies to:

$$\lim_{V_b,T\rightarrow 0}\Delta I^S_{\uparrow,\downarrow}(k_y) = V_b\frac{q^2}{h}\int \delta\left(E_x+E_y-E_F\right)T_{\uparrow,\downarrow}\left(E_x\right)dE_x = V_b\frac{q^2}{h}T_{\uparrow,\downarrow}\left(E_F-E_y\right) \tag{6.30}$$

which then leads to the single-mode spin conductance expression of:

$$G^S_{\uparrow,\downarrow}(k_y) = \lim_{V_b,T\rightarrow 0}\frac{\Delta I^S_{\uparrow,\downarrow}(k_y)}{V_b} = \frac{q^2}{h}T_{\uparrow,\downarrow}\left(E_F-E_y\right) = \frac{q^2}{h}T_{\uparrow,\downarrow}\left(E_F-\hbar^2k_y^2/2m\right) \tag{6.31}$$

One can then obtain the corresponding conductance expression for the case of multi-mode transport by integrating over k_y. For the specific case of zero transverse kinetic energy (i.e. $k_y = 0$), the conductance is given by $G^S_{\uparrow,\downarrow}(0) = \frac{e^2}{\hbar}T_{\uparrow,\downarrow}\left(E_F\right)$, which depends on the transmission function at the Fermi level.

6.4 Summary

In this chapter we have developed a theoretical model, based on tight-binding GF method, to describe electron transport in mesoscopic regime. In the following chapters, we will apply this model to study the microscopic effects affecting spin transport phenomena, and thus optimize the performance of spintronics devices.

Chapter 7

Ballistic Spin Transport across Magnetic-Electric Barriers

In this chapter we apply the GF model, which was described in the previous chapter, to study the effect of spin transport and optimization of SI across a magnetic-electric barrier in a spin transistor device. We proposed that a viable form of spin current transistor is one to be made from a single-mode device which passes electron through a series of magnetic-electric barriers built into the device. The barriers assume a wavy spatial profile across the conduction path due to the inevitable broadening of the magnetic fields. Field broadening results in a monotonically increasing magnetic vector potential across the conduction channel, which increases spin polarization. We have identified that the important factors for generating high spin polarization and conductance modulation are the low source-drain bias, the broadened magnetic fields, and the high number of FM gates within a fixed channel length.

7.1 Theory

Previous studies[126, 144–146] have shown that magnetic and electric barriers could be realized by applying electrostatic potential and edge magnetic fields via a combination of FM and NM gate structures on top of a 2DEG channel of a HEMT. Conduction electron will be spin polarized parallel to the edge magnetic fields. Recent experiments[147] which show large Zeeman splitting in GaInAs or InAs continue to lend credence to the viability of such spin current devices. Since external magnetic fields could be applied and eliminated with relative ease via switching the polarity of the local moment at the FM gate stripe, these devices hold promise for single transistor programmable logic and

memory.[126]

In fact the theoretical concept of field-induced spin current has been well accepted. What is outstanding now is taking the investigation further to include an accurate analysis of the spin current generation capability of these external field devices, where magnetic fields broaden continuously across the conduction channel, in contrast to previous approximation which considers the magnetic fields to approach the form of a Dirac delta function. The immediate impact of such broadening on electron transport is the conversion of the step function magnetic vector potential to one that is continuously increasing with conduction channel length. Living up to reality, it would be necessary to discretize the now more realistic barrier shape and apply the tight-binding GF approach to calculate spin current. The hitherto commonly used method – the single particle effective mass approximation with wave function and flux matching at the boundaries [Chap. 5]– relies on solving for the analytical form of the wave function, which could at times be formidable depending on the barrier shapes.

In mesoscopic transport, channel length has both physical and practical implications to device operation, its effect on the spin polarization of electron current would be crucial to our understanding of how best to use this device either as a constant spin current source or a tunable one. We will study both the effects of the channel length and the number of barriers on spin current. Room temperature distorts the ideal Fermi distribution in energy space, the adverse effect this has on spin current also warrants further investigation. The GF approach allows us to incorporate the Fermi level broadening due to thermal energy, and analyze the effect of temperature on spin current, an aspect which has been frequently neglected in previous works. Finally, we study the spin trans-

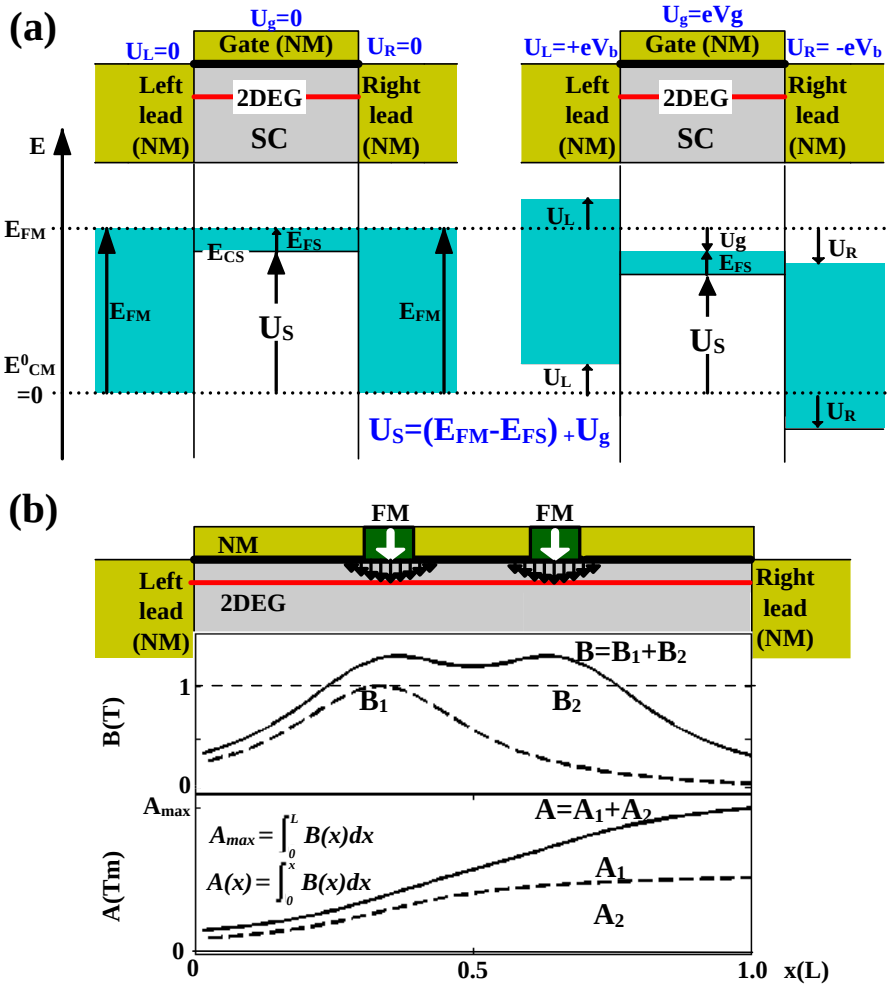

Figure 7.1: (a) Schematic illustration of the 2DEG-based field device and the band-diagram subject to external bias. (b) Distribution of magnetic fields and magnetic vector potential across the conduction channel. Ferromagnetic gates are etched and deposited into some parts of the gate stripes.

port at finite bias voltages, while previous works[148] have largely restricted their transport analysis to the Fermi level only.

7.2 Theory

Figure 7.1 shows a schematic diagram of the 2DEG system FM gates inserted between NM metals on top of the conduction channel. The specific periodicity of the FM gates

defines the types of field-barrier conduction channel that one intends for the electrons. Each of the FM is magnetized in the perpendicular direction. Application of an electric potential to the gates induces a change in the electrostatic potential barriers in the 2DEG channel, U_{eff}, as shown in Fig. 7.1. Note that the effective potential barrier in the channel, $U_{\text{eff}} = (E_{FM} - E_{FS}) + U_g$ depends on both the gate bias (U_g) as well as the Fermi energies of the lead (E_{FM}) and 2DEG (E_{FS}). The perpendicular magnetization of the FM gates produces a localized vertical magnetic field $B_z(x)$, which is modeled as a Lorentzian profile with a peak value of $1T$, i.e.

$$B_z(x) = \frac{B_0}{1 + (x - x_0)/\gamma} \tag{7.1}$$

where the peak magnetic field, $B_0 = 1T$ and the position of the peak is given by x_0. The spread of the magnetic field is characterized by γ, which is the half-width at the half-maximum of the distribution function. The corresponding magnetic vector potential is given by:

$$A(x) = \int B_z(x)\, dx = \frac{1}{2} + B_0\gamma \arctan\left(\frac{x - x_0}{\gamma}\right) \tag{7.2}$$

We apply the tight binding GF method as explained in Sec. 6.3 to compute the spin current, $I_{\uparrow,\downarrow}$ and spin dependent conductance, $G_{\uparrow,\downarrow}$ across the channel of device. The spin polarization of current is defined by the ratio $P = \frac{G_\uparrow - G_\downarrow}{G_\uparrow + G_\downarrow} = \frac{I_\uparrow - I_\downarrow}{I_\uparrow + I_\downarrow}$. In all our simulations, we considered a single-mode device, in which transmission occurs only at $k_y = 0$. Single-mode device[15,149] can be realized by constraining the transverse motion of electron, such that additional sub-bands corresponding to the y direction are formed. By considering transport of the lowest y sub-band, the device becomes single-mode and summation over k_y becomes unnecessary. A single-mode device can also be realized by designing a collector with small diameter into the drain and aligning the one-

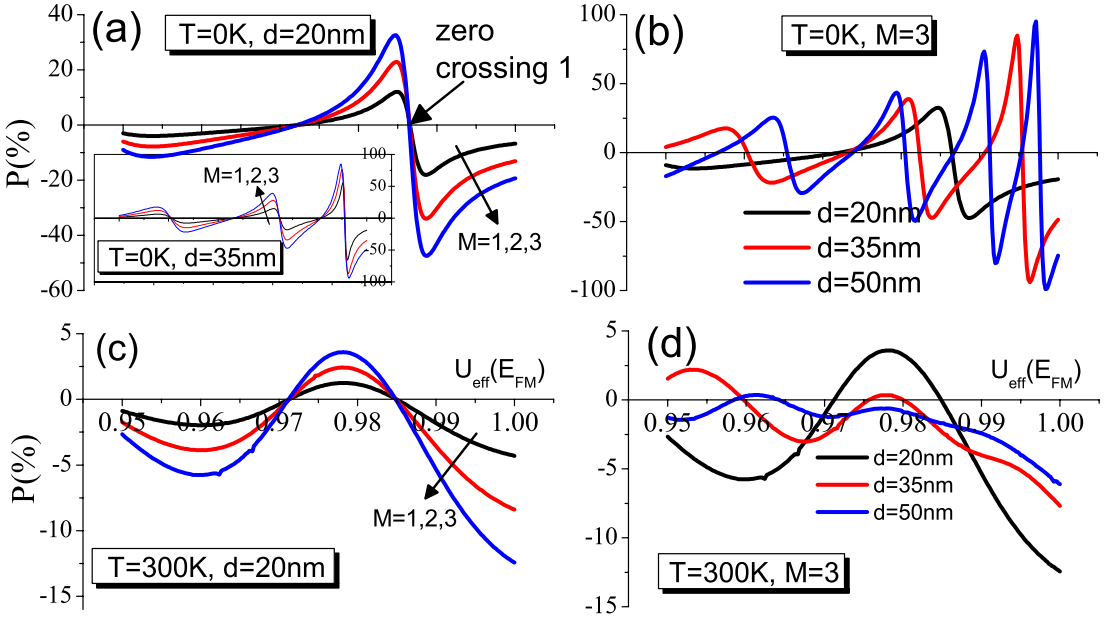

Figure 7.2: (a) Variation of spin polarization, P with increasing U_{eff} for a) different values of M at $T = 0K$, b) different values of d at $T = 0K$, c) different values of M at $T = 300K$, and d) different values of d at $T = 300K$.

dimensional probe parallel to current conduction path. If the diameter is small enough, it collects only electrons with $k_y = 0$.

7.3 Results and Discussion

Letting M represent the number of FM gates and d be the total channel length of the device, we carried out numerical calculations by assuming the following values, unless otherwise stated: $M = 3$, $d = 20nm$, Fermi level of the leads (2DEG), $E_{FM} = 5eV$ ($E_{FS} = 0.005eV$), temperature $T = 0K$, and source-drain bias, $V_b = 0$.

7.3.1 Effective Potential Barrier, U_{eff}

Based on the tight-binding model, we numerically calculate in Fig. 7.2. the spin polarization of current (P) in the 2DEG conduction channel as a function of the effective

potential barrier U_{eff}, taking into account the effects of channel length (d) and the number of barriers within d, i.e. M. Both M and d characterize the spin current conduction path. Fig. 7.2(a) and (b) show the variation of P with increasing U_{eff} at $T = 0K$, for different values of M and d. Previously, based on a simpler flux-continuity model which assumes a δ-function profile for the magnetic fields, it has been found that P is sensitive to U_{eff} across the conduction path. GF calculations confirm this oscillatory behavior of P with U_{eff}. As shown in Fig. 7.2(a) and (b), the oscillation of P increases in magnitude and frequency with increasing U_{eff}, especially as U_{eff} approaches the Fermi energy of the leads. This supports previous notion that this device could be used as a tunable source of spin current supply, for spin conductance in the device can be modulated by gate bias. The effect of modulation has been particularly sensitive when U_{eff} is close to the Fermi energy where electron transport occurs. This is especially so, given that the modulation of P exceeds $\pm 10\%$ for all values of M and d considered in Fig. 7.2(a) and (b), and can be converted to a measurable conductance change by well-established magneto-resistance techniques. At certain values of U_{eff} the spin polarization is zero, i.e. $P = 0\%$. By modulating the gate bias such that $P = 0\%$, the device can be utilized to function as a basic resistor without any spin polarizing effect.

7.3.2 Number of FM gates, M

It is reasonable to expect that the magnitude of the spin polarization should increase with the number of magnetic gates M for a fixed channel length d, and indeed, this trend is reflected in the numerical results of Fig. 7.2(a) where d is fixed at $20nm$. When $M = 1$, we attain a modulation of P of $\pm 10\%$ over a gate bias range ΔU_{eff} of $0.95 - 1.00eV$;

while for $M = 3$, the modulation in P reaches $\pm 30\%$ over ΔU_{eff} of $0.95 - 1.00eV$. However the frequency and the shape of the curves look similar with increasing M in that the zero-crossing $P = 0$ points for all three curves coincide, leaving only the curves between the fixed $P = 0$ points to vary in strength. In fact the region at around zero-crossing "1" is a useful zone for device operation as varying U_{eff} about this point changes P from positive to negative and vice versa.

7.3.3 Conduction channel length, d

The inset in Fig. 7.2 (a) shows the effect of M on the P for device with longer channel length, i.e. $d = 35nm$. It is worth noting that the effect of increasing M on the P curves of a device with $d = 35$ is similar to that with $d = 20nm$, except for the presence of more zero-crossing P points in the case of longer channel length. These results show that channel length affects the gate operating bias zone for conductance modulation but has little effect on the conductance modulation itself.

We will now investigate the effect of the conduction channel length d on P more thoroughly, while keeping the number of gates constant at $M = 3$. Figure 7.2 (b) shows the variation P for different channel length. Two major effects are observed with increasing channel length. Firstly, as in the case of increasing M, we notice an increase in the average magnitude of the P oscillations with increased d. The maximum amplitude of oscillation increases from $P = \pm 50\%$, $\pm 95\%$, to $\pm 100\%$ when d is increased from $d = 20nm$, $35nm$ to $50nm$, respectively. Secondly, unlike in the case of increasing M, we find a strong dependence of the frequency of the P oscillations on increased channel length. For instance within the range shown in the Fig. 7.2(b), we can notice one

peak when $d = 20nm$, three peaks when $d = 35nm$ and four peaks when $d = 50nm$. Higher frequency implies that a small change in the U_{eff} will cause multiple variations in P across various zero-crossings. The increase in the number of zero-crossing P points over U_{eff} offers a wider range for choosing the proper gate bias operating zone, but overly crowded zero-crossings within a small U_{eff} range implies operation instability. A small fluctuation of U_{eff} due to thermal of stray fields could cause sufficient unsolicited conductance modulation, sufficiently to destabilize the device.

In general, the increase in both d and M results in improved performance, in terms of higher spin polarization strength and/or greater range of zero-crossings for conductance modulation. However, in practical terms, it is not advantageous to increase these two parameters indefinitely. As discussed above, although a high frequency of P oscillations with U_{eff} is desirable for conductance modulation in a spin transistor, too high a frequency will be detrimental to device performance, since the device becomes sensitive to any small fluctuations in the gate bias. Indeed, if the device is to be used as a constant and not a tunable spin current source, it would be more advantageous for the gate oscillations in P to be minimal, so that the device can provide a stable supply of spin current. Besides, a short gate or device length is preferred for device miniaturization. Furthermore, our model assumes ballistic electron transport in the 2DEG channel, i.e. the optimal values of d and M would be constrained by the electron's MFP in the 2DEG.

7.3.4 Temperature T

All the above calculations have been carried out at $T = 0K$. For a more practical application we have also shown the results at room temperature, $T = 300K$. The results

are plotted in Fig. 7.2(c) and (d). As expected at room temperature the spin polarization is highly degraded. However, we still obtain significant spin polarization of $P > 10\%$ even at room temperature. The effect of M on P at room temperature [refer Fig. 7.2(c)] is similar to the effect of M on P at $T = 0K$. However channel length, d shows a very significant effect on P at room temperature. Indeed Fig. 7.2(d) shows that device with longer channel length is more sensitive to temperature change, and thus the performance degrades more significantly at room temperature. For example, the maximum value of P for the device with $d = 20nm$ drops only 30% (from $P = 50\%$ at $T = 0K$ to $P = 20\%$ at $T = 300K$), compared to a huge drop of 95% (from $P = 100\%$ at $T = 0K$ to $P = 5\%$ at $T = 300K$) for the device with $d = 50nm$. This shows that shorter devices are less susceptible to the detrimental effect of temperature change to P. The reason for such degradation is obvious as at higher temperature, the thermal broadening of the lead Fermi energy have a strong degradation effect on spin dependent transmission across the barriers, necessarily reducing spin current. The useful conclusions we can draw from these results is that while increasing M and d will increase P, the latter subjects the device to a more severe temperature degradation. The obvious pointers to device physicists are, for those who seek to improve P of a spin transistor, engineering more FM gates within a fixed channel length would be a more effective approach than increasing the channel length.

The effect of temperature has largely been neglected in previous studies which focused mainly on the theoretical concept of field-induced spin current. To study the temperature effect more thoroughly, we investigate the decrease of P with increasing temperature for different values of U_{eff} as shown in Fig. 7.3(a). In fact, the suppression of P due to temperature is also dependent on the applied gate bias. For example at

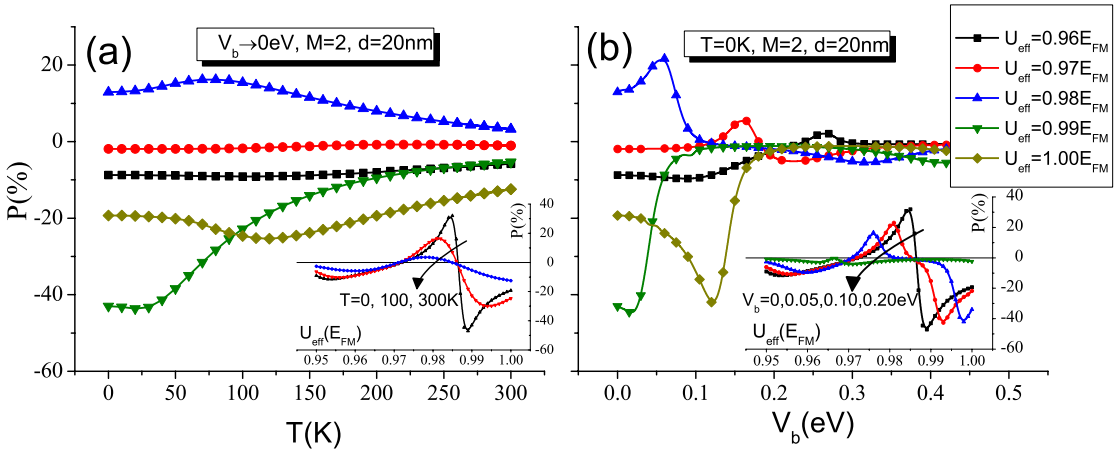

Figure 7.3: a) Spin polarization, P as a function of temperature, T at different values of U_{eff}. Inset in (a) shows P as a function of U_{eff}, at different T. b) P as a function of gate bias voltage, V_b at different values of U_{eff}. Inset in (b) shows spin polarization, P as a function of U_{eff}, at different V_b.

$U_{\text{eff}} = 0.99E_{FM}$, a very steep decrease in the magnitude of P with increasing temperature is noticed compared with other values of U_{eff}. The inset in Fig. 7.3(a) shows that the variation of P vs. U_{eff} is suppressed as temperature increases, clearly showing the degradation effect of temperature not only lowers average P but slows its variation with U_{eff}, thus lowering conductance modulation.

7.3.5 Bias Voltage V_b

In the above, we have investigated the effects of device geometry on the spin current in the limit of zero source-drain bias, i.e. $V_b \to 0$. In the following, we will study the effects of a finite applied bias voltage (V_b) on the spin polarization. To calculate the spin current for a finite V_b, we recall (6.29) with $\mu_{L(R)} = E_F + (-)eV_b/2$. The dependence of P on V_b is shown in Fig. 7.3(b). The main function of the source-drain bias, V_b is to provide a current drive through the device, whilst maintaining the device sensitivity to the gate bias. Therefore, for device stability, the variation in P with V_b should not be

too large, since the purpose of V_b is not to modulate the spin current. In the main plot of Fig. 7.3(b), we found the variation in P with V_b to be minimal for very low V_b, i.e. $V_b < 0.025eV$. For medium values of V_b, i.e. $0.025eV < V_b < 0.2eV$ the variation in P with V_b is relatively large. For larger source-drain bias, i.e. $V_b > 0.2eV$, the magnitude of P decreases to close to zero and its variation with V_b is also low compared to the region of medium V_b. It is quite clear now that medium V_b region is not suitable for device operation. Taking a closer look at the low V_b region reveals interestingly that P changes significantly with U_{eff}; in fact such trend is also observed in the medium V_b region. One can thus conclude that the low V_b region is ideal for spin transistor operation as it provides all the required features, namely high average P, sensitive P modulation by U_{eff}, and importantly insensitive P modulation by V_b. However, it is important to note that in a practical device, V_b has to be large enough to provide sufficient current drive through the device; optimization would thus be necessary here. In fact the inset in Fig. 7.3(b) shows non-heuristically that when V_b is low, P as well as its modulation with U_{eff} is generally higher. A closer inspection of the inset also shows that as V_b increases, there is a shift in the maximum value of P. For instance when V_b increases from $0V$, $0.05V$, to $0.1V$ the negative peaks of P shift from $U_{\text{eff}}(E_{FM}) = 0.988$, 0.992, to 0.997 respectively. It is important to note that although both positive and negative peaks shift, the zero-crossing remain pretty much fixed to $0.987eV$.

7.3.6 Magnetic Barrier Profile

In most of the previous studies of spin polarization under magnetic field, a δ-magnetic field was utilized. Here, we defined a more realistic barrier with Lorentz distribution.

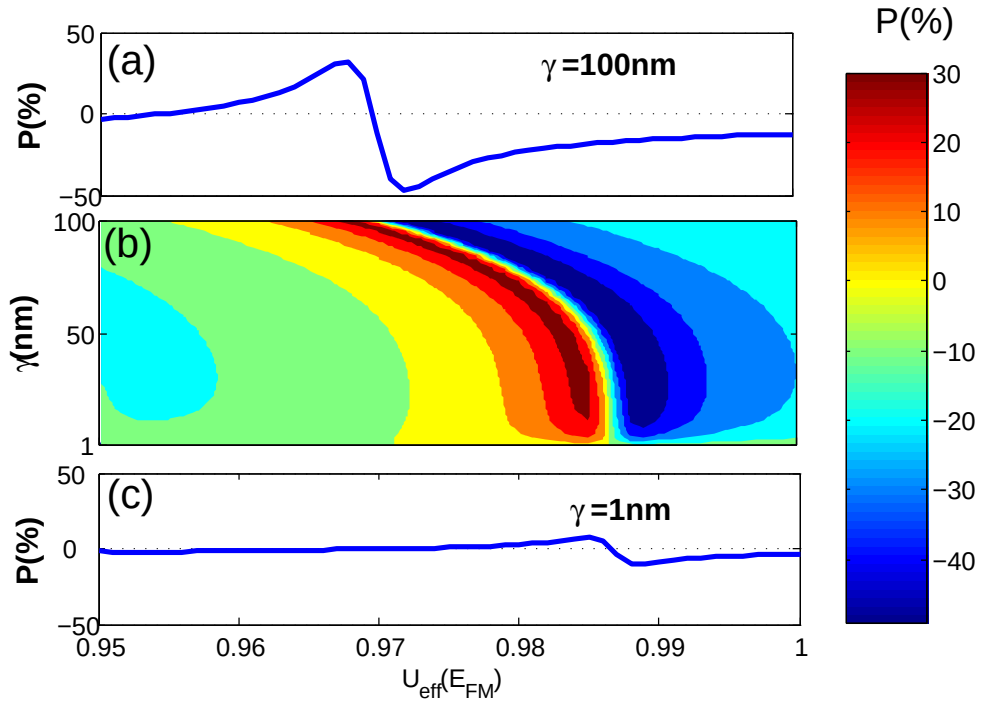

Figure 7.4: Spin polarization, P as a function of U_{eff} . (a) and (c) correspond to an magnetic field with $\gamma = 100nm$ and $1nm$, respectively. (b) shows P with increasing spread in magnetic field profile, γ.

In this more realistic distribution, the magnetic field spreads over a distance along x-axis. Therefore it is worth studying the effect of the spread on polarization of current in the device. In our simulation, this spread is characterized by a scalar parameter, γ. Figure 7.4 shows the variation of P for different γ. For all the values of γ's, the peak of the magnetic field is fixed at $1T$. As shown in the figure the maximum value of P increases with increasing γ for a fixed gate bias. This result which shows that spatially broadened field could generate higher spin polarization than focused field is an interesting finding, since it is more technologically easy to produce a magnetic field that spreads over a large distance, than producing a concentrated magnetic field.

The P peak also shifts towards the left as the γ increases. Knowing this trend, one can attempt to capture the P peak by lowering U_{eff} for higher γ. These results would

again be useful for device engineers to optimize the performance of a spin transistor at least for achieving high P.

7.4 Summary

We have applied the GF formulation described in the previous chapter to design a viable form of spin current transistor which passes electron through a series of wavy magnetic-electric barriers. We carried out a detailed simulations that take into consideration the field broadening effect, the anticipated temperature degradation of spin polarization, and calculated P, P variation with gate bias and source-drain bias, subject to important geometrical property of channel length as well as the number of FM gates within a fixed channel length. We concluded that increasing channel length or the number of FM gates within increases P; but raising the latter within a fixed channel length should be preferable as it does not exacerbate the temperature degradation of P, and is consistent with the trend of device minituarization. Another important conclusion of this work is that we have identified the low V_b region to be suitable for the operation of this spin transistor, as in this region, the device delivers high P, reasonably sensitive P variation with gate bias, and relatively insensitive P variation with source-drain bias. Last, results which show that broadened field is capable of generating higher P than spatially concentrated field is a rather jubilating finding for imparting broadened field to the device is technologically easier. In summary, our device could provide useful guidance to experimentalists or device engineers seeking to device a truly viable form of spin current transistor.

Chapter 8

Multiscale Spin Tunneling Theory

In the previous chapter, we have used GF method to study the spin transport across magnetic and electric barrier. In this chapter we integrate the two main spin transport models we have described earlier, i.e. 1) the microscopic GF formalism, and 2) macroscale SDD model, and develop a multiscale spin tunneling theory across FM/SC interface. This multiscale approach opens the possible for the detailed theoretical studies of interfacial properties (e.g. height, shape and spin asymmetry) required for achieving high SI via tunneling. Based on the calculated results, the optimal interfacial properties have been identified for possible experimental verification.[79]

8.1 Introduction

Electron propagation through potential barriers, which are induced either by interfacial roughness between adjacent layers, systematic doping of bulk layers with impurities, band alignment between different layer materials, or external potential applied locally, plays a crucial role in multilayer devices, e.g. SV sensors,[79,80,90,150,151] MTJ,[152,153] lateral spintronics devices[15,61,154,155] and traditional CMOS transistors. In fact, in semiconductor spintronic devices, the presence of tunneling barriers can greatly enhance SI efficiency from a FM electrode into the SC device.[36,37,41] Even in conventional ferromagnetic metal multilayers, spin-dependent scattering at the layer interfaces as opposed to scattering in the bulk, provides a significant contribution to the GMR effect.[14,156] Conversely, spin flip at the interfaces can result in a large suppression of MR.[157] More

recently, basic understanding of the ballistic tunneling process through barriers,[158] and rapid advances in nanofabrication techniques, have improved the capability of engineering interfacial barriers with significantly better performance.[159]

In this chapter, we develop a multiscale spin transport theory for the investigation of tunneling SI, which is an important phenomenon for spintronic applications. Spin current due to conduction electrons is a non-conserved quantity, and thus the efficiency with which it is transmitted from a magnetic source layer to a usually non-magnetic collector layer, is crucially determined by the physics of the electron propagation and transmission through the interfacial barrier. Therefore, the SI process warrants a detailed analysis beyond the conventional macroscopic picture. Previous theoretical investigations of SI across a tunnel barrier are either based on the purely semiclassical SDD approach [Sec. 2.2] (which treats the barrier as a lump resistance element), or by focusing on the ballistic tunneling across the barrier region [Chap.6].

Here, we apply the effective mass GF formalism [refer Sec. 6.3] to analyze the microscopic effects of the tunnel barrier potential on the incident spin-current. At the same time, the transmitted spin current is also dependent on the spin accumulation and resulting electrochemical potential at the two adjacent contacts. The spin accumulation on the contacts can be determined by considering the semi-classical SDD transport [Sec. 2.2] within the bulk of the contacts.[25,35,36] Thus, the main focus of this chapter is to 1) introduce a self-consistent approach that combines the microscopic GF formalism within the nano-scale barrier and the SDD model within the macroscopic contacts, and 2) based on this model, study the effects of barrier properties, e.g. potential profile and geometry, on the tunneling transport, in order to optimize the tunneling SI for potential

spintronic applications.

In the self-consistent approach, the nonequilibrium potentials at the leads are coupled to the GF calculation for transport within the barrier. One consequence of this self-consistent approach is that the effective barrier resistance as seen by the spin-up and down electrons becomes a dynamical quantity which depends on external factors such as the applied bias, instead of a static parameter which is solely dependent on the intrinsic barrier properties. The resulting SI efficiency in the multilayer will be a function of external parameters, e.g. the applied voltage bias or current density,[160,161] in agreement with recent experimental observations. Thus, our model can incorporate spin transport effects that may have been neglected by previous models. The analysis of these effects such as the increase in spin asymmetry of tunneling conductance with increasing barrier height and barrier spin asymmetry, may potentially guide experimental efforts to engineer interfacial barriers for optimal SI.

8.2 Model and Theory

8.2.1 Self-consistent Model

The basic structure under consideration [Fig. 8.1] is a multilayer device comprising a bulk FM left layer acting as the spin injector, a thin interface, and the bulk SC right layer, which receives the injected spin current. The interfacial barrier is located within the SC region. At equilibrium, the Fermi levels of the SC and FM layers are equalized, but under an applied electrical bias, a non-equilibrium electrochemical profile is obtained, typically as shown in Fig. 8.1 (top). Note that in both the FM and SC layers, there

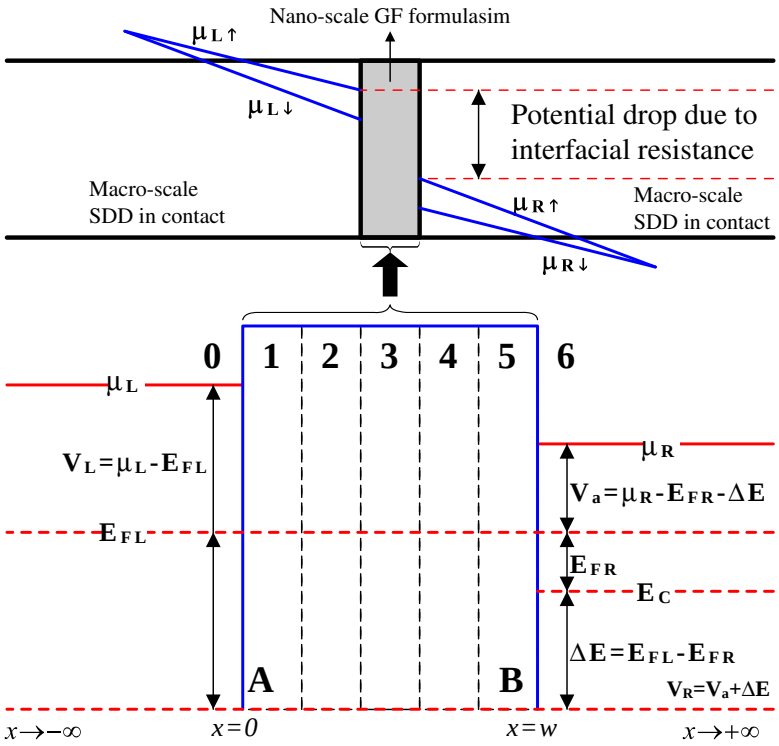

Figure 8.1: (Top) Non-equilibrium distribution of electrochemical potential across the multilayer structure under electrical bias. (Bottom) Magnified diagram of the interfacial barrier of thickness $w = 2.5nm$, which is spatially discretized into $n = 5$ planar sections for the GF analysis. $\mu_L(\mu_R)$ indicates the spin-up electrochemical potential at the boundaries of the barrier, i.e. at A and B. $E_{FL}(E_{FR})$ is the equilibrium Fermi level of the left(right) contacts. E_C indictaes the conductacne band of the seiconductor. For clarity, only the spin-up potentials are drawn.

will be a split in the spin-up and down electrochemical potentials in the vicinity of the interfacial barrier, resulting in spin accumulation.

In most previous works utilizing GF analysis, the electrochemical potentials adjacent to the barrier on both sides are treated as a reservoir constant, i.e. independent of the nature of electron propagation within the barrier. Whilst in the bulk SDD approach, electron transport in the magnetic multilayers has been modeled based on purely passive factors, such as device geometry, resistivity and the different spin diffusion lengths in its constituent layers. In our self-consistent, multiscale approach, however, the spin-dependent electrochemical potentials and the tunneling resistance across the barrier are solved self-consistently by combining the microscopic GF model within the barrier and

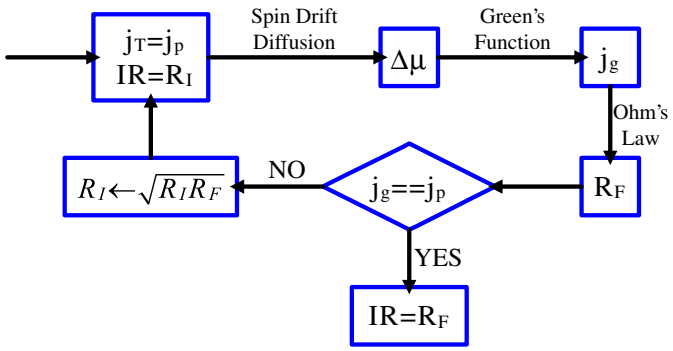

Figure 8.2: Self-consistent calculation scheme for interfacial resistance and current density, which is iterated until the current density converges.The calculation begins by assuming initial values of the charge current density ($j_p = j_p + j_p$) and interface resistance (R_I). Based on the SDD equations, the spatial distribution of the electrochemical profile within both the FM and SC leads can be determined. Subsequently, the evaluated electrochemical potential values at sites immediately adjacent to the barrier are input as variables in the GF calculation of electron transmission through the barrier. The microscopic model within the barrier constitutes a parallel scheme to determine the current density (j_g) and the interfacial resistance (R_F). The calculation cycle is repeated until the current densities j_p and j_g, and hence the corresponding interfacial resistances R_I and R_F converge.

the SDD model in the contacts, as illustrated schematically in Fig. 8.2.

In this self-consistent calculation scheme the interfacial resistance and current density is iterated until the current density converges. In this way, we have unified the microscopic GF and macroscopic SDD models within and outside the barrier, respectively, and obtain the effective tunneling resistance value which is consistent with both models. Thus, the nonequilibrium potentials at the leads are coupled to the GF calculation for transport within the barrier.

8.2.2 Green's Function (GF) formalism

The interfacial central region of the three-region device of Fig. 8.1, of thickness $w = 2.5$ nm, is discretized into n planar sections. The number of discrete sections is chosen to be $n = 5$ such that the width of each section $a = w/n = 0.5nm$ is smaller than the Fermi wavevector $\lambda_F \approx 1.5nm$ thus ensuring accuracy of the tight-binding GF

calculations. The left FM and the right SC regions are both treated as semi-infinite in width. Throughout this chapter, the superscript R(A) refers to retarded and advance function, and the subscript L(R) refers to the function at left(right)contact. Following the tight-binding lattice formalism [Sec. 6.3], the retarded GF matrix for the interfacial region can be expressed by $G^R = \left(E - H_C - \Sigma_L^R - \Sigma_R^R\right)^{-1}$, where Σ_L^R and Σ_R^R are the (5×5) self-energy matrices, due to adjacent sites on the contacts to the left and right of the central region. The explicit form of G^R for the present model is given by:

$$G^R = \begin{bmatrix} E - H_{C1} - t_L g_0 t_L & t & 0 & 0 & 0 \\ t & E - H_{C2} & t & 0 & 0 \\ 0 & t & E - H_{C3} & t & 0 \\ 0 & 0 & t & E - H_{C4} & t \\ 0 & 0 & 0 & t & E - H_{C5} - t_R g_6 t_R \end{bmatrix}^{-1} \tag{8.1}$$

where $H_{Cj} = (2t + U_j)$ for $j = 1, \ldots, 5$, with U_j being the localized potential at lattice site j, $t = \hbar^2/2ma^2$ i.e. the energy coupling constant between adjacent discrete sites, and a is the distance between them. Equation (8.1) is derived from (6.27). Since, in the present model, there is no external magnetic field, (8.1) is obtained by setting the magnetic field and vector potential terms in (6.27) to zero.

Before the inverse matrix of (8.1) can be evaluated, we require the explicit expression for the self-energies of $t_L g_0 t_L$ and $t_R g_6 t_R$. In the one-dimensional single mode form, as an approximation, the flat-potential analytic GF for the semi-infinite left and right leads is given by $g_{0(6)} = -(1/t)\exp\left(ik_{L(R)}a\right)$, where $k_{L(R)} = \sqrt{2m\left(E - V_{L(R)}\right)/\hbar} = \sqrt{2m\left(E - \mu_{L(R)} + E_{FL(R)}\right)/\hbar}$, with $E_{FL(R)}$ the equilibrium Fermi level of the left(right) contacts, and $\mu_{L(R)}$ the non-equilibrium electrochemical potential incident on the left/right

side of the barrier. V_R is the energy quantity as described in Fig. 8.1. To calculate the current perpendicular to the multilayer plane at a particular site, we consider the ballistic spin current expression of (8.2) which could be obtained from (6.29),

$$J_\sigma = \sum_{k_{//}} \frac{-e}{A\hbar} \int \frac{dE}{2\pi} (f_{L\sigma} - f_{R\sigma}) Trace \left[\Gamma_{L\sigma} G^R_\sigma \Gamma_{L\sigma} G^A_\sigma\right] \tag{8.2}$$

where A is the device cross sectional area, σ is the index for spin up($\uparrow$)/down($\downarrow$) and $f^\sigma_{L,R} = 1/\left[1 + \exp\left(E - \mu^\sigma_{L,R}\right)/kT\right]$ is the Fermi occupation probability. Since the non-equilibirum GF applies only to the interfacial potential in the SC region, and assuming that the SC material has a uniform effective mass over the transverse x-y plane, $\mathrm{T}(E) = Trace\left[\Gamma_{L\sigma} G^R_\sigma \Gamma_{L\sigma} G^A_\sigma\right]$ will be independent of $k_{//}$. Thus current can be calculated as:

$$J^\sigma_0 = \frac{-e}{\hbar} \int \frac{dk_{//}}{4\pi^2} \int \frac{dE}{2\pi} (f^\sigma_L - f^\sigma_R)\, \mathrm{T}(E) \tag{8.3}$$

The final current expression is:

$$J^\sigma_0 = \frac{-2\pi mekT}{h^3} \int_{-\infty}^{+\infty} dE \mathrm{T}(E) (F^\sigma_L - F^\sigma_R) \tag{8.4}$$

where $F^\sigma_{L,R} = \ln\left[1 + \exp\left(\mu^\sigma_{L,R} - E\right)/kT\right]$.

8.2.3 Boltzmann spin-drift-diffusive (SDD) model

The GF calculations described in the previous section require the electrochemical potential values of μ_0, $\mu_\uparrow$ and $\mu_\downarrow$ at the left/right boundaries between the central region and the semi-infinite FM/SC contacts. These have to be determined by evaluating the electrochemical potential profile within the bulk FM and SC leads using the macroscopic SDD theory [(2.3)]. The potential discontinuity at the interface due to the interfacial resistance is described by the following equation: $-eJ^\sigma_0 R^\sigma_I = \mu^\sigma_R - \mu^\sigma_L$, where $R^\sigma_I$is the areal spin dependent interfacial resistance experienced by electrons at interface.

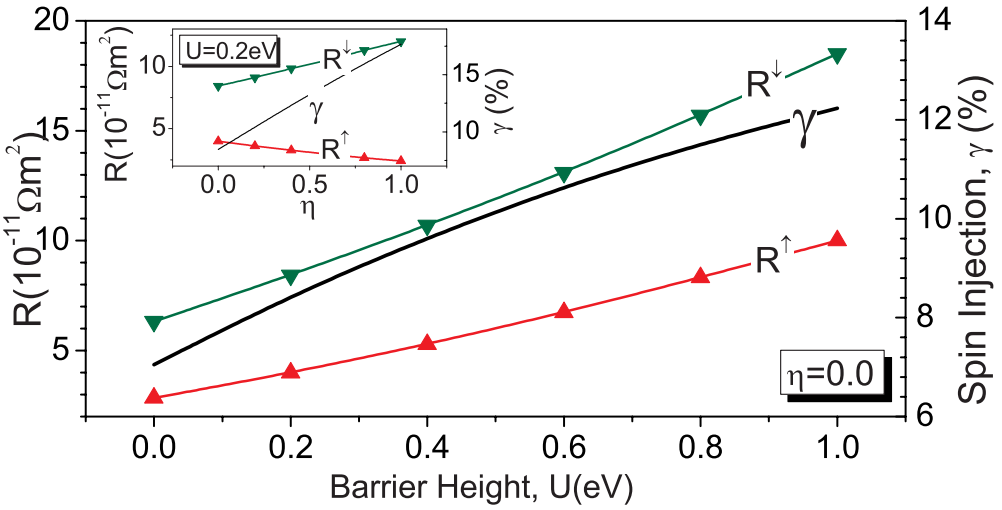

Figure 8.3: Left axis: Spin-up and down resistances as a function of interfacial barrier height U. The difference of resistances becomes increasingly more divergent with U. Right axis: Tunneling spin injection ratio γ increases with U due to the increasingly spin asymmetric resistances. Inset: Spin-up and down resistances (left axis) and spin injection ratio (right axis) as a function of spin asymmetry η of barrier potential, with $U_\uparrow$ fixed at $0.2eV$.

The electrochemical potential $\mu^\sigma_{R,L}$ at the interfaces and R^σ_I are solved self-consistently by combining the microscopic GF model within the barrier and the Boltzmann SDD model in the contacts, as illustrated schematically in Fig. 8.2.

8.3 Results and Discussion

Based on the above self-consistent scheme, we calculate the resistances $R_\uparrow$ and $R_\downarrow$ as experienced by the spin-up and down electrons, respectively, and the SI ratio, defined as $\gamma = (j_\uparrow - j_\downarrow)/(j_\uparrow + j_\downarrow)$ at $x = w$. Unless otherwise stated, we assume the following parameter values in our calculations:[2,3,162,163] $j = 10^6 A/cm^2$, resistivity $(\rho_{FM}, \rho_{SC}) = (10^{-7}, 10^{-4})\Omega m$, intrinsic spin polarization ratio $(\alpha_{FM}, \alpha_{SC}) = (0.4, 0.0)$, effective mass $(m^*_{FM}, m^*_{SC}) = (1, 0.067)m_e$, and Fermi energy $(E_{FM}, E_{FS}) = (10, 0.05)eV$.

Figure 8.3 shows that both the magnitude $(R_\uparrow + R_\downarrow)$ and spin asymmetry $(R_\uparrow - R_\downarrow)$

of the interfacial barrier resistance increases with interfacial barrier height U, even when the barrier height is spin-independent (i.e. $\eta = 0$). While the former is a well-established fact, the latter is a rather unexpected result arising out of the self-consistent, multi-scale calculations. This is because the semiclassical SDD models predict high SI only in the presence of spin-asymmetric tunnel barriers.[36] The divergence between the $R_\uparrow$ and $R_\downarrow$ with increasing barrier height naturally leads to a higher SI ratio, as by the γ curve of Fig. 8.3. Additionally, as shown in the inset of Fig. 8.3, the divergence between the spin-up and down resistances also increases with increasing spin asymmetry $\eta = (U_\downarrow - U_\uparrow)/(U_\uparrow + U_\downarrow)$ of the barrier potential, thus enhancing the SI ratio through the barrier.

It is worth noting that the increase of SI ratio with increasingly divergent spin resistance is consistent with previous theoretical results.[36] Since it has been previously predicted that SI efficiency may be improved by increasing the spin asymmetry of the tunneling barrier potential, considerable experimental efforts have been focused on engineering suitable tunneling barrier with a large spin-split property. Our calculations, however, suggest that high SI efficiency may also be achieved by engineering a suitably high barrier potential, without necessarily having to enhance its spin-split property, which is a more challenging proposition in practical tunnel barriers. Thus, the fact that the spin asymmetry of barrier resistance is sensitive to the barrier height is a useful result of our work. Further, it is instructive to conduct a systematic study of how the divergence between the spin-up and down resistances is influenced by specific tunnel barrier profiles and thickness.

We consider three types of barrier potentials: 1) exponentially increasing (in go-

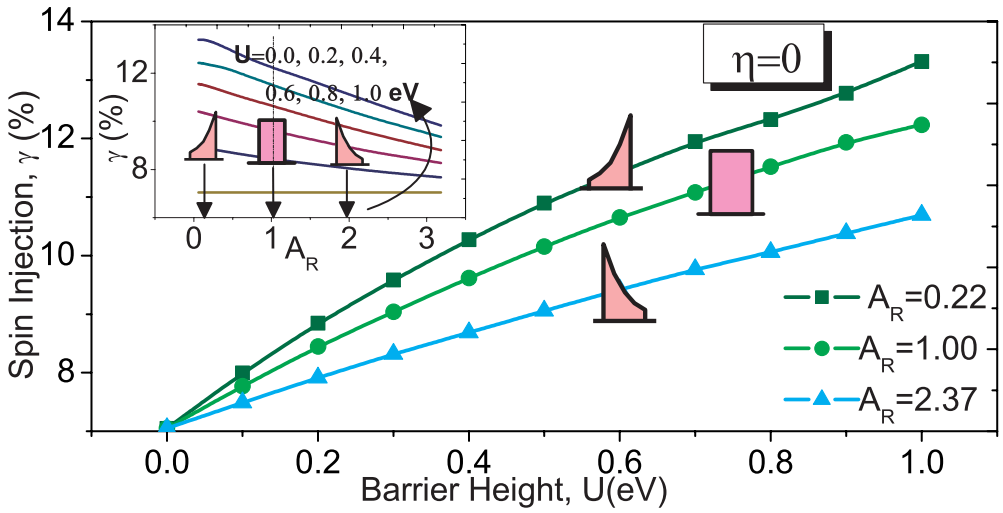

Figure 8.4: Spin injection ratio γ as a function of barrier height U and barrier geometry as characterized by A_R. The barriers considered have zero spin-asymmetry ($\eta = 0$) and the same area under their respective potential curve.

ing from the FM to the SC layer), 2) exponentially decreasing and 3) square profiles. These barrier profiles are visually depicted in the inset of Fig. 8.4. For a quantitative description of the barrier profile, we introduce a variable $A_R = (U_0/U)$, which is the ratio of the barrier potential at $x = 0$ (U_0) to the height of an equivalent square barrier (U). Barriers of the same thickness w can be considered equivalent when the area under their respective barrier potentials are equal. This is because for barriers with identical w, the area under the barrier represents the average potential experienced by the tunneling electron while traversing across the barrier. By keeping the area under the barrier constant, we thus have $A_R < 1$ $(A_R > 1)$for the exponentially increasing (decreasing) potentials, and $A_R = 1$ for the square barrier.

We first consider the effect of barrier height for three representative barrier potentials with specific A_R values of 0.22, 1.0 and 2.37, respectively. For all three barrier shapes, the SI ratio increases monotonically with the barrier height U, but to a varying extent depending on the barrier geometry (Fig. 8.4). Barriers with an exponentially de-

creasing (increasing) slope exhibit the least (greatest) sensitivity to increase in barrier height. Next, we analyze the effect of barrier geometry (i.e. A_R) on spin injection. As seen from the inset of Fig. 8.4, there is a substantial decrease in the SI ratio with increasing A_R. This is because the effective tunneling resistance of an exponentially decreasing barrier (i.e. with $A_R > 1$) is lower than that of an exponentially increasing barrier (with $A_R < 1$). This translates to a lower SI efficiency, since (as shown in Fig. 8.3) SI generally increases with increasing resistance of the interfacial barrier. While a higher U improves the SI ratio γ, the rate of increase in γ is suppressed at large A_R values. It should be noted that barriers with $A_R \approx 2$ have a profile similar to that of a Schottky barrier. Thus, our analysis indicates that a Schottky effect at a FM/SC interface is detrimental to achieving high SI efficiency, compared to the more square-like insulating (e.g. oxide) barrier potential of the same tunneling resistance.

8.4 Summary

We integrated the two spin transport models that we have described previously – SDD and GF – and developed a multiscale spin tunneling theory to study the tunneling SI process through FM/SC interfacial barrier by means of a self-consistent analysis. The calculated results show that SI efficiency increases with barrier height, as well as barrier asymmetry. The former trend is not obvious and has not been formally predicted previously. Our model also predicts a strong dependence of the SI ratio on the barrier profile. In general, an exponentially increasing interfacial barrier between a FM metal and a SC contact yields a higher ratio compared to a Schottky-like exponentially decreasing barrier. This suggests that a pronounced Schottky effect should be avoided in

order to achieve a high SI ratio. Our calculated results provide a guide to the engineering (e.g. via doping) and biasing of interfacial barriers in order to obtain the optimal barrier height and profile for tunneling SI.

Chapter 9

Conclusion

9.1 Conclusion

In this thesis, first, we developed a mathematical model to describe the spin transport in a PSV device. Using this model, we analyzed the effect of material parameters on the MR of the PSV. In our analysis we focused mainly on understanding the physics of spin transport as well as optimizing the material parameters to achieve high MR ratio. We discover various novel effects which are further utilized to enhance the MR ratio. Then, we studied the optimization of MR by including additional resistive components–IR and additional layers–into the basic PSV device. In both cases, we found that there is a competition between all the individual resistive components in dominating the spin asymmetry of the device. We also analyzed the interplay between this competitive resistance effect and spin-relaxation for further optimization of the MR. Then, we studied the current confinement effect which rises due to the effect of patterning the layers in a SV device. The current confinement effect further complicates the competitive resistance effect due to other phenomenon such as current crowding and spreading resistance. To optimize the MR, all these effects were considered. We showed that device performance

can be highly enhanced by carefully utilizing these effects.

Then, we studied electron and spin transport across a ballistic channel in a 2DEG spin transistor. We found that the transport properties of the device, such as the transmission probability, the SI efficiency and the MR ratio, all exhibit oscillatory behavior when the electron energy is varied. The basis of these oscillations is the resonant transport across the 2DEG. By utilizing this resonant transport property, we further proposed a SC-based gate controlled MR device that could perform the function of a metallic SV, but with the advantage that its MR can be optimized (post-fabrication) and its stability enhanced by controlling a gate bias voltage. Next, we modified the spin transistor by designing a viable form of spin transistor in which electron passes through a series of wavy magnetic-electric barriers. We carried out a detailed simulations that take into consideration the field broadening effect, the temperature degradation of spin polarization, and calculated SI, SI variation with gate bias and source-drain bias, subject to important geometrical property of channel length as well as the number of FM gates within a fixed channel length. This device provided useful guidance to experimentalists or device engineers seeking to device a truly viable form of spin current transistor.

Finally, we combined the two main mathematical models that we have developed in this thesis–SDD and GF–and developed a multiscale theory to study the tunneling SI process through an interfacial barrier by means of a self-consistent analysis. The calculated results enable us to carry out MR optimization by utilizing the interfacial properties such as barrier profile and barrier spin-asymmetry. Based on the calculated results, the optimal interfacial properties have been identified for possible experimental verification.

In summary, in this thesis we have successfully achieved the 3 main objectives:

1. We have developed mathematical models to describe the physics of spin transport in spintronic nanodevices. The two main mathematical models that were developed in this thesis are, i.e.1) semi-classical SDD model, and 2)the mesoscopic GF formalism.

2. Using these models, we have studied the effects of various device parameters on spin transport. Via our studies, we have understood the physics of spin transport, as well as identified various anomalous and novel effects. The spin transport physics/effect that were noticed and/or studied are:

   - The effect of structural and physical parameters.
   - The effect of spin-independent resistivity on spin-asymmetry.
   - Anomalous MR suppression effect due to the coupling of spin relaxation with resistivity.
   - The complex interplay between spin-asymmetry, spin relaxation and the anomalous MR suppression effect due to increase in FM layer thickness.
   - competitive resistance effect due to interfacial resistance and additional layers.
   - Current confinement, current crowding and spread resistance due to patterning of layers.
   - Resonant spin tunnelling in ballistic regime.
   - Gate controlled MR in spin-transistors.
   - Ballistic spin tunneling across magnetic-electric barriers.
   - Effect of interfacial barrier geometry and shape.

3. By careful utilization of the results and theoretical knowledge obtained from our analysis, we further explored different means as well as proposed new designs to enhance the performance of spintronic devices.

Our results, models and the simulation programs that have been developed to model spin transport are also useful for the experimentalist to predict the device performance prior

to conducting experiments and practical realization.

9.2 Further work

The GF formulism introduced in this thesis is a very powerful tool to study the quantum transport phenomena in nanodevices. Thus by using the GF method, we can continue to study many other spin transport phenomena, which could be useful in optimizing the performance of spintronic devices. In the future I will use the NEGF method to study physics of electron transport in 1D materials, especially in graphene nanoribbons (GNR). The GNR is a quasi-one dimensional system which has attracted various interesting studies on transport,[164–166] magnetic,[167–173] and optical[172,173] properties. I will develop a mathematical model based on the pi-orbital tight binding (TB) method [4] to describe the electron transport in GNR. Using this model, I will investigate the effects of atomic disorder on the electronic transport in graphene. The effect of applied magnetic field in a disordered graphene will also be investigated. I will further

1. include other physical phenomena such as spin scattering and phonon scattering into the existing model;
2. model different structure such as shaped modified GNR and bilayer GNR; and investigating their effects on the electronic transport.

My aim is to gain a clear understanding of these phenomena and further utilize the effects in device application, e.g. in magnetoresistive devices.

Appendix A

Mathematica Code for Spin Drift Diffusion Model

Appendix B

ANSYS Software Package for Finite Element Poison Solver

Appendix C

Matlab Code for Green's Function Formulation

Bibliography

[1] L. Piraux, S. Dubois, and A. Fert, J. Magn. Magn. Mater. 159,L287 (1996).

[2] J. Bass and W. P. Pratt, Jr., J. Magn. Magn. Mater. 200, 274, (1999).

[3] N. Strelkov, A. Vedyaev, B. Dieny, J. Appl. Phys. 94, 3278 (2003).

[4] S. A. Wolf, D. D. Awschalom, R. A. Buhrman, J. M. Daughton, S. von Molnar, M. L. Roukes, A. Y. Chtchelkanova, and D. M. Treger, Science 294, 1488 (2001).

[5] I. Zutic,J. Fabian,and S. Das Sarma, Rev. Mod. Phys. 76, 323 (2004).

[6] G. Prinz, Science 282, 1660 (1998).

[7] G. Prinz and K. Hathaway, Physics Today 48, 24 (1995).

[8] S. Das Sarma, American Scientist 89, 516 (2001).

[9] Gregg, JF and Petej, I and Jouguelet, E and Dennis, C, J. Phys.D 35, R121 (2002).

[10] Tedrow, P. M., R. Meservey, and P. Fulde, Phys. Rev. Lett. 25, 12701272 (1970).

[11] Julliere, M., Phys. Lett. A 54, 225226(1975).

[12] Johnson, Mark and Silsbee, R. H., Phys. Rev. Lett. 55, 1790–1793 (1985).

[13] M. N. Baibich, J. M. Broto, A. Fert, F. Nguyen Van Dau, F. Petroff, P. Etienne, G. Creuzet, A. Friederich and J. Chazelas, Phys. Rev. Lett. 61, 2472 (1988).

[14] G. Binasch, P. Grunberg, F. Saurenbach and W. Zinn, Phys. Rev. B 39, 4828 (1989).

[15] S. Datta and B. Das, Appl. Phys. Lett. 56, 665 (1990).

[16] Schliemann, John and Egues, J. Carlos and Loss, Daniel, Phys. Rev. Lett. 90, 146801 (2003).

[17] Johnston-Halperin, E. and Lofgreen, D. and Kawakami, R. K. and Young, D. K. and Coldren, L. and Gossard, A. C. and Awschalom, D. D., Phys. Rev. B 65, 041306 (2002).

[18] M. E. Flatté. and G. Vignale, Appl. Phys. Lett. 78, 1273 (2001).

[19] Francesco Giazotto and Fabio Taddei and Rosario Fazio and Fabio Beltram, Appl. Phys. Lett. 82, 2449-2451 (2003).

[20] T. Koga, J. Nitta, S. Datta and H. Takayanagi, Phys. Rev. Lett. 88, 126601 (2002).

[21] A. Slobodskyy, C. Gould, T. Slobodskyy, C. R. Becker, G. Schmidt, and L.W. Molenkamp, Phys. Rev. Lett. 90, 246601 (2003).

[22] N. F. Mott, Proc. Roy. Soc. 153, 699 (1936).

[23] N. F. Mott, Proc. Roy. Soc. 156, 368 (1936).

[24] Aronov, A. G., Zh. Eksp. Teor. Fiz. Pisma Red. 22,37–39(1976).

[25] P.C. van Son, H. van Kempen and P.Wyder, Phys. Rev. Lett. 58, 2271 (1987).).

[26] T.Valet and A.Fert, Phys. Rev. B 48, 7099 (1993).).

[27] D. Hagele, M. Oestreich, W.W. Ruhle, N. Nestle, K. Eberl, Appl. Phys. Lett. 73, 1580 (1998).

[28] J.M. Kikkawa, D.D. Awschalom, Nature 397, 139 (1999).

[29] Ohno, Y., D. K. Young, B. Beschoten, F. Matsukura,H. Ohno, and D. D. Awschalom, Nature 402, 790 (1999).

[30] H. Ohno, D. Chiba, F. Matsukura, T. Omiya, E. Abe, T. Dietl, Y. Ohno and K. Ohtani, Nature 408, 944 (2000).

[31] M. Yamanouchi, D. Chiba, F. Matsukura, and H. Ohno, Nature 428, 539 (2004).

[32] M. Yamanouchi, D. Chiba, F. Matsukura, T. Dietl, H. Ohno, Phys. Rev. Lett. 96, 096601 (2006).

[33] F.G. Monzon and M.L. Roukes, Phys. Rev. Lett. 198, 632 (1999).

[34] M. Khodas, A. Shekhter and A.M. Finkel'stein, Phys. Rev. Lett. 92, 086602 (2004).

[35] G. Schmidt, D. Ferrand, L. W. Molenkamp, A. T.Filip and B. J. van Wees, Phys. Rev. B 62 R4790 (2000).).

[36] E.I. Rashba, Phys. Rev. B 62, R16267,(2000).).

[37] A. Fert and H. Jaffres, Phys. Rev. B 64, 184420 (2001).

[38] P. R. Hammar, B. R. Bennett, M. J. Yang, and Mark Johnson, Phys. Rev. Lett. 83, 203 (1999).

[39] S. Gardelis, C. G. Smith, C. H. W. Barnes, E. H. Linfield, and D. A. Ritchie, Phys. Rev. B 60, 7764 (1999).).

[40] B. T. Jonker, Proc. IEEE 91, 727 (2003).

[41] H. J. Zhu, M. Ramsteiner, H. Kostial, M. Wassermeier, H. P. Schonherr, and K. H. Ploog, Phys. Rev. Lett. 87, 016601 (2001).).

[42] R. Fiederling, M. Keim, G. Reuscher, W. Ossau, G. Schmidt, A. Waag and L.W. Molenkamp, Nature (London) 402 (1999), p. 787.

[43] Lampel, G., Phys. Rev. Lett. 20, 491493 (1968).

[44] Bhat, R. D. R., and J. E. Sipe, Phys. Rev. Lett. 85, 54325435 (2000).

[45] Albrecht, J. D. and Smith, D. L., Phys. Rev. B 66, 113303 (2002).

[46] Albrecht, J. D. and Smith, D. L., Phys. Rev. B 68, 035340 (2003).

[47] Alvarado, Santos F. and Renaud, Philippe, Phys. Rev. Lett. 68, 1387–1390 (1992).

[48] Kirczenow, George, Phys. Rev. B 63, 054422 (2001).

[49] Grundler, Dirk, Phys. Rev. B 63, 161307 (2001).

[50] Fabian, J., and S. Das Sarma, J. Vac. Sci. Technol. B 17, 17081715 (1999).

[51] R. J. Elliott, Phys. Rev. B 96, 266 (1954); Y. Yafet, Sol. State Phys. 14, 2 (1963).).

[52] Dyakonov, M. I., and V. I. Perel, Fiz. Tverd. Tela 13, 35813585 (1971).

[53] Bir, G. L., A. G. Aronov, and G. E. Pikus, Zh. Eksp. Teor. Fiz. 69, 13821397 (1975).

[54] Dyakonov, M. I., and V. I. Perel, Zh. Eksp. Teor. Fiz 38, 362376 (1973).

[55] Rashba, E. I., and A. L. Efros, Phys. Rev. Lett. 91, 126405 (2003).

[56] D K Young and J A Gupta and E Johnston-Halperin and R Epstein and Y Kato and D D Awschalom, Semiconductor Science and Technology 17, 275-284(2002).

[57] Chiba, D., M. Yamanouchi, F. Matsukura, and H. Ohno, Science 301, 943945 (2003).

[58] Kato, Y., R. C. Myers, D. C. Driscoll, A. C. Gossard, J. Levy, and D. D. Awschalom, Science 299, 12011204 (2003).

[59] Waag, A., T. Gruber, G. Reuscher, R. F. W. Ossau, G. Schmidt, and L. W. Molenkamp, J. Supercond. 14, 291298 (2001).

[60] G. Papp and F. M. Peeters, Appl. Phys. Lett. 78, 2184-2186 (2001).

[61] S. G. Tan, M. B. A. Jalil, T. Liew, Phys. Rev. B 72, 205337 (2005).).

[62] T Hartenstein and C Li and G Lefkidis and W Hü), Journal of Physics D: Applied Physics 41, 164006 (2008)).

[63] Mattana, R., J.-M. George, H. Jaffres, F. Nguyen Van Dau, A. Fert, B. Lepine, A. Guivarch, and G. Jezequel, Phys. Rev. Lett. 90, 16601(2003).

[64] Fiederling, R., M. Kleim, G. Reuscher,W. Ossau, G. Schmidt, A. Waag, and L. W. Molenkamp, Nature 402, 7877905(1999).

[65] Weisbuch, C., and C. Hermann, Phys. Rev. B 15, 816822 (1977).

[66] Y. Q. Li and D. W. Steuerman and J. Berezovsky and D. S. Seferos and G. C. Bazan and D. D. Awschalom, Appl. Phys. Lett. 88, 193126 (2006).

[67] D. Yoshizumi, Y. Muraoka, Y. Okamoto, Y. Kiuchi, J. Yamaura, M. Mochizuki, M. Ogata, and Z. Hiroi, J. Phys. Soc. Jpn. 76, 063705(2007).

[68] A. Barthelemy, A. Fert, and F. Petroff, Handbook of Magnetic Materials(Elsevier, Amsterdam, 1999).

[69] E.Y. Tsymbal and D.G. Pettifor, Solid State Phys. 56, 113 (2001).

[70] M.A.M. Gijs and G.E.W. Bauer, Adv. Phys. 46, 285 (1997).

[71] S.S.P. Parkin, N. More, and K. P. Roche, Phys. Rev. Lett. 64, 2304 (1990).

[72] J. Barnas, A. Fuss, R. E. Camley, P. Grunberg, and W. Zinn, Phys. Rev. B 42, 8110 (1990).

[73] Y. Seyama, A. Tanaka, and M. Oshiki, IEEE Trans. Magn. 35, 2838 (1999).

[74] H. Yuasa, M. Yoshikawa, Y. Kamiguchi, K. Koi, H. Iwasaki, M. Takagishi and M. Sahashi, J. Appl. Phys. 92, 2646 (2002).

[75] H. Yuasa, H. Fukuzawa, H. Iwasaki, M. Yoshikawa, M. Takagishi and M. Sahashi, J. Appl. Phys. 93 (2003), 7915.

[76]

[77] M. Takagishi, K. Koi, M. Yoshikawa, T. Funayama, H. Iwasaki, and M. Sahashi, IEEE Trans. Magn. 38, 2277 (2002).

[78] P. M. Levy, S. Zhang, T. Ono, and T. Shinjo, Phys. Rev. B 52, 16 049 (1995).

[79] S. F. Lee ,W. P. Pratt Jr., R. Loloee, P. A. Schroeder, and J. Bass, Phys. Rev. B 46, 548(1992).

[80] W. P. Pratt Jr., S. F. Lee, J. M. Slaughter, R. Loloee, P. A. Schroeder, and J. Bass,Phys. Rev. Lett. 66, 3060 (1991).

[81] Ed. By H. Ehrenreich And F. Spaepen, Sol. State Phys., vol. 56, pp.113-237, 2001.

[82] E. Yu. Tsymbal and D. G. Pettifor , J. Magn. Magn. Mater, vol. 202, Issue 1, Pages 163-173 , June 1999.

[83] Tehrani, S., B. Engel, J. M. Slaughter, E. Chen, M. De-Herrera, M. Durlam, P. Naji, R. Whig, J. Janesky, and J. Calder, IEEE Trans. Magn. 36, 27522757 (2000).

[84] S.Datta, Electronic Transport in Mesoscopic Systems, Cambridge University Press, Cambridge, UK, 1995.

[85] S. Nonoyama, A. Orugi, Phys. Rev. B 57, 8797 (1998).

[86] Y. Meyerand and N. S. Wingreen, Phys. Rev. Lett. 68, 2512 (1992).

[87] S. S. P. Parkin, Z. G. Li, and David J. Smith, Appl. Phys. Lett. 58, 2710 (1991).

[88] M. Takagishi, K. Koi, M. Yoshikawa, T. Funayama, H. Iwasaki, and M. Sahashi, IEEE Trans. Magn. 38, 2277, (2002).

[89] H. Fukuzawa, H. Yuasa, S. Hashimoto, K. Koi, H. Iwasaki, M. Takagishi, Y. Tanaka, M. Sahashi, IEEE Trans. Magn. 40, 2236 (2004).

[90] M. A. M. Gijs, S. K. J. Lenczowski, and J. B.Giesberg, Phys. Rev. Lett. 70, 3343 (1993).

[91] S. Agrawal, M. B. A. Jalil, S. G. Tan, K. L. Teo, and T. Liew, Phys. Rev. B 72, 075352(2005).

[92] S. G. Tan, Mansoor B. A. Jalil, J. Guo, Thomas Liew, K. L. Teo, T. C. Chong, J. Magn. Magn. Mater. 288, 418 (2005).

[93] Y. Yafet, J. Appl. Phys. 42, 1564 (1971).

[94] L. Berger, Phys. Rev. B 72, 100402R (2005).

[95] Y. Tserkovnyak, A. Brataas, G. E. W. Bauer, B. I. Halperin, Rev. Mod. Phys. 77, 1375 (2005).

[96] M. B. A. Jalil, S. G. Tan, S. Bala Kumar, Seongtae Bae, Phys. Rev. B 73, 134417 (2006).

[97] S. Bala Kumar, M. B. A. Jalil, S. G. Tan, and K. L. Teo, IEEE Trans. Magn. 42, 2459 (2006).

[98] K. Nagasaka, Y. Seyama, L. Verga, Y. Shimizu and A. Tanaka, J. Appl. Phys. 89 (2001), 6943.

[99] H. Fukuzawa, H. Yuasa, S. Hashimoto, H. Iwasaki, Y. Tanaka, Appl. Phys. Lett. 87, 082507 (2005).

[100] P. Holody, W.C. Chiang, R. Loloee, J. Bass, W.P. Pratt Jr., P.A. Schroeder, Phys. Rev. B 58, 12230 (1998).

[101] M. D. Stiles and D. R. Penn, Phys. Rev. B 61, 3200 (2000).

[102] E. I. Rashba, Eur. Phys. J. B 29, 513-527 (2002).).

[103] M. F. Gillies and A. E. T. Kuiper, J. Appl. Phys. 88, 5894 (2000).

[104] S. G. Tan, M. B. A. Jalil, Bala Kumar, K. L. Teo, and Thomas Liew, J. Appl Phys. 99, 084305 (2006).

[105] S. G. Tan, M. B. A. Jalil, S. Bala Kumar, K. L. Teo, Y. Zheng, and T. Liew, IEEE Trans. Magn. 42, 2673 (2006).

[106] W. G. Wang, C. Ni, T. Moriyama, J. Wan, E. Nowak, and J. Q. Xiao, Appl. Phys. Lett. 88, 202501 (2006).

[107] Y. V. Sharvin, Sov. Phys. JETP 21, 655 (1965).

[108] J. Peralta-Ramos and A. M. Llois, Phys. Rev. B 73, 214422 (2006).

[109] S. Yuasa, T. Nagahama, and Y. Suzuki, Science 297, 234 (2002).

[110] A. Vedyayev, N. Ryzhanova, C. Lacroix, L. Giacomoni, B. Dieny, Europhys. Lett. 39, 219 (1997).

[111] S. Zhang and P. M. Levy, Phys. Rev. Lett. 81, 5660 (1998).

[112] J. Mathon and A. Umerski, Phys. Rev. B 60, 1117 (1999).).

[113] J. J. Sun and P. P. Freitas, J. Appl. Phys. 85, 5264 (1999).

[114] P. LeClair, H. J. M. Swagten, J. T. Kohlhepp, R. J. M. van de Veedonk, W. J. M. de Jonge, Phys. Rev. Lett. 84, 2933 (2000).

[115] J. S. Moodera, T. H. Kim, C. Tanaka, C. H. de Groot, Philos. Mag. B 80, 195 (2000).

[116] P. LeClair, J. T. Kohlhepp, H. J. M. Swagten, W. J. M. de Jonge, Phys. Rev. Lett. 86, 1066 (2001).

[117] P. LeClair et al., Phys. Rev. B 64, 100406-1 (2001).

[118] T. Nozaki, Y. Jiang, Y. Kaneko, A. Hirohata, N. Tezuka, S. Sugimoto, and K. Inomata, Phys. Rev. B 70, 172401 (2004).

[119] J. S. Moodera, et al., Phys. Rev. Lett. 83, 3029 (1999).

[120] T. Nozaki, N. Tezuka, and K. Inomata, Phys. Rev. Lett. 96, 027208 (2006).

[121] T. Hanbicki, O. M. J. van t Erve, R. Magno, G. Kioseoglou, C. H. Li, G. Itskos, R. Mallory, M. Yasar, and A. Petrou, Appl. Phys. Lett. 82, 4092 (2003).

[122] H. Goronkin, S. Tehrani, T. Remmel, P. L. Fejes and K. J. Johnson, IEEE Trans. Electron Dev. 36, 281 (1989).

[123] S. Agrawal, M. B. A. Jalil, S. G. Tan, K. L. Teo, and T. Liew, Phys. Rev. B 72, 075352 (2005).

[124] R. Lipperheide and U. Wille, Phys. Rev. B 72, 165322 (2005).

[125] S. G. Tan, M. B. A. Jalil, S. Bala Kumar, K. L. Teo, Y. Zheng, and T. Liew, IEEE Trans. Magn. 42, 2673 (2006).

[126] S. G. Tan, M. B. A. Jalil, S. Bala Kumar, K. L. Teo, and Thomas Liew, J. Appl Phys. 99, 084305 (2006).

[127] H. D. Lu, L Shao, Y. L. Hou, T. P. Hou, Solid State Commun. 141, 61 (2007).

[128] Th. Schäpers, J. Nitta, H. B. Heersche, and H. Takayanagi, Phys. Rev. B 64, 125314 (2001).

[129] S. Sahoo, T. Kontos, J. Furer, C. Hoffmann, M. Grber, A. Cottet, and C. Schnenberger, Nat. Phys. 1, 99 (2005).

[130] S. Cho, Y.-F. Chen, and M. S. Fuhrer, Appl. Phys. Lett. 91, 123105 (2007).

[131] T. Yokoyama, Phys. Rev. B 77, 073413 (2008).

[132] Y. Imry and R. Landauer, Rev. Mod. Phys. 71, S306 (1999).

[133] M. P. Anantaram and T. R. Govindan, Phys. Rev. B 58, 4882 (1998).

[134] J. C. Cuevas, A. L. Yyati, and A. Marti-Redero, Phys. Rev. Lett. 80, 1066 (1998).

[135] M. Bransbyge, N. Kobayashi, and M. Tsukada, Phys. Rev. B 60, 17064 (1999).

[136] T. Yamada and Y. Yamamoto, Phys. Rev. B 55, 1902 (1996).

[137] M. Mogoga and C. Joachim, Phys. Rev. B 56, 4722 (1997).

[138] X. Xue, S. Datta, S. Hong, R. Reifenberger, J. I. Henderson, and C. P. Kubiak, Phys. Rev. B 59, R7852 (1999).

[139] C. Caroli, R. Combescot, P. Nozieres, and D. Saint-James, J. Phys. C 4, 916 (1971).

[140] R. Lake, G. Klimeck, R. C. Bowen, and D. Jovanovic, J. Appl. Phys. 81, 7845 (1997).

[141] J. Mathon, Phys. Rev. B 56, 11810 (1997).

[142] A. Cresti, R. Farchioni, G. Grosso, and G. P. Parravicini, Phys. Rev. B 68, 075306 (2003).

[143] T.N. Todorov, J. Phys.: Condens. Matter 14, 3049 (2002.

[144] H. Z. Xu and Y. Okada, Appl. Phys. Lett. 79, 3119 (2001).

[145] R. Zhu and Y. Guo J. Appl. Phys. 103, 073717 (2008).

[146] S. Bala Kumar, S. G. Tan, M. B. A. Jalil, P. Q. Cheung, and Yong Jiang, J. Appl. Phys. 103, 054310 (2008).

[147] T. P. Martin, A. Szorkovszky, A. P. Micolich, A. R. Hamilton, C. A. Marlow, H. Linke, R. P. Taylor, L. Samuelson, arXiv:0805.0504v1(2008).

[148] R. Jansen, B. C. Min, Phys. Rev. Lett. 99, 246604 (2007); B. T. Jonker, G. Kioseoglou, A. T. Hanbicki, C. H. Li and P. E. Thompson, Nat. Physics 3, 542 - 546 (2007) .

[149] S. G. Tan, M. B. A. Jalil, Thomas Liew, K. L. Teo, T. C. Chong, J. Appl. Phys. 97, 10D506 (2005).

[150] S. Bala Kumar, S. G. Tan, and M. B. A. Jalil, Appl. Phys. Lett. 90, 163101 (2007).

[151] G. C. Han, Y. K. Zheng, Z. Y. Liu, B. Liu, and S. N. Mao, J. Appl. Phys. 100, 063912 (2006).

[152] Y. Zheng, Y. Wu, K. Li, J. Qiu, G. Han, Z. Guo, P. Luo, L. An, Z. Liu, L. Wang, S. G. Tan, B. Zong, and B. Liu, J. Nanosci. Nanotechnol. 7, 117-137 (2007).

[153] J. S. Moodera, L. R. Kinder, T. M. Wong, and R. Meservey, Phys. Rev. Lett. 74, 3273 (1995).

[154] J. Schliemann, and D. Loss, Phys. Rev. B 68, 165311 (2003).

[155] A. Majumdar, Phys. Rev. B 54, 11911 (1996).).

[156] T. Valet and A. Fert, Phys. Rev. B 48, 7099 (1993).

[157] A. Fert and S.-F. Lee, Phys. Rev. B 53, 6554 (1996).

[158] W. H. Butler, X. G. Zhang, T. C. Schulthess, and J. M. MacLaren, Phys. Rev. B 63, 054416 (2001).

[159] S. Parkin, C. Kaiser. A. Parnchula, P. M. Rice, B. Hughes, M. Samant, and S.-H. Yang, Nat. Mater. 3, 862 (2004);S. Yuasa, T. Nagahama, A. Fukushima, Y. Suzuki and K. Ando, Nat. Mater. 3, 868 (2004).

[160] S. Bala Kumar, S. G. Tan, and M. B. A. Jalil, Appl. Phys. Lett. 90, 142106 (2007).

[161] T. Nozaki, A. Hirohata, N. Tezuka, S. Sugimoto, and K. Inomata, Appl. Phys. Lett. 86, 082501 (2005).

[162] S. Bala Kumar, S. G. Tan, M. B. A. Jalil and J. Guo, Appl. Phys. Lett. 91, 142110 (2007).

[163] P K Chakraborty and K P Ghatak, J. Phys. D: Appl. Phys. 32, 2438 (1999).

[164] K. Wakabayashi, M. Sigrist, Phys. Rev. Lett. 84, 3390 (2000).

[165] K. Wakabayashi, Phys. Rev. B 64, 125428 (2001).

[166] K. Tada, K. Watanabe, Phys. Rev. Lett. 88, 127601 (2002).

[167] C.P. Chang, C.L. Lu, F.L. Shyu, R.B. Chen, Y.C. Huang, M.F. Lin, Physica E 82, 27 (2005).

[168] Y. Shibayama, H. Sato, T. Enoki, M. Endo, Phys. Rev. Lett. 84, 1744 (2000).

[169] S.C. Chen, T.S. Wang, C.H. Lee and M.F. Lin, Phys. Lett. A 372, 5999 (2008).

[170] J.Y. Wu, J.H. Ho, Y.H. Lai, T.S. Li and M.F. Lin, Phys. Lett. A 369, 333 (2007).

[171] K. Harigaya, Chem. Phys. Lett. 340, 123 (2001).

[172] K. Wakabayashi, M. Fujita, H. Ajiki, and M. Sigrist, Phys. Rev. B 59, 8271 (1999).

[173] Y.C. Huang, C.P. Chang, M.F. Lin, Nanotechnology 18, 495401 (2007).

Name: Bala kumar a/l Sundaram Pillay

Degree: The Degree of Doctorate Engineering

Department: Electrical and Computer Engineering

University: National university of Singapore

Thesis Title: Spin Transport study in Spintronic Nanodevices

Abstract

A detail understanding of the physics of spin transport phenomena is essential to enhance the performance of present spintronic devices, as well as in designing new devices for future applications. This thesis consists of theoretical study and simulation on the physics of spin transport in spintronic nanodevices. The aim of our simulation is to harness the physics of spin transport to improve the performance of devices such as the spin-valves and spin-transistors, as well as to propose new design for these devices. In this thesis, first the effects of various device parameters on spin transport is analyzed in detail. Focus is given to the understanding of the fundamental physics of spin transport as well as identifying any anomalous and novel effects. Once transport physics and the various transport effects are well understood, then we utilize this understanding to enhance the performance of the devices. We also explore new methods and device designs in order to further improve the performance.

Keywords:

Spintronics, Spin valve, Gaint Magnetoresistance, spin injection, spin drift diffusion, Green's Function

SPIN TRANSPORT STUDY IN SPINTRONICS NANODEVICES

BALA KUMAR A/L SUNDARAM PILLAY

NATIONAL UNIVERSITY OF SINGAPORE

2008

SPIN TRANSPORT STUDY IN SPINTRONIC NANODEVICES BALA KUMAR A/L SUNDARAM PILLAY 2008